DISSERTATION

EXPLORING NANOAGGREGATE STRUCTURES OF MODEL ASPHALTENES USING TWO DIMENSIONAL INFRARED SPECTROSCOPY

Submitted by

Jenée D. Cyran

Department of Chemistry

In partial fulfillment of the requirements

For the Degree of Doctor of Philosophy

Colorado State University

Fort Collins, Colorado

Summer 2015

Doctoral Committee:

Advisor: Amber T. Krummel

Elliot Bernstein
Nancy Levinger
Thomas Borch
Sonja Kreidenweis

ABSTRACT

EXPLORING NANOAGGREGATE STRUCTURES OF MODEL ASPHALTENES USING TWO DIMENSIONAL INFRARED SPECTROSCOPY

Asphaltenes have been an enigma in the scientific community; studies on the molecular masses have differed by orders of magnitude and structures have been debated between island or archipelago structures. Thus, the asphaltene community defines asphaltenes by their solubility. Asphaltenes are *n*-heptane-insoluble and toluene-soluble. The known nanoaggregation of asphaltenes at different timescales and concentrations causes issues to determine the molecular weight and structure of asphaltene molecules. This thesis is the first step to using two-dimensional infrared (2D IR) spectroscopy to study the nanoaggregate structure of model asphaltenes. 2D IR spectroscopy is a vibrational spectroscopy that is advantageous over linear IR absorption due to the ability to spread the spectral information over two axes. The 2D IR spectra give rise to structurally sensitive cross-peaks, affording the ability to probe the structure of the nanoaggregates. The model asphaltenes used in this work are violanthrone-79 and lumogen orange, a perylene derivative. These model asphaltenes consist mostly of polycyclic aromatic hydrocarbons (PAHs), similar to asphaltenes. Violanthrone-79 and lumogen orange also have carbonyl functional groups, which provide vibrational probes. The carbonyl stretching and ring breathing vibrations are used to probe the stacked structure of the nanoaggregates. A quinone series of one, two and three ring systems was used to first study the coupling between the carbonyl stretching and ring breathing vibrational modes. The quinone series provided the foundation for the larger ring systems that emulate asphaltenes. The data from studying the

stacked structure of nanoaggregate model asphaltenes can be used to reveal properties of nanoaggregate asphaltenes. This work will allow for continued study of the kinetics of nanoaggregation using 2D IR waiting time experiments for dynamic information. Thus, this work demonstrates the use of 2D IR spectroscopy, which offers femtosecond time resolution, as a viable technique for studying nanoaggregation.

ACKNOWLEDGEMENTS

Graduate school is quite the roller coaster. The frequency of the oscillations vary, and there seems to be more hardships and struggles than success. However, one long data collection night makes it all worth the while. This experience would not have been possible without the unwavering support of many wonderful people.

I would like to thank Amber for being a great mentor and for inspiring me to be a better scientist. While Amber always gave me a hard time about rotations and how long it took me to decide which group to join, I can say with 100% confidence that I made the right decision, and I could not have completed graduate school without her. Amber's excitement for science is contagious, and she is a strong motivator. Thank you for always believing in me and for building my confidence.

A special thanks to the Krummel group, both past and present, for all of you have taught me many new things and have made this experience fun. Thank you for helping me grow and helping me learn to be a mentor. I have enjoyed our group bonding experiences, and I am happy to have been introduced to bananagrams. Good luck on all of your future endeavors, and I hope our paths meet again.

Thank you to all of the friends I have met outside of the group and graduate school. You all have kept me sane, and I enjoyed all of the great conversations, the good times and this wonderful community. Thank you to all of the Department of Chemistry support staff at Colorado State University. You have all made this experience easier and less stressful.

I would like to thank my family for their love and support. My parents have been my biggest fans and have always encouraged me to follow my dreams no matter how far away my dreams

take me. My sisters are wonderful and have kept me "cool" while I was in graduate school. Thank you for always reminding me about the big picture and remembering to enjoy life. Thank you to my wonderful puppy, Tucker. I hope you don't mind moving to Germany.

TABLE OF CONTENTS

LIST OF TABLES

LIST OF FIGURES

Chapter 1

Introduction

1.1. Asphaltenes

Asphaltenes are a component in heavy crude oils, bitumen and coal. The core of asphaltenes consists of polycyclic aromatic hydrocarbons (PAHs). Asphaltenes are named based on having asphalt-like properties and can be used for paving roads or shingles for roofs. Asphaltenes are known to aggregate and form nanoaggregates and clusters rendering asphaltenes the cholesterol of the oil industry. The nanoaggregates and clusters grow and eventually cause refinery pipes to corrode, foul, and even clog. Due to the aggregation, the molecular structure of asphaltenes is difficult to determine. Therefore, asphaltenes are most commonly defined by their solubility properties; asphaltenes are toluene-soluble and *n*-heptane-insoluble.[1]

Asphaltenes have been studied for many decades due to their important role in the oil industry and oil recovery. Experiments have been conducted to determine the molecular weight and structure of asphaltenes using mass spectrometry,[2,3] scanning and transmission electron microscopy (SEM and TEM),[4] time-resolved fluorescence depolarization (TRFD),[5] and other techniques. However, the molecular weight and structure of asphaltenes are highly debated due to the inherent nanoaggregation tendencies and their biodiversity varying from location to location. Researchers agree that asphaltenes consist of PAH cores with aliphatic side chains and can contain heteroatoms, such as sulfur, oxygen and nitrogen. Model compounds composed of PAH cores with aliphatic side chains are often used to study different properties of asphaltenes. There are discrepancies on the structures, mostly between island or archipelago configurations.[6] However, both configurations contain similar PAH cores and side chains. The structures of the

model asphaltenes, a perylene derivative and violanthrone-79, used in this thesis work are illustrated in Figure 1.1.

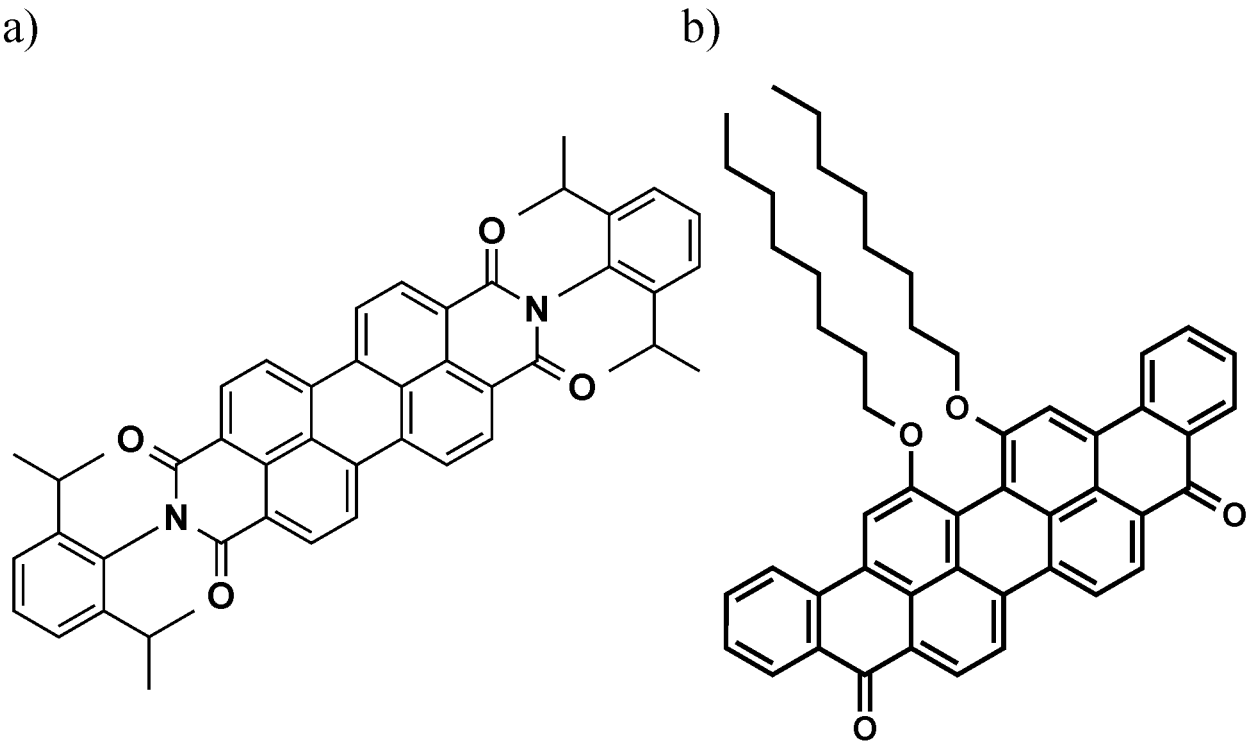

Figure 1.1. Structures of model asphaltenes, (a) a perylene derivative and (b) violanthrone-79, used in experiments.

Studies have also been completed to determine properties of the nanoaggregate structure of asphaltenes and model asphaltenes. The critical nanoaggregate concentration (CNAC) has been found on asphaltene and model asphaltenes to be 0.1 g/L.[1,7] Molecular dynamic (MD) simulations were completed and found the number of molecules per aggregate and begin to probe the structure of different aggregates.[8,9] These studies are beginning to probe the nanoaggregate structures. However, the aggregates probed with NMR and fluorescence studies have only looked at dimers. The MD simulations report that the nanoaggregates contain 6-7

molecules per aggregate. Therefore, studies must be completed using techniques that can probe larger nanoaggregate structures.

Model asphaltenes are often used to probe the fundamental interaction of asphaltenes and nanoaggregate structures. Perylene derivatives and violanthrone-79 are appropriate model asphaltenes since they are both composed of PAHs, have side chains, and are consistent with idealized molecular structures for asphaltenes.[1] The goal of this work was to probe the nanoaggregate structure of asphaltenes and understand how the asphaltenes molecules are stacked.

Nanoaggregation of asphaltenes and model asphaltenes is driven by the π-stacking interactions between the core rings of the PAHs. Molecular dynamic (MD) simulations[9,10] and NMR experiments[11] have been used to study the nanoaggregation of violanthrone-78. The results of the MD simulations indicate that there are about 7 violanthrone molecules per aggregate and the molecules are stacked 4.5 Å apart. Experimentally, the nanoaggregates have been difficult to study. Monomers and dimers were studied with fluorescence spectroscopy. However, larger nanoaggregates tend to have overwhelming fluorescence signal rendering fluorescence spectroscopy impractical. Vibrational spectroscopy, specifically 2D IR spectroscopy, provides the structural sensitivity needed to study the nanoaggregate structure of model asphaltenes. Larger nanoaggregate structures can be probed using 2D IR spectroscopy. 2D IR spectroscopy also offers femtosecond time resolution, which can be used to study the kinetics of the nanoaggregation.

1.2. 2D IR Spectroscopy

2D IR spectroscopy is a rapidly growing technique used to study the vibrational modes of molecules to obtain structural and dynamic information. 2D IR spectroscopy has been used to study the molecular structure of DNA[12,13] and peptides,[14,15] as well as the dynamics of hydrogen bonding[16] and chemical exchange kinetics.[17] Linear IR absorption and 2D IR spectroscopy probe molecular vibrations using mid-infrared light. Linear IR absorption is used to determine the functional groups and connectivity of atoms in the condensed phase. The vibrational modes are resonant with specific frequencies in the mid-IR region.[18] The molecular vibrations are sensitive to the solvent environment and structure of the molecules. Nonlinear IR spectroscopy, such as 2D IR, provides more observables for understanding complex chemical systems. 2D IR offers structural resolution and time resolution on the femtosecond (fs) time scale.[19]

2D IR spectroscopy was developed based on the methodology of two-dimensional nuclear magnetic resonance (2D NMR). NMR is an absorption method when nuclei are exposed to a magnetic field. 2D NMR spectra spread the spectral information over two axes and can be used to determine molecular structures. The appearance of cross peaks in a 2D NMR spectrum indicate coupling between spins, which can reveal information about connectivity and separation of nuclei.[20] Thus, 2D NMR reveals structural information for molecules in the solution phase. 2D NMR can also be used to look at dynamics of a system. However, NMR experiments sample at the millisecond time scale, which is slower than many chemical reactions. 2D IR spectroscopy samples at the fs time scale and can be used to track faster chemical reactions. 2D IR spectroscopy has the same structural sensitivity as 2D NMR and two axes of spectra compared to one for linear IR absorption spectroscopy. Therefore, 2D IR spectroscopy is a technique capable of studying nanoaggregation of model asphaltenes.

2D IR spectra have diagonal peak pairs, one is negative and one is positive, that result from a bleach of an excited state and a stimulated emission, as illustrated in Figure 1.2. The negative peaks are a result of a 0-1 transition and the positive peaks are a result of a 1-2 transition. There can be off-diagonal peak pairs that arise due to vibrational coupling between two vibrational modes. The off-diagonal peaks in Figure 1.2 are due to vibrational coupling between the antisymmetric and symmetric carbonyl stretching vibrational modes in lumogen orange. Vibrational coupling is seen between vibrational modes that are close in space and energy. Thus, vibrational coupling can report the structure of the molecules. The separation between the negative and positive peak pairs is the vibrational anharmonicity.

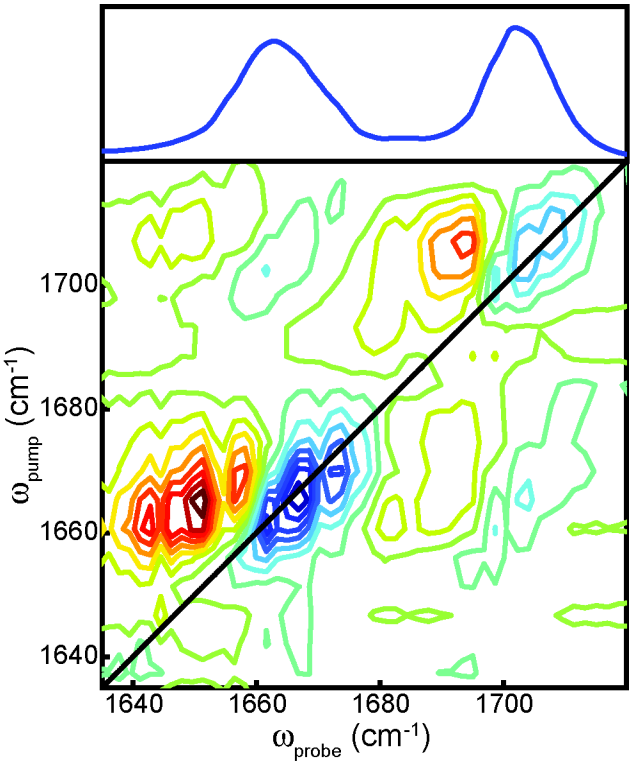

Figure 1.2. Linear IR absorption and 2D IR spectra of a 10 mM perylene derivative in chloroform. The negative peaks (blue) are from the 0-1 transition and the red peaks result from the 1-2 transition.

The ring breathing and carbonyl stretching vibrational modes are used as the probes to understand model asphaltene nanoaggregate structure. Smaller ring systems, such as quinones and anthrone, were used to understand the monomeric ring and carbonyl vibrational coupling. The normal vibrational modes are measured using linear IR absorption and 2D IR spectroscopy. The normal modes are the linear combination of the local modes of the molecule. The local modes are important for relating the molecular vibrations to the structure of the molecule. The local mode picture of the model asphaltenes was used to probe the nanoaggregate structure in solution.

1.3. Outline of Thesis

This thesis details our efforts in elucidating the nanoaggregate structure of model asphaltenes, violanthrone-79 and perylene derivative using vibrational spectroscopy, including 2D IR spectroscopy.

In Chapter 2, the details of the 2D IR spectrometer setup are laid out. Chapter 2 also describes how to calculate 2D IR spectra and how to complete electronic structure calculations. The appendices I and II are examples of MATLAB and Gaussian code to complete the calculations.

Chapter 3 discusses our development of active Bragg correction to waveforms for mid-IR pulse shaping. Active Bragg corrections result in shaped pulses with a full width half max (FWHM) of 150 fs, similar to the probe pulses.

Characterizing anharmonic vibrational modes of a quinone series is the subject of Chapter 4. One, two, and three ring quinones were studied to understand the ring breathing and carbonyl stretching vibrational coupling. By inverting the 1Q-Hamiltonian, we are able to quantify the

vibrational coupling between the ring breathing and carbonyl stretching modes. The results from the quinone investigation set the foundation for ring-carbonyl interactions for larger PAHs and model asphaltenes.

Chapter 5 explores the nanoaggregate structure of a model asphaltene, violanthrone-79, in chloroform using 2D IR spectroscopy. We looked at three different nanoaggregate structures based on molecular dynamic simulations; parallel, anti-parallel, and a chiral 28 degrees. We also calculated 2D IR spectra of mixtures of different configurations. Based on the 2D IR spectra, the aggregates are best represented by mixtures of the configurations with majority contributions from the anti-parallel configuration.

The nanoaggregate structure of perylene derivative, a model asphaltene, is studied in Chapter 6. Waiting time experiments were completed to look at the ultrafast dynamics of the perylene system. Understanding the structure of asphaltene nanoaggregates opens the door to exploring the kinetics and dynamics for nanoaggregate formation.

References

(1) Mullins, O. C. The Asphaltenes. *Annu. Rev. Anal. Chem.* **2011**, *4* (1), 393–418.

(2) Hortal, A. R.; Hurtado, P.; Martínez-Haya, B.; Mullins, O. C. Molecular-Weight Distributions of Coal and Petroleum Asphaltenes from Laser Desorption/Ionization Experiments. *Energy Fuels* **2007**, *21* (5), 2863–2868.

(3) Becker, C.; Qian, K.; Russell, D. H. Molecular Weight Distributions of Asphaltenes and Deasphaltened Oils Studied by Laser Desorption Ionization and Ion Mobility Mass Spectrometry. *Anal. Chem.* **2008**, *80* (22), 8592–8597.

(4) Trejo, F.; Ancheyta, J.; Rana, M. S. Structural Characterization of Asphaltenes Obtained from Hydroprocessed Crude Oils by SEM and TEM. *Energy Fuels* **2009**, *23* (1), 429–439.

(5) ANDREWS, A. B.; SHIH, W.-C.; MULLINS, O. C.; NORINAGA, K. Molecular Size Determination of Coal-Derived Asphaltene by Fluorescence Correlation Spectroscopy. *Appl. Spectrosc.* **2011**, *65* (12), 1348–1356.

(6) Sabbah, H.; Morrow, A. L.; Pomerantz, A. E.; Zare, R. N. Evidence for Island Structures as the Dominant Architecture of Asphaltenes. *Energy Fuels* **2011**, *25* (4), 1597–1604.

(7) Rane, J. P.; Harbottle, D.; Pauchard, V.; Couzis, A.; Banerjee, S. Adsorption Kinetics of Asphaltenes at the Oil–Water Interface and Nanoaggregation in the Bulk. *Langmuir* **2012**, *28* (26), 9986–9995.

(8) Kuznicki, T.; Masliyah, J. H.; Bhattacharjee, S. Aggregation and Partitioning of Model Asphaltenes at Toluene−Water Interfaces: Molecular Dynamics Simulations. *Energy Fuels* **2009**, *23* (10), 5027–5035.

(9) Jian, C.; Tang, T.; Bhattacharjee, S. Molecular Dynamics Investigation on the Aggregation of Violanthrone78-Based Model Asphaltenes in Toluene. *Energy Fuels* **2014**, *28* (6), 3604–3613.

(10) Jian, C.; Tang, T. One-Dimensional Self-Assembly of Polyaromatic Compounds Revealed by Molecular Dynamics Simulations. *J. Phys. Chem. B* **2014**, *118* (44), 12772–12780.

(11) Shi, M.-M.; Chen, Y.; Nan, Y.-X.; Ling, J.; Zuo, L.-J.; Qiu, W.-M.; Wang, M.; Chen, H.-Z. Π−π Interaction among Violanthrone Molecules: Observation, Enhancement, and Resulting Charge Transport Properties. *J. Phys. Chem. B* **2011**, *115* (4), 618–623.

(12) Krummel, A. T.; Mukherjee, P.; Zanni, M. T. Inter and Intrastrand Vibrational Coupling in DNA Studied with Heterodyned 2D-IR Spectroscopy. *J. Phys. Chem. B* **2003**, *107* (35), 9165–9169.

(13) Peng, C. S.; Jones, K. C.; Tokmakoff, A. Anharmonic Vibrational Modes of Nucleic Acid Bases Revealed by 2D IR Spectroscopy. *J. Am. Chem. Soc.* **2011**, *133* (39), 15650–15660.

(14) Hamm, P.; Lim, M.; DeGrado, W. F.; Hochstrasser, R. M. The Two-Dimensional IR Nonlinear Spectroscopy of a Cyclic Penta-Peptide in Relation to Its Three-Dimensional Structure. *Proc. Natl. Acad. Sci.* **1999**, *96* (5), 2036–2041.

(15) Woutersen, S.; Hamm, P. Structure Determination of Trialanine in Water Using Polarization Sensitive Two-Dimensional Vibrational Spectroscopy. *J. Phys. Chem. B* **2000**, *104* (47), 11316–11320.

(16) Elsaesser, T.; Huse, N.; Dreyer, J.; Dwyer, J. R.; Heyne, K.; Nibbering, E. T. J. Ultrafast Vibrational Dynamics and Anharmonic Couplings of Hydrogen-Bonded Dimers in Solution. *Chem. Phys.* **2007**, *341* (1–3), 175–188.

(17) Kwak, K.; Zheng, J.; Cang, H.; Fayer, M. D. Ultrafast Two-Dimensional Infrared Vibrational Echo Chemical Exchange Experiments and Theory†. *J. Phys. Chem. B* **2006**, *110* (40), 19998–20013.

(18) Wilson, E. B.; Decius, J. C.; Cross, P. C. *Molecular Vibrations: The Theory of Infrared and Raman Vibration Spectra*; Dover: Mineola (N.Y.), 1980.

(19) Zanni, M. T.; Gnanakaran, S.; Stenger, J.; Hochstrasser, R. M. Heterodyned Two-Dimensional Infrared Spectroscopy of Solvent-Dependent Conformations of Acetylproline-NH2†. *J. Phys. Chem. B* **2001**, *105* (28), 6520–6535.

(20) Aue, W. P.; Bartholdi, E.; Ernst, R. R. Two-dimensional Spectroscopy. Application to Nuclear Magnetic Resonance. *J. Chem. Phys.* **1976**, *64* (5), 2229–2246.

Chapter 2

Methods and Materials

2.1. Introduction

The objective for this work is to use 2D IR spectroscopy to probe the nanoaggregate structure of model asphaltene compounds. 2D IR spectroscopy is a third order nonlinear infrared spectroscopy. There are three pulse interactions with the sample, and a third order signal is emitted from the sample. 2D IR experiments can be completed in the time domain or the frequency domain. The 2D IR spectrometers can be setup by four-wave mixing, in a box-CARS geometry, or utilizing mid-IR pulse shaping using a germanium based acousto-optic modulator (Ge-AOM).[1] The work completed in this thesis is based on 2D IR experiments utilizing pulse shaping techniques. Pulse shaping affords 2D IR experiments with high phase stability, apposed to four-wave mixing, which often requires active phasing for the data.[2,3] We are set up in a pump-probe geometry, therefore, the third order signal follows the probe beam path to the detector. The absorptive spectra, a combination of rephasing and nonrephasing, are collected with the spectrometer.[4]

2.2. Overview of Experimental Setup

Figure 2.1 illustrates the overview of the experimental setup used for the 2D IR experiments utilizing pulse shaping technologies. A Wyvern-1000 Ti:sapphire regenerative amplifier system (KM Labs) is used to generate 800 nm pulses for pumping an optical parametric amplifier (OPA). The amplifier is seeded by a Kerr-lens modelocked Ti:sapphire oscillator. The oscillator is pumped with the 3 W output from a Nd:YVO_4 Spectra Physics Millennia continuous wave

laser with p-polarization. The output pulse train has a repetition rate of 75 MHz (200 mW mode-locked power, 50-70 nm bandwidth at FWHM). There is a photodiode in the oscillator that provides the trigger for the timing for the rest of the system. The photodiode was modified from the original setup to avoid additional back scatter from the regenerative amplifier.

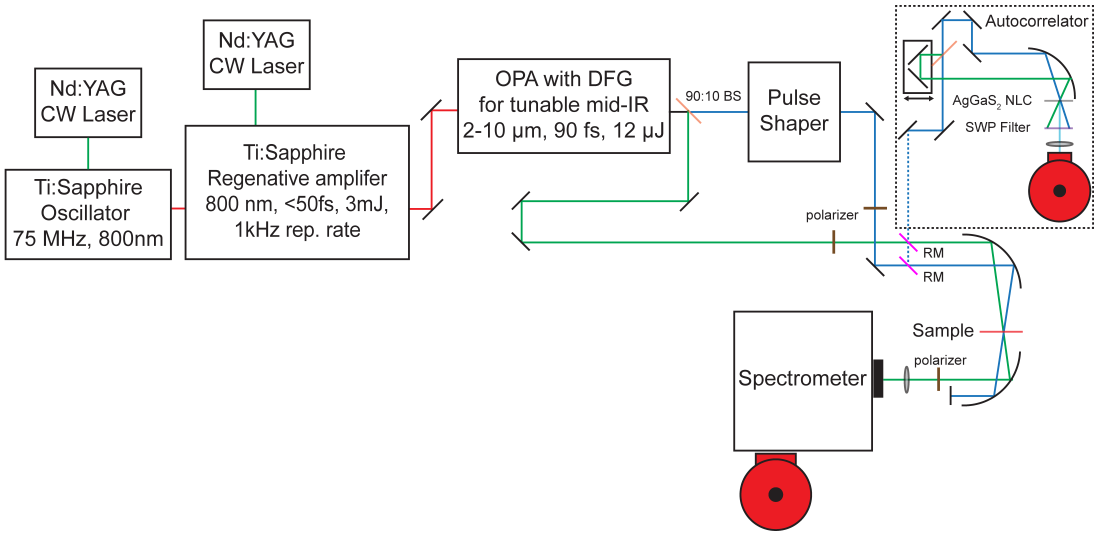

Figure 2.1 2D IR Experimental Setup is illustrated. The pulse shaper is shown in more detail in Figure 2.2.

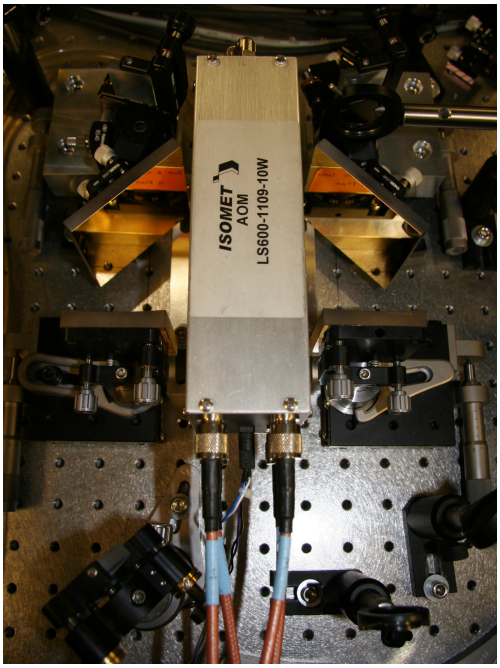

Figure 2.2 Pulse shaper setup with Ge-AOM. The pulse shaper setup is in a 4-f geometry consisting of a grating to spatially resolve the frequencies, a cylindrical mirror to focus the light on the AOM and a folding mirror to direct the light to the AOM. Identical optics are used on the second half after the AOM.

The oscillator pulse train is sent to a stretcher to stretch out the pulses in time. The amplifier is a chirped pulse amplifier; thus the pulses need to be chirped before entering the amplification stage. Temporally chirped pulses have the lower frequencies of light arriving first and the higher frequencies of light arriving last. The stretched pulse enters a multi-pass Ti:sapphire amplifier that is cryogenically cooled. The amplifier is pumped by a Lee Laser (LDP Series, 1 kHz, 13 W, 532 nm). Solid-state diodes at 1064 nm are used as the pump source from the Nd:YAG laser rod. There are two Q-switches that are used to pulse the laser. A second harmonic generation (SHG) assembly follows the Q-switches to produce 532 nm light. The Lee Laser runs at a 1 kHz repetition rate. The 532 nm light travels to the amplification cavity and is used to amplify the seed pulses. The seed pulses travel to the Pockels cell and a $\lambda/4$ waveplate. When the Pockels cell is on, it acts as a $\lambda/4$ waveplate, which negates the $\lambda/4$ waveplate. The pulse will be trapped in the cavity when the Pockels cell is on. The beam travels through one pass in the cavity in about 14 ns. The Pockels cells are turned on for about 200 ns corresponding to 12 passes through the cavity. The Pockels cells timing is set to pick the largest intensity pulse; this is monitored with a fast photodiode and the oscilloscope.

A grating compressor is used to compress the pulses in time. Two gratings are used in the compressor, and the beam reflects off each grating twice. The position of the gratings is adjusted to eliminate or reduce higher order dispersion. The output pulses are centered at 800 nm, 45 fs in duration, and the average power is 3 W. The pulse duration is measured with a frequency resolved optical gating (FROG) using SHG on a beta barium borate (BBO) crystal. The spectrum of the pulse can also be measured with scatter on a photodiode.

The laser output is used to pump an OPA (TOPAS-C, Light Conversion) with a difference frequency stage attached to generate 90 fs 6 μm pulses. The light enters the OPA box and hits a

beam-splitter to separate the light for the two amplification stages. The first amplification stage begins with a beam splitter where a small portion of the light is used to generate white light with a sapphire plate. The remaining light is used as the pump for the first stage of amplification. The white light continuum and the pump are combined into a nonlinear crystal, beta-Barium borate (type II). The amplified white light is called the signal. The signal and the pump separated from the first beam-splitter are overlapped in space and in time in a second nonlinear crystal, type II BBO. The signal and pump are collinear in the crystal as well as at longer distances. The amplified signal and idler continue to the difference frequency stage (DFG) while the pump is dumped to the side of the OPA. The DFG stage consists of a silver gallium sulfide ($AgGaS_2$) crystal. The angles of the crystals are changed to tune the output wavelength of light. For the experiments in this thesis, the light was tuned to 5 and 6 μm. The pulse durations are measured with an intensity autocorrelation..

The intensity autocorrelation is a SHG technique. The light is separated with a d-mirror into two arms and the arms meet horizontally parallel at a 6 in parabolic mirror. The two arms are overlapped in time and space in a $AgGaS_2$ crystal. The SHG signal is produced between the two arms, and the two beams are filtered out with a short wave pass filter. The SHG signal is detected on a mercury cadmium telluride (MCT) detector. A stage is set in one of the arms and is scanned while the other arm is stationary. Intensity is recorded for each of the steps of the stage and an intensity plot versus the time is plotted. The resulting autocorrelation of the OPA output pulses are 90 fs.

The output of the OPA is overlapped with a helium neon (HeNe) laser in order to track the mid-infrared light. 2D IR spectrometers are not commercially available and thus need to be

home built. The oscillator, regenerative amplifier, and OPA were all commercially available. The rest of the spectrometer was home built.

In order to do 2D IR experiments, three mid-IR pulse interactions are needed to produce a fourth electric field that is the third order nonlinear response. The OPA output hits a 90:10 (T:R) beam-splitter and is separated into two pathways: a probe pathway and a pump pathway. The probe pathway is unmodified and is directed along the pathway to the detector. The probe pathway also contains a computer delay stage used for setting T_0 and for waiting time experiments. The pump pathway is directed to a pulse shaper setup, where the pulse is modified to act as two pulses. The HeNe IR overlap needs to be completed before and after the beam splitter. The beam splitter slightly changes the pointing of the HeNe, which causes misalignment between the IR and HeNe after transmission through the beam splitter.

2.2.1. Mid-Infrared Pulse Shaper Setup

The mid-IR pulse shaper setup was developed by the Zanni group,[5,6] and our setup is shown in Figure 2.2. The light is directed onto a grating that disperses the light in frequency space. The light goes to a cylindrical mirror and then a folding mirror to a germanium acousto-optic modulator (AOM, Isomet Corporation LS600-1109). After the AOM, identical optics as the first side are setup to complete a 4-*f* shaper setup. An arbitrary waveform generator (AWG, DynamicSignals LLC PXDAC4800) is used to send waveforms to the AOM. The carrier frequency of the waveform is 75 MHz. A piezoelectric transducer converts the waveform into an acoustic wave that travels through the Ge crystal. Changing the amplitude and phase of the waveform shapes the pulse.

The setup and calibration are described elsewhere and briefly here.[7] The first optic in the shaper setup is a grating with a groove density of 100 ln/mm located on a translation stage. The light is spatially separated, and the HeNe is used to estimate the center wavelength. For instance, we are set to 6000 nm light which corresponds to the nine and a half HeNe reflection. This HeNe reflection is centered at a cylindrical mirror (129.4 mm f.l.). The beams reflect off a 3-inch gold folding mirror and travel into the Ge-AOM at the Bragg angle. To set the first half of the optics, the AOM is removed and replaced with a 3-inch gold folding mirror centered where the AOM would be centered. The 3-inch gold folding mirror, sending light to the AOM, is set so the light is flat and straight. The optic is changed to the Bragg angle at the end. Also, the 90:10 beam splitter is replaced with a 50:50 beam splitter. The light is reflected back through the first half by the 3 inch gold folding mirror and reflects off of the 50:50 beam splitter. The light is sent to the autocorrelator, which can also be used as a single arm SHG setup. The stage position of the first grating is translated to optimize the SHG signal. The second side of the shaper has identical optics. The pyro electric detector and the oscilloscope are used to detect the light from the second grating. The second grating is rotated until the light is seen on the oscilloscope. The pulse duration is determined by the autocorrelator before the Ge-AOM is put into place. This ensures that the shaper setup is not altering the pulse widths. A pulse scan is also completed to ensure that there is no clipping on the shaper optics.

The next step is to slide the Ge-AOM into position between the two sets of optics. With the AOM off, a pulse scan is collected to verify no frequencies are clipping on the Ge-AOM. The RF amplifier and the chiller are turned on for the Ge-AOM. The chiller temperature is set to 22.0 °C. The next step to change the folding mirrors so the light directed to the Ge-AOM is at the Bragg angle. The folding mirrors are turned only in the horizontal direction away from the

user. The mirrors are adjusted until the Bragg angle is achieved. Turning the Ge-AOM on and off tests the Bragg angle. There should be little to no light reaching the array detector when the Ge-AOM is one and the pulse shaper setup is at the Bragg angle.

2.2.2. Ge-AOM Calibration

The Ge-AOM is calibrated to map the frequencies of the pulse and the time dependence of the mask on the Ge-AOM. Two waveforms are needed to calibrate the Ge-AOM; the first is a frequency comb and the second is a single peak. Both waveforms are set in Array Magic program under the AWG tab. The number of samples is 15 and the number of peaks can vary but are usually set to 41 peaks. This calibration can be completed with or without the active-Bragg compensation.[8] For waiting time experiments, the active-Bragg compensation should not be used. The pump beam is directed to the MCT array detector to complete the calibration. The single peak and the frequency comb are inputs into the AutoCombFit MATLAB file and are illustrated in Figure 2.3a. The AOM sample slope and the AOM center peak sample are also inputs and can be found in Array Magic program after the number of peaks are picked for the frequency comb. An example of the time-frequency calibration plot is illustrated in Figure 2.3b. The AWG frequency obtained from the oscillator is also an input. The polynomial fit will produce three parameters, p_0, p_1 and p_2. These polynomial fit parameters are inputs into the AOM calibration file, AOM_Freq_Calibration.ini. Once the inputs are put into the AOM calibration file, Array Magic needs to be restarted. The new calibration parameters should be listed in the AWG settings tab.

Dispersion from traveling through the AOM must also be accounted for with the pulse shaper setup. Group velocity dispersion (GVD) and third order dispersion (TOD) are adjusted in the

waveform. To measure the dispersion compensation, the SHG setup in the autocorrelator is used. The Dispersion Parameter Scan (DPS) tab in Array Magic is used to run the dispersion scans. An example of a DPS output is shown in Figure 2.3c, where GVD and TOD are plotted. The highest intensity point is used for the GVD and TOD inputs in AWG settings tab. The GVD and TOD results will change depending on whether or not the Bragg correction is used. The calibration and dispersion compensation are completed to obtain two pump pulses similar to the probe pulse. The autocorrelation of a single pump pulse with Bragg correction is normally around 120 fs.

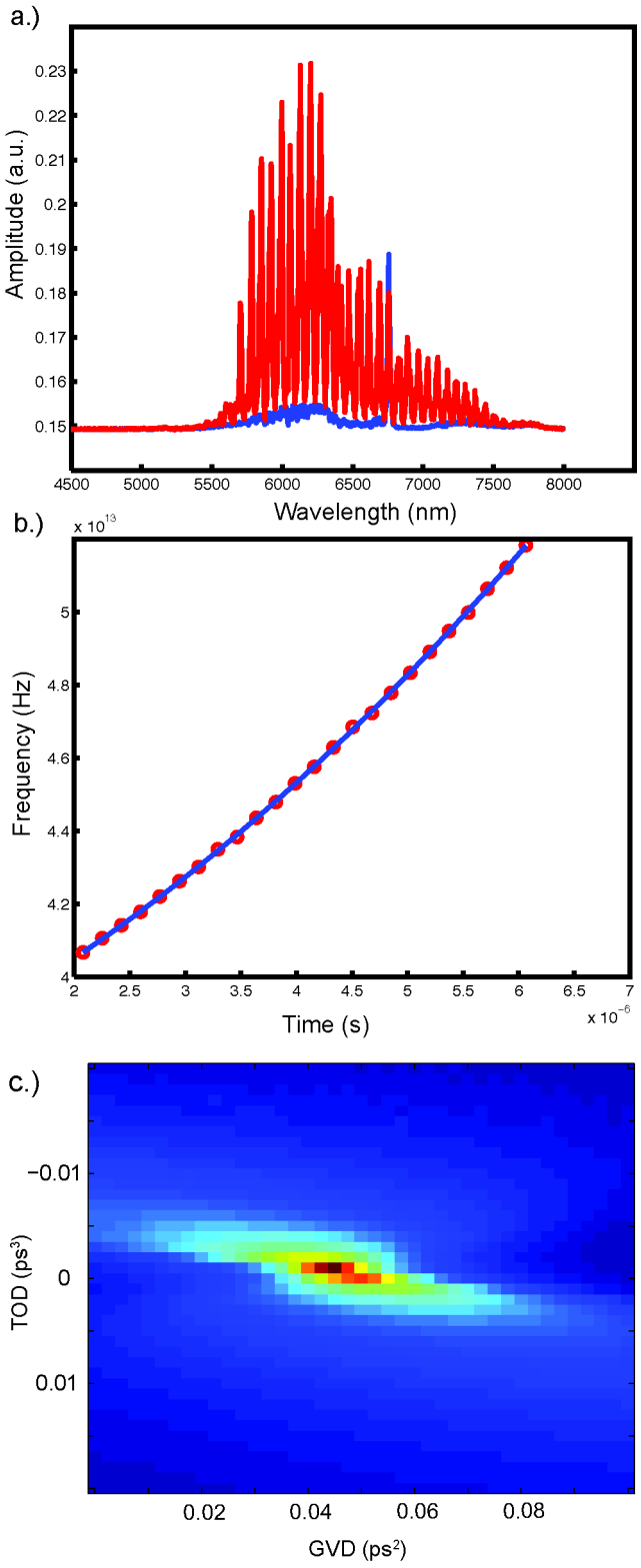

Figure 2.3. Outputs from AutoCombFit MATLAB file where a) are the frequency comb and single peak pulse scans and b) is the polynomial fit to determine the relationship between time and frequency for the AOM. c) The dispersion parameter scan output plotted in MATLAB.

2.2.3. 2D IR Spectrometer

The pump pulses (the light from the pulse shaper side) and the probe pulse are in pump-probe geometry. Both the pump and probe pulses travel through a telescope to increase the beam diameter and to gain a tighter focus at the sample. The pump and the probe pulses reflect off of a 6 inch f.l. parabolic and are separated by 1 inch. The two beams are focused in the sample and are overlapped spatially and temporally. A second parabolic mirror is used to collimate the beams after the sample. The probe is focused onto the slit of the spectrometer (0.25 mm) with a lens and detected on a 64 element MCT array detector (Infrared Systems and Infrared Associates). The femtosecond pulse acquisition system (FPAS) is used as an integrator and analog-to-digital converter (ATD). The pump beam also has a pathway to the spectrometer for diagnostic and calibration purposes. The Array Magic program is used to view the light on the array detector, to do pump-probe scans and 2D IR scans.

The pump and probe are temporally and spatially overlapped using a pinhole. Each arm is sent through the pinhole and detected on the array detector. The pointing is optimized and then T_0 is set by doing a pump-probe scan to look for the interference between the probe and the pump scatter in the pinhole. A 2 mm Germanium window was used next to set T_0. However, molecular samples have been found to be a better resource to set T_0. Molecular samples of either acetic acid or dimethylformamide (DMF) in carbon tetrachloride are used to set a more accurate T_0. The 2D IR scans are from 0 to 2500 fs with a 7 fs step size and are averaged over 300 scans per sample. Phase cycling is used to remove transient absorption and scatter from the spectra. Phase cycling is a procedure where the relative phase of the two pump pulses is changed. There are 4 frames for phase cycling, (0,0), (0,π), (π,π), and (π,0).[1] By changing the relative phase of the pump pulses, unwanted signals from transient absorption and scatter can be removed. If

rephasing and nonrephasing spectra need to be separated, there is an 8-frame scheme that should be used and the spectra can be separate post processing. The system is purged for collection of all pulse scans, calibration scans, and for sample collection. An air dryer (Pure Gas, PHF Series) is used to remove water lines and CO_2 absorption from the spectra.

2.2.4. Triggering and Timing

The trigger pulses and timing for all components is crucial for 2D IR experiments. Triggering and timing schematics for 2D IR experiments utilizing pulse shapers can be found elsewhere and are described briefly here.[7] The 75 MHz oscillator is the input into a divider circuit to generate the 1 kHz pulse train. The 1 kHz signal is the input trigger for the digital delay generator (DDG, Stanford Research Systems). The DDG is used to produce four 1 kHz signals with independent delays. A delay of 50 μs is used to trigger the regenerative amplifier's pump laser and the Pockels cells. A delay of 53 μs is used to trigger the FPAS for data acquisition. A delay of 38 μs is used to trigger an AWG, which generates the RF masks sent to the AOM. An RF amplifier amplifies the RF masks before the masks are sent to the AOM. The AOM delay is set to 8 μs. The 75 MHz signal from the oscillator is also multiplied to be the trigger for the clock of the AWG. The AWG has an external trigger that is the oscillator multiplied by 15. This exact frequency should be inputted into the AWG program (PXDAC4800 Playback) for best results. The AWG also requires a pulse widener to go from 10s of microseconds to 100s of microseconds. This is a little white circuit board that is connected to the computer and the AWG. The circuit board must be on in order to chop the signal.

2.3 Sample Preparation

All of molecules used for experiments in this thesis were commercially available. 1,4-Benzoquinone and violanthrone-79 were purchased from Sigma Aldrich. 1,4-Napthoquinone and 9,10-anthraquinone were purchased from Acros Organics. The peryelene derivative, *N,N'*-Bis(2,6-diisopropylphenyl)-3,4,9,10-perylenetetracarboxylic diimide, was purchased from TCI America. Different solvents were tried to obtain aggregation while also aiming to have no solvent peaks in the region of interest. Originally toluene and n-heptane were going to be used to study the nanoaggregation of the model asphaltenes. The concentration for aggregation for toluene and n-heptane are low, under 0.1 mM. Chloroform was used for this work because the infrared absorption peak is around 1550 cm^{-1}, which lies outside of the region of interest. Therefore, there are no solvent peaks interfering with the peaks from the molecules of interest. Chloroform was also used since the aggregation occurs above 1 mM. The optical density (OD) of the IR peaks for 1 mM or higher concentrations for these molecular systems are easily detected with our 2D IR spectrometer.

Each sample was prepared fresh daily to ensure aggregation was kept constant. Further aggregation is noticeable when the samples have been sitting for a day. The perylene and violanthrone-79 samples were sonicated for 5 minutes. Samples were placed between two calcium fluoride windows with a Teflon spacer for UV-vis, linear IR absorption and 2D IR spectroscopies.

2.4. Linear IR Absorption Spectroscopy

Linear IR absorption spectra are collected on a Nicolet 6700 spectrometer with the Omnic software. The FTIR attachment is used as well as screen C. The screen prevents the liquid

nitrogen cooled MCT detector from being over saturated. Each spectrum has 4 cm^{-1} resolution and averaged 64 scans. The system was purged with nitrogen to remove water absorption. The spectra were processed using the atmospheric suppression correction available in the Omnic software and saved as .CSV files. The spectra were imported into MATLAB and a percentage of chloroform background was subtracted. The spectra were also baseline corrected in MATLAB by picking two end points and adjusting the end points to zero for the spectra. The spectra were also fit with Gaussian line shapes to obtain the peak position, FWHM, and peak height or intensity.

2.5. Ultraviolet-visible Spectroscopy

Ultraviolet-visible (UV-vis) spectroscopy was used to study the nanoaggregation of the model asphaltenes. A concentration series, ranging from 0.01 mM to 20 mM for violanthrone and 0.5 mM to 10 mM for lumogen orange, was completed to determine the concentration where nanoaggregates form. Nonlinearities in concentration gradients correspond to aggregation processes. For example, the UV-vis spectra for violanthrone-79 had a blue shift when the concentration was increased. The blue shift is indicative of H-aggregation, where the dipoles are aligned and the molecules are stacked vertically in the z-axis. Thus, UV-vis spectroscopy probes the structure of the nanoaggregate. The UV-vis spectroscopy experiments were completed on a Nicolet Evolution 300 spectrophotometer (Thermo Electron Corporation) owned by the Reynolds group. Normally cuvettes are used for UV-vis experiments, however, the concentrations needed to aggregate violanthrone-79 and lumogen orange were too high to use cuvettes, which typically have large path lengths. The path lengths for 0.1 mM to 20 mM of violanthrone-79 in chloroform ranged from 25 μm to 100 μm spacers. The spectrophotometer

has a removable cuvette holder. The cuvette holder is replaced with a homemade sample holder and sample cell, which is also used for the linear IR absorption spectrometer. CaF_2 plates and chloroform have UV-vis absorption around 200 nm and are not interfering with the molecular samples of interest. The UV-vis spectra can be baseline corrected and have the chloroform background subtracted using MATLAB code similar to the linear IR absorption spectra.

2.6. Gaussian Calculations

Electronic structure calculations were completed to obtain the dipole derivatives needed for simulated linear IR absorption and 2D IR spectra. An example of the geometry and frequency optimization calculations can be found in Appendix II. The method for the calculations was density functional theory (DFT) with the Becke-3-Lee-Yang-Parr (B3LYP) exchange-correlation functional. The basis set was 6-31G(d) for the calculations. Other basis sets, such as 6-311G(d,p), and other methods, including Moller Plesset (MP), were used for geometry optimization and frequency calculations. However, there was no basis set or method dependence for the calculations on the quinone series. Calculations were also completed taking into account the solvent. These calculations for the quinone series included the dielectric constant for the solvent, chloroform. The anharmonic keyword was used to calculate the anharmonic vibrational modes. An example of the input for a Gaussian calculation on to the Rappé group's cluster is found in Appendix II section A2.1. The code in Appendix II section A2.2 illustrates how to obtain the dipole vectors for individual normal modes. The dipole vectors for the individual normal modes are used as the input dipole vectors for simulating linear IR absorption and 2D IR spectra. Corrections were applied to the energies based on the basis set and method used.[9] The dipole derivative vectors were only used for anthrone and violanthrone-79. There were

discrepancies between the energies and intensities in the quinone series between experimental and theoretical results. Thus, the linear IR absorption and 2D IR spectra could not be simulated for the quinone series.

2.7. Simulating 2D IR Spectra

The code for simulating 2D IR spectra can be found in Appendix I. The code utilizes outputs from Gaussian geometry optimization and anharmonic frequency calculations (Gaussian 09 Rev D01).[10] The transition dipoles from the calculations are used to determine the stacked configuration of violanthrone-79 as detailed in chapter 5. The file name for the code is trimer_par.m and is used to calculate the one- and two-quantum Hamiltonians and to calculate the response functions. Thus, the end result is to produce linear and 2D IR simulated spectra.

The coupling matrices are built by using transition dipole coupling (TDC) model.[11] TDC is a simple method used to describe only electrostatic coupling between transition dipoles. The equation for coupling, β, described by TDC depends on angle and distance between the two transition dipoles. The TDC model breaks down when the transition dipoles are too close together and systems that contain mechanical coupling as well.

The coupling terms calculated from TDC are inputs into the one-quantum Hamiltonian. The MATLAB code for calculating the vibrational coupling terms using TDC can be found in Appendix I section 2.2. The one-quantum Hamiltonian, including the β terms, is diagonalized to produce the eigenvalues for local mode energies and eigenvectors that are the transition dipole vectors. The linear IR absorption spectra are simulated and the line shape uses a pure dephasing time of 1 ps.

The two-quantum Hamiltonian is built by using the overtone and combination bands of the states in the one-quantum Hamiltonian. The anharmonicity for the states is also needed and can be extracted for the experimental 2D IR spectra. Calculating the rephasing and nonrephasing response functions simulates the 2D IR spectra. The polarization in these calculations is set to all horizontal. The polarization can be altered in the response functions.[12]

2.8 Deciphering 2D IR Spectra

2D IR spectra have peaks that come in peak pairs. One peak will be negative and one peak will be positive in the peak pairs. Cartooned examples of 2D IR spectra are illustrated in Figure 2.4. There are peak pairs along the diagonal and there can also be off-diagonal or cross peak pairs as well. The peak pairs are separated by anharmonicity.

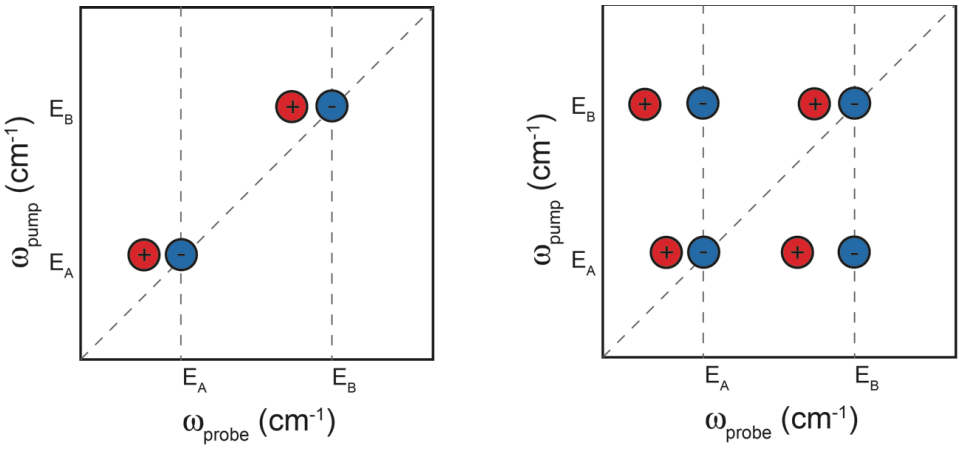

Figure 2.4 Cartooned 2D IR spectra illustrated diagonal and off-diagonal peak pairs.

References

(1) Hamm, P.; Zanni, M. T. *Concepts and Methods of 2D Infrared Spectroscopy*; Cambridge, 2011.

(2) Volkov, V.; Schanz, R.; Hamm, P. Active Phase Stabilization in Fourier-Transform Two-Dimensional Infrared Spectroscopy. *Opt. Lett.* **2005**, *30* (15), 2010–2012.

(3) Backus, E. H. G.; Garrett-Roe, S.; Hamm, P. Phasing Problem of Heterodyne-Detected Two-Dimensional Infrared Spectroscopy. *Opt. Lett.* **2008**, *33* (22), 2665–2667.

(4) Khalil, M.; Demirdöven, N.; Tokmakoff, A. Obtaining Absorptive Line Shapes in Two-Dimensional Infrared Vibrational Correlation Spectra. *Phys. Rev. Lett.* **2003**, *90* (4), 047401.

(5) Shim, S.-H.; Strasfeld, D. B.; Fulmer, E. C.; Zanni, M. T. Femtosecond Pulse Shaping Directly in the Mid-IR Using Acousto-Optic Modulation. *Opt. Lett.* **2006**, *31* (6), 838–840.

(6) Shim, S.-H.; Strasfeld, D. B.; Zanni, M. T. Generation and Characterization of Phase and Amplitude Shaped Femtosecond Mid-IR Pulses. *Opt. Express* **2006**, *14* (26), 13120–13130.

(7) Middleton, C. T.; Woys, A. M.; Mukherjee, S. S.; Zanni, M. T. Residue-Specific Structural Kinetics of Proteins through the Union of Isotope Labeling, Mid-IR Pulse Shaping, and Coherent 2D IR Spectroscopy. *Methods* **2010**, *52* (1), 12–22.

(8) Nite, J. M.; Cyran, J. D.; Krummel, A. T. Active Bragg Angle Compensation for Shaping Ultrafast Mid-Infrared Pulses. *Opt. Express* **2012**, *20* (21), 23912.

(9) Andersson, M. P.; Uvdal, P. New Scale Factors for Harmonic Vibrational Frequencies Using the B3LYP Density Functional Method with the Triple-Z Basis Set 6-311+G(d,p). *J. Phys. Chem. A* **2005**, *109* (12), 2937–2941.

(10) Frisch, M. J.; Trucks, G. W.; Schlegel, H. B.; Scuseria, G. E.; Robb, M. A.; Cheeseman, J. R.; Scalmani, G.; Barone, V.; Mennucci, B.; Petersson, G. A.; et al. *Gaussian 09 Revision D.01*.

(11) Krimm, S.; Bandekar, J. Vibrational Spectroscopy and Conformation of Peptides, Polypeptides, and Proteins. In *Advances in Protein Chemistry*; C.B. Anfinsen, J. T. E. and F. M. R., Ed.; Academic Press, 1986; Vol. 38, pp 181–364.

(12) Hochstrasser, R. M. Two-Dimensional IR-Spectroscopy: Polarization Anisotropy Effects. *Chem. Phys.* **2001**, *266* (2–3), 273–284.

Chapter 3

Active Bragg Angle Compensation for Shaping Ultrafast mid-Infrared Pulses

This chapter is a publication from 2012 and is published in Optics Express.[1] I contributed to this work by helping to build the 2D IR spectrometer, data collection for the autocorrelations and 2D IR spectra, and for the sample preparation. We found that using a waveform that corrected for the Bragg angle produced shorter pulses and the correction would be applicable to shape ultrafast pulses of light with broad bandwidths. It should be noted that the affects this new waveform on waiting time experiments has not been fully determined. While collected data for waiting time experiments, the Bragg correction is not used.

3.1. Introduction

Multidimensional optical spectroscopies have proven to be measurements of high utility for investigations regarding a variety of physical and chemical phenomena. For example two- and three-dimensional electronic spectroscopies have been employed to measure charge transfer processes and structural rearrangements in proteins related to these processes.[2–4] Two- and three-dimensional infrared spectroscopy has gained broader use in examining structural rearrangements and solvent dynamics involved in charge transfer,[5,6] charge transfer in organic photovoltaic materials,[7] nucleic acids,[8,9] and protein folding events.[10–12] In fact, the multitude of chemical systems investigated using multidimensional nonlinear spectroscopies only continues to grow at a rapid pace. Recent advances in pulse shaping have opened up new possibilities for multidimensional electronic and multidimensional infrared spectroscopies due to the simplicity

of beam geometries made available, higher signal-to-noise ratios obtained, and higher spectral acquisition rates.[10,13–15] In addition, advancements in the use of broadband light sources have also been made. For example, non-linear optical spectroscopy experiments are now being performed with continuum mid-IR ultrafast light sources.[16–19] Direct pulse shaping in the mid-IR and continuum mid-IR ultrafast light sources are two technologies with promise of pushing the field of multidimensional IR spectroscopy forward. However, these two technologies are not necessarily compatible with each other due to the geometrical constraints associated with pulse shaping.

In modulating an optical pulse by pulse shaping, the temporal profile of a pulse is determined by the bandwidth of the pulse and the relative phases between each wavelength. By manipulating each frequency independently, it is possible to produce arbitrarily modified pulses. This process is represented as $E'(\omega)= M(\omega)E(\omega)$, where $E(\omega)$ is the original optical field represented in the frequency domain, $M(\omega)$ is the mask that represents the modification to the pulse, and $E'(\omega)$ is the resulting optical field. For example, a mask that produces a double pulse is given by

$$M(\omega) = \frac{1}{2}(e^{-i\varphi_1} + e^{-i(\tau\omega+\varphi_2)}) \qquad \text{Equation 3.1}$$

where τ is the separation between the pulses, and φ_1 and φ_2 are the absolute phases of each pulse in the pulse pair. This waveform is utilized in 2D IR spectroscopy and 2D electronic spectroscopy experiments.[20–22]

Pulse shapers developed recently for directly shaping mid-IR light are based on acousto-optic modulators that operate in the Bragg regime. As such, it is the geometry of the acousto-optic interaction that controls the efficiency of the modulation of the optical wave and the efficiency of the diffraction of the light. Achieving operation in the Bragg regime requires the interaction

length between light and sound to be long. In this case, phase-matching conditions are important. Momentum conservation between the light and sound waves requires that the incident and diffracted optical waves both be at the Bragg angle relative to the acoustic wave for efficient diffraction.[23–25] If this condition is not satisfied, a wavevector mismatch results which gives rise to angular dispersion. As pulse shapers are employed with longer wavelength light or larger optical bandwidth systems, angular dispersion increases due to the larger differences in Bragg angle from one side of the spectrum of the pulse to the other.

For the majority of AOM-based pulse shapers, a sine wave is used to drive the AOM device. The shaping mask is integrated into the sine wave by separating the waveform into amplitude and phase portions, and implementing the masks as amplitude and phase modifications to the sine wave as follows:

$$Waveform(t) = M_{amp} \sin(f_c t + M_{\varphi}) \qquad \text{Equation 3.2}$$

where f_c is the center frequency of the AOM and $M_{amp}(t)$ and $M_{\varphi}(t)$ are the time dependent amplitude and phase portions of the shaping mask.

The pulse shapers utilized for shaping mid-IR light are comprised of a Germanium acousto-optic modulator (Ge-AOM) fixed in the Fourier plane of a zero-dispersion compressor (ZDC) line. The frequency components in the mid-IR pulse are spatially resolved in the first half of the zero-dispersion compressor and directed onto the Ge-AOM, often by a gold folding mirror. In the case of a constant frequency and amplitude acoustic wave being driven across the crystal, only one specific frequency component impinges on the AOM at the proper Bragg angle. The Bragg angle is given by,

$$\sin\theta_B = \frac{\lambda f}{2vn(\lambda)} \qquad \text{Equation 3.3}$$

where λ is the optical wavelength, f is the center acoustic frequency, ν is the acoustic velocity in the medium, and $n(\lambda)$ is the wavelength dependent index of refraction of light. This equation gives a single Bragg angle for a specific wavelength and acoustic frequency. Thus, only one optical frequency component will diffract off the acoustic wave front at the Bragg angle, while all of the other components will deviate from the Bragg angle resulting in angular dispersion of the light. Figure 3.1a depicts this result. Each frequency component is incident on the AOM at a constant angle, θ_B, which is the Bragg angle for the center frequency component. The other frequency components will diffract at angles governed by the phase-matching direction given by the addition of the optical wavevector and the acoustic wavevector. In order to mitigate angular dispersion introduced by the AOM, the acoustic wave must have the proper frequency at specific positions in the AOM crystal such the Bragg condition is satisfied for all frequency components contained in the mid-IR pulse. Figure 3.1b depicts the case of the acoustic wave front arriving at the appropriate part of the crystal in order for all optical frequencies to be incident and diffract at the Bragg angle, θ_B.

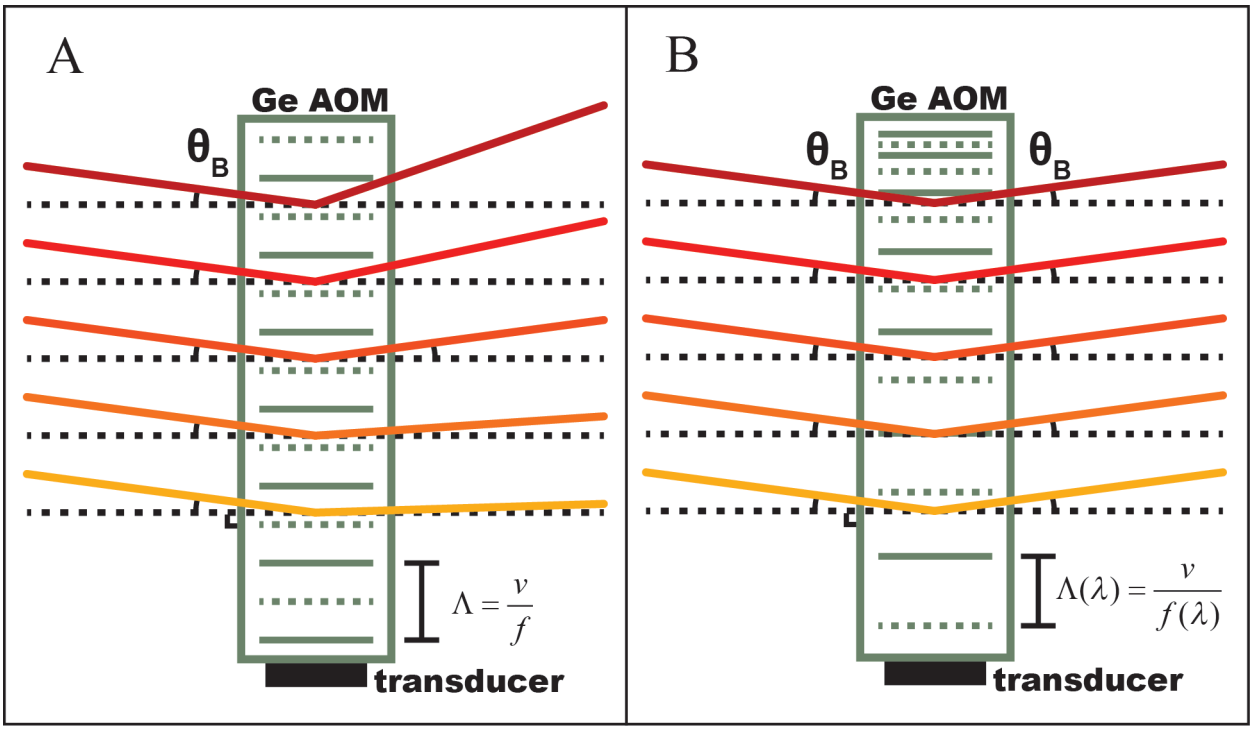

Figure 3.1. Illustrations of Bragg deflections in an AOM crystal for spatially separated frequencies of light using a constant frequency acoustic wave (a) and a Bragg angle compensated acoustic wave (b). The solid and dashed lines in the AOM crystal represent the acoustic wave. The different frequencies of light, each represented by different colors, all enter the device at the same angle, θ_B.

In order to realize the situation depicted in Figure 3.1b, we have developed a waveform to actively satisfy the Bragg condition. This is accomplished by utilizing the arbitrary waveform generator (AWG) to take advantage of the full acoustic bandwidth available and generating an acoustic wave with a frequency that is dependent upon the optical wavelength of the pulse. The AOM has an acoustic velocity that is constant and because a pair of folding mirrors are used to direct all optical frequencies to and from the AOM, a constant, C, can be defined,

$$C = 2v\sin\theta_B = \frac{\lambda_0 f_c}{n(\lambda_0)} \qquad \text{Equation 3.4}$$

where λ_o is the center wavelength of the pulse and f_c is the center frequency of the acoustic wave. Using the Bragg angle equation, a new acoustic frequency is calculated that depends on the wavelength of light being diffracted,

$$\frac{\lambda f(\lambda)}{n(\lambda)} = C = \frac{\lambda_0 f_c}{n(\lambda_0)} \qquad \text{Equation 3.5}$$

$$f(\lambda) = \frac{\lambda_0 f_c n(\lambda)}{\lambda n(\lambda_0)} \qquad \text{Equation 3.6}$$

Substituting this expression into the equation for a pulse modulating waveform gives,

$$Waveform(t) = M_{amp}(t)\sin(2\pi f(\lambda)t + M_{\varphi}(t)) \qquad \text{Equation 3.7}$$

where the shaping mask is described by its time dependent amplitude $M_{amp}(t)$, and time dependent phase, $M_{\varphi}(t)$. Although the wavelength dependent acoustic frequency is included, this equation is not correct since it is only true for constant frequencies. Instead, the instantaneous phase must be considered, using the equation,

$$Waveform(t) = M_{amp}(t)\sin(\phi(t) + M_{\varphi}(t)) \qquad \text{Equation 3.8}$$

where $\phi(t)$ is the instantaneous phase expressed as

$$\phi(t) = \phi_0 + 2\pi \int_0^t f(\tau)\, d\tau \qquad \text{Equation 3.9}$$

where ϕ_o is the initial phase. Equation 3.9 requires the function for frequency to be in terms of time with respect to the acoustic wave while equation 3.6 gives the frequency in terms of wavelength. Using the same calibration procedures required to map the IR frequency onto the spatial dimension of the mask, as well as the time-dependence of the RF mask produced by the AWG, the Bragg angle correction frequency can be obtained in terms of the acoustic waveform time scale. This gives a new waveform equation,

$$Waveform(t) = M_{amp}(t)\sin(\phi_0 + 2\pi\int_0^t f_\lambda(\tau)\,d\tau + M_\varphi(t))$$

Equation 3.10

where $f_\lambda(\tau)$ is the Bragg angle compensated acoustic frequency converted to the time scale of the acoustic wave. Below we describe the experimental implementation of this waveform, provide the temporal pulse characteristics produced utilizing this waveform, and demonstrate its utility in 2D IR spectroscopy.

3.2. Experimental Methods

The design and layout of our two-dimensional infrared spectrometer utilizes a partially collinear beam geometry, such as those implemented in pump-probe experiments; an acousto-optic modular is placed in the pump beam-line similar to work demonstrated by Zanni and co-workers. Briefly, our spectrometer consists of an ultrafast pulsed, light source, a pulse shaper, and multi-element detection system. In our system, a Ti:sapphire oscillator (KM Laboratories) produces an 80 MHz pulse train of sub-50 fs, 2.5 nJ pulses centered at 800 nm. The pulses from the oscillator are used to seed a regenerative chirped pulse amplifier (KM Laboratories Wyvern 1000) producing pulses at a 1 kHz repetition rate that are 3 mJ in energy, centered at 800 nm, and are sub-50 fs in duration. These pulses pump an optical parametric amplifier (OPA, Light Conversion TOPAS-C) fit with a difference frequency generation stage, to produce tunable mid-IR light. In this work, the mid-IR pulses are centered at 4830 nm, are 15 μJ in energy, and 100 fs in duration. A long-wave pass filter is used to separate the mid-IR light from any remaining signal and idler light.

The mid-IR pulses are directed into the spectrometer box, and overlapped with a HeNe laser to facilitate alignment. The mid-IR is split into two beam paths using a wedged ZnSe 90:10 (T:R) beam splitter. The majority of the light is directed towards the pulse shaper and the remainder of

the light is directed along a second path and serves as the probe beam in our experiments. A Ge-AOM based pulse shaper is used to generate pulse pairs for 2D IR spectroscopy and is described below. A pump-probe beam geometry is used for 2D IR experiments; the pump and probe beams are reflected off of a gold coated 90° off-axis parabolic mirror (152.4 mm f.l.). After the sample, the pump and probe beams are collected on an identical parabolic reflector, and are directed towards a spectrometer composed of a Triax 190 spectrometer (Horiba) coupled with a 2x32 element HgCdT array detector (Infrared Systems Development and Infrared Associates). The probe beam is directed into the spectrometer and focused onto the entrance slits of the spectrometer using a 100 mm focal length lens. We determine the resolution of the spectrometer by scanning the spectrum of a pulse across one element in the center of the MCT array and compare the width of the water vapor absorption lines to the linear IR spectrum of water vapor in the 5-6 μm region. Based on these data, the resolution of our spectrometer is approximately 4 cm^{-1} with the chosen grating.

The mid-IR pulse shaper is composed of a Ge-AOM (Isomet Corporation LS600-1109) placed in the Fourier plane of a zero-dispersion compressor line. The geometry utilized is a reflective implementation introduced by Shim et al. for pulse shaping directly in the mid-IR.[26,27] In our system, the input mid-IR beam is passed over a cylindrical mirror and dispersed by a grating with a blaze wavelength of 5.2 μm and a groove density of 100 ln/mm. The grating is adjusted to a quasi-Littrow configuration, where the diffracted IR light is reflected back on itself, but is tilted downward, and the diffracted beam is collected by a cylindrical mirror (129.4 mm f.l.). The spatially separated and collimated frequency components of the mid-IR beams are reflected off a 3-inch gold folding mirror into the Ge-AOM at the Bragg angle. The second half of the shaper is set up to mirror the first half with identical optics.

As a result of the Ge-AOM being a traveling wave device, the timing between the acoustic waveform and the mid-IR pulse must be synchronized. The oscillator contains a fast photodiode for detecting the 80 MHz output pulse train. In order to accommodate the timing of the Ge-AOM, the 80 MHz pulse train is diverted into a phase lock loop circuit (Maxim MAX3639). This circuit produces two output signals: a 300 MHz signal used to sync the clock of the AWG to the oscillator and another 80 MHz signal to be reduced to 1 kHz for the regenerative amplifier. In addition, the 1 kHz signal used to trigger the regenerative amplifier components is sent through a digital delay generator (DDG, Berkley Nucleonics Corp. Model 575). The DDG uses the 1 kHz signal to produce 4 additional 1 kHz signals with independent time delays. The first channel produces a pulse that is delayed by 50 μs that is used to trigger the regenerative amplifier's pump laser and Pockels cell. The second channel is used to trigger data acquisition with a delay of 53 μs. Channels three and four are used to trigger the RF amplifier for the Ge-AOM and the AWG (GaGe CompuGen 4302) with delays of 8 μs and 38 μs, respectively. This ensures that the acoustic waveform has reached the proper location in the Ge-AOM crystal when the light arrives at the crystal to produce the desired modified pulse. Following the procedure outlined by Middleton et al., a frequency comb is used to correlate the time for the acoustic wave to travel to a spot in the crystal and affect a specific frequency of light.[28]

In order to characterize the pulse durations of the shaped pulses, a home-built, noncolinear, intensity autocorrelator is used. In the autocorrelator, the pulse to be measured is split into two equal beams using a D-shaped gold mirror; thus producing the fixed and delay arms typically present in autocorrelators. The beams from each arm are horizontally overlapped with the delay arm at a 90° gold off-axis parabolic mirror (101.6 mm f.l.). Both beams are reflected and focused into a Type I $AgGaS_2$ crystal for frequency doubling. The SFG signal arising from the

interaction of the two pulses is passed through a short-wave pass filter to block out any fundamental light that did not undergo SFG and is focused into a single element HgCdT detector (Infrared Associates). This signal is integrated using a boxcar integrator and collected using a digital-to-analog converter (Infrared Systems Development).

3.3. Results and Discussion

Implementing pulse shaping experimentally requires two optical components. First, an apparatus is needed to spatially separate each frequency of the pulse. A zero-dispersion compressor consisting of gratings and lenses to separate and collimate each frequency of light is utilized for this purpose. The Ge-AOM is introduced into the ZDC line and fixed at the Fourier plane. The duration of the pulse is measured. In Figure 3.2a, several intensity autocorrelations of the pulse are compared. First, the temporal duration of the pulse prior to entering the pulse shaper is 98 fs as noted in Figure 3.2a. There is little change in the pulse duration after the ZDC line is constructed; the output pulse corresponds to what would be the zero-order diffraction of light with the Ge-AOM in place. With the Ge-AOM in place, the zero-order diffraction of the light is characterized after the shaper and is stretched in time to 650 fs due to the mid-IR pulse traveling through the 20 mm thick crystal. This result is consistent with the work of Zanni and co-workers.[26,28] Upon driving the constant frequency and amplitude acoustic wave through the Ge-AOM and directing the first-order diffraction output to the array detector, a frequency-time calibration is performed for the pulse shaper. In addition, a slit and the array detector are used to determine the presence of spatial dispersion and a spectrum of the pulse is inspected to ensure that none of the frequency components are clipped in the pulse shaper. If either of these problems exists, they are corrected prior to continuing with optimizing the pulse shaper. The

pulse duration measured after the calibration is 3766 fs—this is almost 6 times larger than the pulse duration of the zero-order diffraction prior to activating the Ge-AOM. The autocorrelation trace is shown in Figure 3.2a.

There are steps to be taken to optimize the pulse shaper, each of which aim to compensate for group velocity dispersion (GVD) and third-order dispersion (TOD) in the pulse as determined previously.[26] The second harmonic signal generated in a $AgGaS_2$ crystal from the output pulses of the shaper is used for this optimization. Additional phase terms can be added to pulse shaping waveforms to compensate for GVD and TOD by expanding the phase as a function of frequency in a Taylor's series expansion. Utilizing the AWG, a series of waveforms can be generated in order to scan the GVD and TOD terms; the SHG signal maxima is indicative of the appropriate GVD and TOD values to be used. The GVD and TOD terms determined for the constant amplitude waveform are 0.088 ps^2 and -0.005 ps^3 for GVD and TOD, respectively. Subsequently, the focal length from the second cylindrical mirror to the second grating is slightly adjusted using a translation stage under the second grating in order to further improve the SHG signal of the output of the shaper. The measured duration of this pulse is 255 fs and is shown in Figure 3.2b. It is important to note that even though the FWHM of the pulse is significantly improved, long tails on the either side of the pulse still exist. The alignment of the shaper optics was performed several times producing the same result each time.

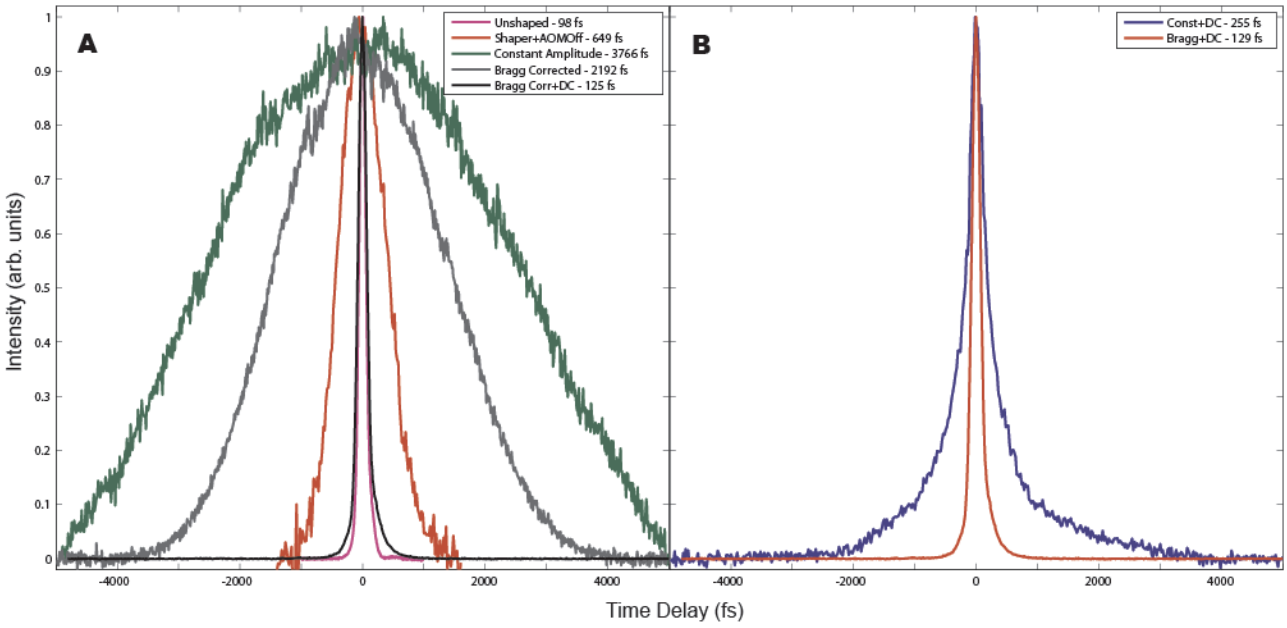

Figure 3.2. Intensity autocorrelations of mid-IR pulses. (a) Comparisons of the measured autocorrelations for mid-IR pulses traveling through the shaper device in a variety of configurations compared to mid-IR pulses not passing through the shaper. Only a combination of a Bragg angle corrected waveform and GVD/TOD corrections produce pulses with comparable pulse durations to the unmodified pulses. (b) Comparisons between shaped pulses generated with and without the Bragg angle compensation. Both configurations were measured using GVD and TOD corrections optimized for the waveform type used. All autocorrelations are normalized.

The optical bandwidth of our mid-IR pulses produced from the OPA is exceptional. The FWHM bandwidth of the pulse is routinely measured to be 900-1100 nm centered at either 5 μm or 6 μm, depending on the chemical system under investigation. This constitutes a change in the Bragg angle, $\Delta\theta_B$, equal to 0.44 degrees. For comparison, a visible pulse centered at 800 nm with a FWHM bandwidth of 100 nm, $\Delta\theta_B$ is equal to 0.02 degrees. For practical consideration, an actuator on a mirror mount with 100 tpi (turns per inch) threads, 0.44 degrees constitutes greater than half a turn. Moreover, the wavevector mismatch that occurs with Bragg misalignment scales linearly; hence this angular dispersion will not improve at longer optical wavelengths, nor as optical bandwidths increase.

After implementing the new waveform developed above, a second GVD and TOD scan was performed. A new set of GVD and TOD values were determined to be 0.0441 ps^2 and −0.005 ps^3 for GVD and TOD, respectively. The autocorrelations of pulses produced from the shaper under these conditions are shown in Figure 3.2a and 3.2b. The pulses are measured to be 125 fs in duration, and the envelope returns to being nearly the same shape as the input mid-IR pulse. These pulse durations are similar to those previously reported after applying corrections for temporal dispersion.[26] From this data it is evident that the wavevector mismatch produced in the pulse shaper must be mitigated in order to efficiently shape broadband mid-IR pulses. Since the AOM produces both material dispersion from the Ge crystal and angular dispersion from the varying Bragg angle conditions, both must be accounted for in order to produce short pulses. With short pulses in hand, we moved on to generate pulse pairs required for 2D IR experiments. Autocorrelations of pulse pairs with several different time delays are shown in Figure 3.3a. When an autocorrelation of a pulse pair is performed, three peaks are observed in the trace. There is one large peak present at the middle of the plot resulting from both pulse pairs being temporally overlapped, and there are two side peaks with half of the intensity resulting from one pulse from each pulse pair overlapping. The distance between the middle peak and a side peak is equal to the time delay between the two pulses. A 2D IR spectrum of $W(CO)_6$ in hexane is presented in Figure 3.3b. In addition to our active Bragg-angle compensating waveform in the experiment, phase cycling schemes developed by Zanni and co-workers were employed for transient absorption and scatter removal.[21] Thus, our new waveform does not hamper any previously developed capabilities, nor does it require the use of additional pulses produced by the regenerative amplifier.

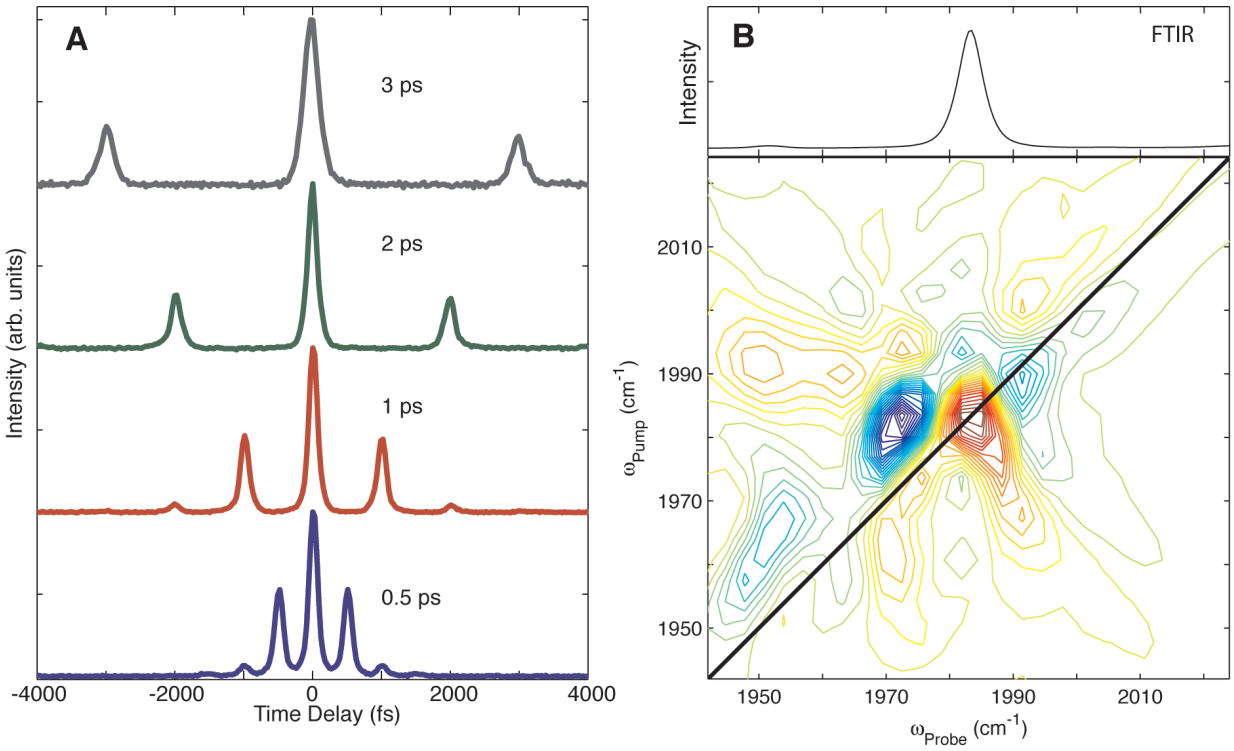

Figure 3.3. (a) Intensity autocorrelations of mid-IR pulse pairs generated using a Bragg angle corrected double pulse mask with pulse pair separations of 0.5 ps, 1 ps, 2 ps, and 3 ps. All autocorrelations are normalized time zero peak. (b) FTIR and 2D-IR spectrum of the carbonyl stretch in $W(CO)_6$ in hexane using the active Bragg-angle compensating pulse pair mask and phase cycling to remove transient absorption and scatter.

3.4. Conclusions

The Ge-AOM is a spatial light modulator that operates in the Bragg regime. As such, the only diffraction order that will have significant light intensity is the first order diffraction line. Further, operating in the Bragg regime requires the incident and diffracted optical fields to meet the acoustic wave front at the Bragg angle. As optical bandwidth broadens to $\lambda_o \pm \Delta\lambda$, angular dispersion is introduced because only λ_o is perfectly set to the Bragg angle. As $\Delta\lambda$ increases, angular misalignment increases, thereby producing increasing amounts of angular dispersion in the pulse.

The effect of angular misalignment is small at visible wavelengths required by multidimensional electronic spectroscopy because the fractional bandwidth in the AOM remains small.[15] However, at mid-IR wavelengths required for multidimensional IR spectroscopy the effect is significant because the fractional bandwidth in the AOM is ten-fold larger. The significance of the angular misalignment only grows as λ_o moves to longer wavelengths, for example far-IR, or the bandwidth, $\Delta\lambda$ increases. We have presented an approach to removing angular misalignment from a Bragg-regime pulse shaper by utilizing a waveform that actively compensates for the change in Bragg angle across the bandwidth of the optical pulse. The resulting acoustic wave in the Ge-AOM forces the acoustic wave front to a position that results in the proper Bragg angle for each optical frequency that is incident on the AOM. This approach to actively correcting the Bragg angle can be generalized to other optical frequencies and is especially promising for making pulse shaping technology compatible with broadband or continuum mid-IR pulsed light sources.

3.5 Additional Notes

This work was supported by the ACS Petroleum Research Foundation (51228-DN16) and through start-up found provided by Colorado State University. J.M. Nite acknowledges the generous support of the Maciel Fellowship Fund.

References

(1) Nite, J. M.; Cyran, J. D.; Krummel, A. T. Active Bragg Angle Compensation for Shaping Ultrafast Mid-Infrared Pulses. *Opt. Express* **2012**, *20* (21), 23912.

(2) Schlau-Cohen, G. S.; Ishizaki, A.; Fleming, G. R. Two-Dimensional Electronic Spectroscopy and Photosynthesis: Fundamentals and Applications to Photosynthetic Light-Harvesting. *Chem. Phys.* **2011**, *386* (1–3), 1–22.

(3) Fidler, A. F.; Harel, E.; Engel, G. S. Dissecting Hidden Couplings Using Fifth-Order Three-Dimensional Electronic Spectroscopy. *J. Phys. Chem. Lett.* **2010**, *1* (19), 2876–2880.

(4) Lewis, K. L. M.; Ogilvie, J. P. Probing Photosynthetic Energy and Charge Transfer with Two-Dimensional Electronic Spectroscopy. *J. Phys. Chem. Lett.* **2012**, *3* (4), 503–510.

(5) Spry, D. B.; Goun, a; Glusac, K.; Moilanen, D. E.; Fayer, M. D. Proton Transport and the Water Environment in Nafion Fuel Cell Membranes and AOT Reverse Micelles. *J. Am. Chem. Soc.* **2007**, *129* (26), 8122–8130.

(6) Bredenbeck, J.; Helbing, J.; Hamm, P. Labeling Vibrations by Light: Ultrafast Transient 2D-IR Spectroscopy Tracks Vibrational Modes during Photoinduced Charge Transfer. *J. Am. Chem. Soc.* **2004**, *126* (4), 990–991.

(7) Pensack, R. D.; Banyas, K. M.; Barbour, L. W.; Hegadorn, M.; Asbury, J. B. Ultrafast Vibrational Spectroscopy of Charge-Carrier Dynamics in Organic Photovoltaic Materials. *Phys. Chem. Chem. Phys. PCCP* **2009**, *11* (15), 2575–2591.

(8) Krummel, A. T.; Zanni, M. T. DNA Vibrational Coupling Revealed with Two-Dimensional Infrared Spectroscopy: Insight into Why Vibrational Spectroscopy Is Sensitive to DNA Structure. *J. Phys. Chem. B* **2006**, *110* (28), 13991–14000.

(9) Yang, M.; Szyc, Ł.; Elsaesser, T. Vibrational Dynamics of the Water Shell of DNA Studied by Femtosecond Two-Dimensional Infrared Spectroscopy. *J. Photochem. Photobiol. Chem.* **2012**, *234* (SI), 49–56.

(10) Shim, S.-H.; Strasfeld, D. B.; Ling, Y. L.; Zanni, M. T. Automated 2D IR Spectroscopy Using a Mid-IR Pulse Shaper and Application of This Technology to the Human Islet Amyloid Polypeptide. *Proc. Natl. Acad. Sci. U. S. A.* **2007**, *104* (36), 14197–14202.

(11) Backus, E. H. G.; Bloem, R.; Donaldson, P. M.; Ihalainen, J. A.; Pfister, R.; Paoli, B.; Caflisch, A.; Hamm, P. 2D-IR Study of a Photoswitchable Isotope-Labeled Alpha-Helix. *J. Phys. Chem. B* **2010**, *114* (10), 3735–3740.

(12) Ganim, Z.; Jones, K. C.; Tokmakoff, A. Insulin Dimer Dissociation and Unfolding Revealed by Amide I Two-Dimensional Infrared Spectroscopy. *Phys. Chem. Chem. Phys. PCCP* **2010**, *12* (14), 3579–3588.

(13) Vaughan, J. C.; Hornung, T.; Stone, K. W.; Nelson, K. A. Coherently Controlled Ultrafast Four-Wave Mixing Spectroscopy. *J. Phys. Chem. A* **2007**, *111* (23), 4873–4883.

(14) Myers, J. A.; Lewis, K. L. M.; Tekavec, P. F. Two-Dimensional Fourier Transform Electronic Spectroscopy with a Pulse-Shaper. **2009**, *92*, 956–958.

(15) Dugan, M. A.; Tull, J. X.; Warren, W. S. High-Resolution Acousto-Optic Shaping of Unamplified and Amplified Femtosecond Laser Pulses. *J. Opt. Soc. Am. B* **1997**, *14* (9), 2348.

(16) Fuji, T.; Suzuki, T. Generation of Sub-Two-Cycle Mid-Infrared Pulses by Four-Wave Mixing through Filamentation in Air. *Opt. Lett.* **2007**, *32* (22), 3330.

(17) Petersen, P. B.; Tokmakoff, A. Source for Ultrafast Continuum Infrared and Terahertz Radiation. *Opt. Lett.* **2010**, *35* (12), 1962.

(18) Cheng, M.; Reynolds, A.; Widgren, H.; Khalil, M. Generation of Tunable Octave-Spanning Mid-Infrared Pulses by Filamentation in Gas Media. *Opt. Lett.* **2012**, *37* (11), 1787.

(19) Calabrese, C.; Stingel, A. M.; Shen, L.; Petersen, P. B. Ultrafast Continuum Mid-Infrared Spectroscopy: Probing the Entire Vibrational Spectrum in a Single Laser Shot with Femtosecond Time Resolution. *Opt. Lett.* **2012**, *37* (12), 2265.

(20) Tian, P.; Keusters, D.; Suzaki, Y.; Warren, W. S. Femtosecond Phase-Coherent Two-Dimensional Spectroscopy. *Science* **2003**, *300* (5625), 1553–1555.

(21) Shim, S. H.; Zanni, M. T. How to Turn Your Pump–probe Instrument into a Multidimensional Spectrometer: 2D IR and Vis Spectroscopiesvia Pulse Shaping. *Phys Chem Chem Phys* **2008**, *11* (5), 748–761.

(22) Tseng, C.; Matsika, S.; Weinacht, T. C. Two-Dimensional Ultrafast Fourier Transform Spectroscopy in the Deep Ultraviolet. *Opt. Express* **2009**, *17* (21), 18788.

(23) Boyd, R. W. *Nonlinear Optics*, 3rd ed.; Academic Press, 2008; p 640.

(24) Gordon, E. I. A Review of Acoustooptical Deflection and Modulation Devices. *Proc. IEEE* **1966**, *54* (10), 1391–1401.

(25) Klein, W.; Cook, B. Unified Approach to Ultrasonic Light Diffraction. *IEEE Trans. Sonics Ultrason.* **1967**, *14* (3), 123.

(26) Shim, S.-H.; Strasfeld, D. B.; Zanni, M. T. Generation and Characterization of Phase and Amplitude Shaped Femtosecond Mid-IR Pulses. *Opt. Express* **2006**, *14* (26), 13120.

(27) Shim, S.-H.; Strasfeld, D. B.; Fulmer, E. C.; Zanni, M. T. Femtosecond Pulse Shaping Directly in the Mid-IR Using Acousto-Optic Modulation. *Opt. Lett.* **2006**, *31* (6), 838–840.

(28) Middleton, C. T.; Woys, A. M.; Mukherjee, S. S.; Zanni, M. T. Residue-Specific Structural Kinetics of Proteins through the Union of Isotope Labeling, Mid-IR Pulse Shaping, and Coherent 2D IR Spectroscopy. *Methods* **2010**, *52* (1), 12–22.

Chapter 4

Characterizing Anharmonic Vibrational Modes of Quinones with Two-Dimensional Infrared Spectroscopy

This chapter is a publication from 2015 and is published in the Journal of Physical Chemistry B.[1] I am the lead author for this work with co-workers Jacob Nite and Amber Krummel. I prepared samples of benzoquinone, naphthoquinone, and anthraquinone used for UV-vis, linear IR absorption and 2D IR experiments. I also completed electronic structure and frequency calculations using Gaussian. We were able to characterize the anharmonic vibrational modes of a quinone series.

4.1. Introduction

Coherent multidimensional infrared spectroscopies, including 2D- and 3D IR spectroscopy, have had a tremendous impact on investigations of solvent dynamics and structure conformational dynamics related to biological systems in the past decade.[2–6] In particular, 2D IR spectroscopy is now a robust tool for probing lipid membranes,[7,8] peptides,[9–11] and proteins.[12–14] Carbonyl groups are strong oscillators that have useful characteristics including being sensitive to local solvent environments, hydrogen bonding, and relative orientations of the oscillators.[15,16] Investigators take advantage of the localized nature of the transition dipole associated with the carbonyl stretching motion in biological molecules in order to monitor structural dynamics under varying conditions. For example, the carbonyl ester in phospholipids reports on the orientation of the phospholipid headgroup[17–19] and, of course, the amide I vibrations of peptides and proteins

are used extensively.[20–24] 2D IR spectroscopy has also been extended to study nucleic acids, albeit to a lesser extent.[25–28] Four of the five nucleotides in DNA and RNA include carbonyl bonds that produce carbonyl stretch vibrations with strong oscillator strengths.[29] However, in the case of nucleic acids, spectral signatures from the carbonyl bonds are complicated by the fact that the transition dipole associated with the in-plane carbonyl stretch is not fully localized along the carbonyl bond but is somewhat delocalized onto the ring structure of the nucleotide base. Thus, prior to using the nucleotide carbonyl stretching vibration as a handle for probing structural dynamics, investigations instead have focused on fully characterizing the anharmonic vibrational modes in single nucleotides and developing models to describe the inter- and intramolecular vibrational coupling in nucleotides and model DNA oligomers.[25,30–32] In reality, there exist many biologically relevant molecules that contain hetero ring structures or highly conjugated ring structures, which may need to be treated similarly to the nucleotides. Quinones are one example of carbonyl containing conjugated ring structures that are ubiquitous in biology.

Quinone derivatives are important molecules in plant, microbial, and mammalian biology. The benzoquinone derivatives, plastoquinone and ubiquinone are required for electron transfer in plant chloroplasts and mitochondrial membranes, respectively.[33,34] Naphthoquinone derivatives give rise to vitamin Ks that are required for post-translational modification of proteins required for blood coagulation and bone health.[35] In addition, anthraquinone derivatives make up drugs that are important in the treatment of malaria and cancer.[36,37] In each of these examples, the quinone performs its role in a complex, condensed phase environment. In order to fully characterize the role of quinones, one must be able to probe their structure and dynamics in their natural environments. 2D IR spectroscopy is particularly well suited to probe these molecules in their native environments because the spectroscopic experiments can be tailored to handle highly

scattering media such as lipid membranes. However, extracting information regarding molecular structure and the surrounding solvent dynamics from a vibrational spectrum requires the vibrational eigenstates of a molecule to be well characterized in order to facilitate the interpretation of the spectral data. In this work, a series of quinones with increasing ring content are investigated and the anharmonic vibrational modes are characterized.

Characteristics of molecular vibrational eigenstates generally fall between two limiting cases: At one limit, the vibrational eigenstates in a molecule can be considered harmonic, normal modes that are anharmonically coupled, and at the second limit the vibrational eigenstates in a molecule can be considered anharmonic, local modes that are harmonically coupled.[38] In reality, many molecular systems, including the quinone series investigated here, have vibrational eigenstates that cannot be described perfectly by either of these limiting cases, but instead lie in between these two limits. Thus, it is important to directly measure the characteristics of the molecular vibrational modes. It has been shown that one can naturally cross over from the first limit to the second limit, but the key parameter to consider is the ratio of vibrational coupling to the anharmonicity of the bond potentials. If vibrational coupling is large relative to the anharmonicity of the potential, the vibrational eigenstate is considered to be in the "near-normal" limit; whereas if vibrational coupling is small relative to the anharmonicity of the potential, the vibrational eigenstate is considered to be in the "near-local" behavior.[38,39] Independent of where the vibrational eigenstates of quinones lie in between these limiting behaviors, the vibrational characteristics of quinones must be reported in order to use them to report on biological structure, dynamics, and function in the future. 2D IR spectroscopy probes the transitions between the ground, first, and second vibrational levels and is thus, sensitive to vibrational coupling and anharmonicity. 2D IR spectroscopy also allows diagonal and off-diagonal

anharmonicities to be observed directly, thereby providing a direct measure of vibrational anharmonicity. In this work, we characterize the anharmonic vibrational characteristics of the in-plane carbonyl stretching and in-plane ring deformations of three quinones: benzoquinone, naphthoquinone, and anthraquinone. The diagonal and off-diagonal anharmonicities of the observed absorption features are extracted from 2D IR spectra collected on this series of molecules. In addition, the magnitudes of vibrational couplings between the carbonyl and ring vibrations are determined.

4.2. Experimental and Computational Methods

4.2.1 Linear IR and 2D IR Spectroscopy

The samples prepared for all linear IR absorption and 2D IR experiments have concentrations of 10.0 mM solute in chloroform. All samples were measured at room temperature and were placed between two CaF_2 plates with a 200-μm-thick Teflon spacer. 1,4-Benzoquinone was purchased from Sigma Aldrich. 1,4-Naphthoquinone and 9,10-anthraquinone were purchased from Acros Organics. Chloroform (ACS grade) was used as the solvent for each sample and purchased from Fisher Scientific. Each sample was in monomeric form; this was confirmed by the lack of spectroscopic features indicative of aggregation in the UV-visible absorption and linear IR absorption spectroscopy experiments. For example, there were no shifts in the UV-vis absorption spectroscopy experiments collected as a function of quinone concentration from 5.0 to 20.0 mM.

Linear IR absorption spectra were collected using a Nicolet 6700 spectrometer (Thermo Fisher Scientific) with 4 cm^{-1} resolution and averaging 64 scans. The spectra were processed using the atmospheric suppression correction in the OMNIC software (Thermo Fisher Scientific). All linear IR absorption spectra have an air background subtracted; in addition, a percentage of

chloroform background was subtracted to ensure solvent peaks were removed. Each linear IR absorption spectrum was baseline corrected by picking two end points and adjusting the end points to zero using a MATLAB program written in-house. The linear IR absorption data and slices extracted from the 2D IR data are fit with Gaussian line shapes using MATLAB minimization tools.

Each quinone sample was probed using 2D IR spectroscopy, where three mid-IR electric fields interact with the sample to generate an electric field that is the third-order signal. The 2D IR spectrometer used in these experiments consists of a Ti:sapphire oscillator used to seed a regenerative chirped pulse amplifier (Wyvern 1000, KM Laboratories) to produce sub-45 fs pulses at a 1 kHz repetition rate; the wavelength of these pulses is centered at 800 nm. The 800 nm pulses pump an optical parametric amplifier (OPA, Light Conversion TOPAS-C) with a difference frequency generation stage ($AgGaS_2$) used to produce tunable mid-IR light. The mid-IR pulses were centered at 6000 nm, had 9 μJ of energy, and were 70 fs in duration as determined by autocorrelation. A 90:10 beamsplitter was used to direct the majority of the IR light to a Ge-acoustic optic modulator (Ge-AOM, Isomet Corporation LS600-1109) based pulse shaper.[40,41] Direct pulse-shaping in the mid-IR is performed with active Bragg angle compensation being utilized. The details of active Bragg angle compensation can be found in ref 41 but are briefly described here. The pulse shaper is set up in a 4-*f* geometry. The mid-IR light is directed onto a grating with a groove density of 100 ln/mm. The diffracted beam is directed toward a cylindrical mirror (129.4 mm f.l.). A 3-inch gold mirror is used to direct the beam into the Ge-AOM at the Bragg angle. The beam is reflected off of identical optics in the second half of the zero dispersion compressor in order to complete the 4-*f* pulse shaper. An arbitrary waveform generator (AWG, DynamicSignals LLC PXDAC4800) is used to generate a Bragg

angle compensated acoustic wave. The Bragg angle compensated waveform takes the instantaneous phase into account in order to perform a frequency sweep of the acoustic wave and thereby minimize angular dispersion in the pulse shaper.[42] The resulting shaped pulses are 134 fs in duration as measured by autocorrelation. A pump-probe beam geometry was used where the beams are reflected off of a 90° parabolic mirror (101.6 mm f.l.). The third order signal is self-heterodyned since it follows the path of the probe beam after the sample and was detected using a linear 64-element mercury cadmium telluride (MCT) array detector. Signal to noise was improved by averaging 300 scans for each sample. The background scatter and transient absorption signals are subtracted from the signal by phase cycling the pump pulses.[43] The w_{pump} axis of the 2D IR spectra is a Fourier transformation of t_1, which is scanned from 0 to 2.5 ps in 7 fs steps with the pulse shaper. The w_{probe} axis is obtained by dispersing the electric field of the third order signal off of a grating in the monochromator and thus transforming the signal into the frequency domain. The w_{probe} axis was calibrated using atmospheric water vapor. The logarithm of a purged spectrum divided by a nonpurged spectrum results in an absorption spectrum similar to a linear IR absorption spectrum. The result of the calibration determines the wavelength at each pixel of the spectrometer. The w_{pump} axis is calibrated with a pump interference spectrum. The three mid-IR electric fields and the emitted electric field of the third-order signal are each polarized parallel to each other. In this experimental geometry, the absorptive 2D IR spectra are recorded.

4.2.2 Computational Methods

All three quinones investigated experimentally were also studied using theoretical calculations. Gas-phase geometry optimizations and frequency calculations were completed using density functional theory (DFT) with the Becke-3-Lee-Yang-Parr (B3LYP) exchange-correlation

functional and second-order Møller-Plesset (MP2) perturbation theory. The basis sets used with each method were 6-31G(d) and 6-311G(d,p). For completeness, calculations were completed with and without the dielectric constant for chloroform. In addition, both harmonic and anharmonic frequency calculations were performed. All calculations were performed in Gaussian 09.[44] Only the data for the DFT B3LYP/6-311G(d,p) anharmonic calculations are included in Table 2. The scaling factor for B3LYP with 6-311G(d,p) is 0.9619.[45] This scaling factor was applied to the calculated frequencies.

4.3. Results and Discussion

The molecular structure and linear IR absorption spectra of benzoquinone, naphthoquinone and anthraquinone are shown in parts a-c of Figure 4.1, respectively. In the spectral region from 1560 to 1710 cm^{-1}, the peaks arise from carbonyl and ring vibrational modes. Traditionally, the lower frequency peaks have been assigned to in-plane ring deformation modes that are dominated by motion along the C=C bonds and the higher frequency peaks have been assigned to the in-plane C=O stretching vibrations.[46] However, other studies have resulted in different assignments for the peaks in the 1560-1710 cm^{-1} spectral region. For instance, studies of benzoquinone have reported the C=C stretching vibration as the higher frequency mode[47] while others have attributed the higher frequency mode to a Fermi resonance.[48] The situation is similar for naphthoquinone and anthraquinone.[49] Thus, the description of the modes in the spectral region from 1560 to 1710 cm^{-1} continues to be debated and complete descriptions of these anharmonic vibrations are needed. As demonstrated in Figure 4.1, the linear IR absorption spectra varied significantly for this series of quinones. Hence, the linear data illustrates the potential for differences in the nuclear motions that contribute to the vibrational modes observed.

As such the traditional labeling of vibrational modes is likely unsuitable for describing the observed vibrational modes in this series of quinones. In order to avoid confusion and to assist in proper identification, the peaks will be referred to by the label, B1, B2, etc., throughout this chapter. The labels for benzoquinone (B1-B3), naphthoquinone (N1-N4) and anthraquinone (A1-A3) are descriptions for the vibrational modes and are noted in Figure 4.1.

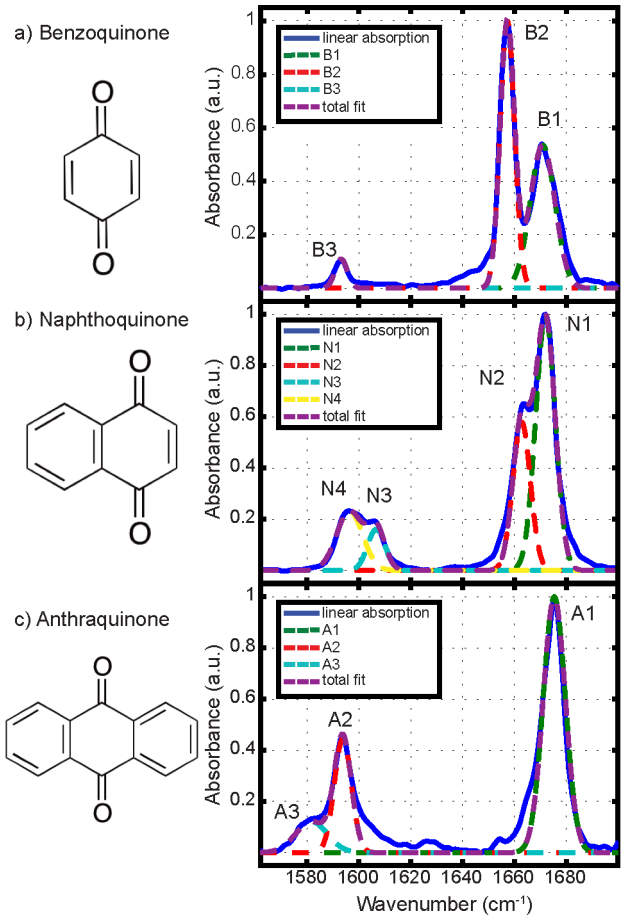

Figure 4.1. Molecular structures and linear spectra with Gaussian fits of benzoquinone, naphthoquinone, and anthraquinone in chloroform.

The peaks for benzoquinone (B1-B3), naphthoquinone (N1-N4), and anthraquinone (A1-A3), illustrated in Figure 4.1 were fit using Gaussian lineshapes where the oscillator strengths, center frequency, and line widths were allowed to vary. The total fit indicated in purple is the sum of the contributing Gaussian fits. The results of these fits are summarized in Table 4.1.

With symmetrically positioned carbonyls on the molecule, if traditional peak assignments hold, there will be two normal modes in the 1650 to 1680 cm^{-1} spectral region due to symmetric and antisymmetric stretches of the carbonyl vibrations. Each quinone in this series has vibrational modes within the spectral region from 1650 to 1680 cm^{-1}; however, there is significant variability in peak positions and intensities. Benzoquinone has two peaks, B1 and B2, with significant intensity. Naphthoquinone has two peaks, N1 and N2, with significant intensity. Anthraquinone has one peak, A1, within the spectral region from 1650 to 1680 cm^{-1} that has significant intensity. Anthraquinone and benzoquinone each have peaks in this region that appear as shoulders on the main peaks; these peaks that appear as shoulders are difficult to resolve from the main peaks and are not expected to contribute vibrational coupling in the molecules due to the weak oscillator strengths that they exhibit. The oscillator strength of each vibrational mode will depend on the extent of orthogonality between the vibrational modes; for example, if the vibrational modes are perpendicular, the oscillator strength will be held completely in either the symmetric or antisymmetric mode. The linear IR spectrum of anthraquinone suggests that anthraquinone is nearing the limit of having orthogonal vibrational modes in this region. This is in contrast to the linear spectra of benzoquinone and naphthoquinone that exhibit significant oscillator strength in both vibrational modes in the 1650-1680 cm^{-1} region.

Benzoquinone, naphthoquinone, and anthraquinone each have vibrations in the region from 1560-1620 cm^{-1} that have been traditionally assigned as symmetric and antisymmetric, in-plane ring deformations that are dominated by C=C bond motions. The lower frequency modes, B3, N3, N4, A2, and A3, exhibit no correlation between the number of rings and the transition dipoles in the lower frequency region. As seen in Figure 4.1, the spectral region from 1560 cm^{-1} to 1710 cm^{-1} evolves from benzoquinone to anthraquinone with only the addition of rings: the peak positions and relative intensities change, thus indicating that each of these vibrational modes contains carbonyl stretching and ring deformation character. Moreover, the integrated intensity from 1560 cm^{-1} to 1710 cm^{-1} remains approximately constant. Therefore, the relative magnitudes of ring deformation and carbonyl stretching character are varying between benzoquinone, naphthoquinone, and anthraquinone. The goal of this chapter is to characterize the differences in the relationship between the ring and carbonyl modes as rings are added in this quinone series. To this end, the vibrational anharmonicity for each mode and the vibrational coupling between each mode will be reported.

In order to understand the mixing of the vibrational modes, 2D IR experiments were completed on benzoquinone, naphthoquinone, and anthraquinone; the spectra are plotted in Figure 4.2a-c. The three transitions of interest in benzoquinone and the four transitions of interest in naphthoquinone occur between 1580 and 1680 cm^{-1} and thus can be probed simultaneously at a spectral resolution of 1.7 cm^{-1} with the spectrometer centered at 1629 cm^{-1}. The three transitions of interest in anthraquinone occur between 1560 and 1700 cm^{-1}; in order to probe these vibrations simultaneously, a grating with a lower groove density (75 lines/mm) was utilized in the 2D IR spectrometer resulting in a spectral resolution of 5.4 cm^{-1}.

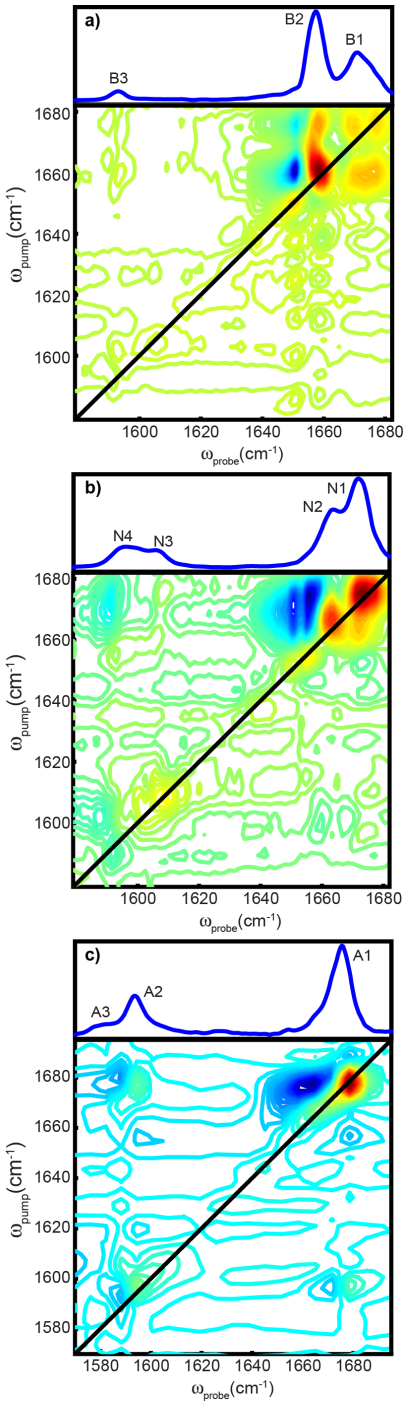

Figure 4.2. Linear and 2D IR spectra of the carbonyl and ring modes of (a) benzoquinone, (b) naphthoquinone, and (c) anthraquinone in chloroform. The 2D IR spectrum of benzoquinone is plotted in 1.8% intervals, and the 2D IR spectra of naphthoquinone and anthraquinone are plotted in 2.5% intervals.

The 2D IR spectra presented here contain peaks along the diagonal and cross peaks that appear off of the diagonal; both types of features come as pairs of peaks. The peak pairs along the diagonal in Figure 4.2 are derived from the v=0 to the v=1 transition (positive in red) and the v=1 to v=2 transition (negative in blue). The pairs of peaks along the diagonal are separated along w_{probe} by the anharmonicity, Δ_i, of the vibrational mode. The cross peaks in the 2D IR spectra also have positive and negative peak pairs, where the pairs of peaks along w_{probe} are separated by the off-diagonal anharmonicity, Δ_{ij}, of the vibrational modes that interact with each other. The presence of cross peaks indicates vibrational coupling between two vibrational modes.

In a 2D IR spectrum, the intensity scales as $I \propto \mu_{0i}^4$ for the diagonal peaks and $I \propto \mu_{0i}^2 \mu_{ij}^2$ for the cross peaks. Thus, the diagonal and cross peaks will not necessarily have the same intensity. The intensity of the cross peaks pumped at a lower frequency is proportional to the square of the dipole strength of the lower frequency modes, which are less intense than the higher frequency modes for the data presented in Figure 4.2. Therefore, cross peaks pumped at lower frequencies are less intense than cross peaks pumped at higher frequencies.

The spectra in Figure 4.2 depict the full spectral range of interest from 1560 to 1700 cm^{-1}. However, the spectra in Figure 4.2 are congested in the higher frequency region, from 1650 to 1680 cm^{-1}. Therefore, 2D IR spectra were also collected of only the high frequency regions considered to be dominated by carbonyl stretching contributions to the vibrational modes. Figure 4.3 depicts the 2D IR spectra of the higher frequency modes collected at the highest spectral resolution of the spectrometer. The spectra of the carbonyl regions are collected with a spectral resolution of 1.7 cm^{-1} and the spectrometer is centered at 1664 cm^{-1} for the series of quinones investigated here. This is specifically advantageous for anthraquinone since the lowest spectral resolution of the spectrometer was used to acquire the spectrum in Figure 4.2c.

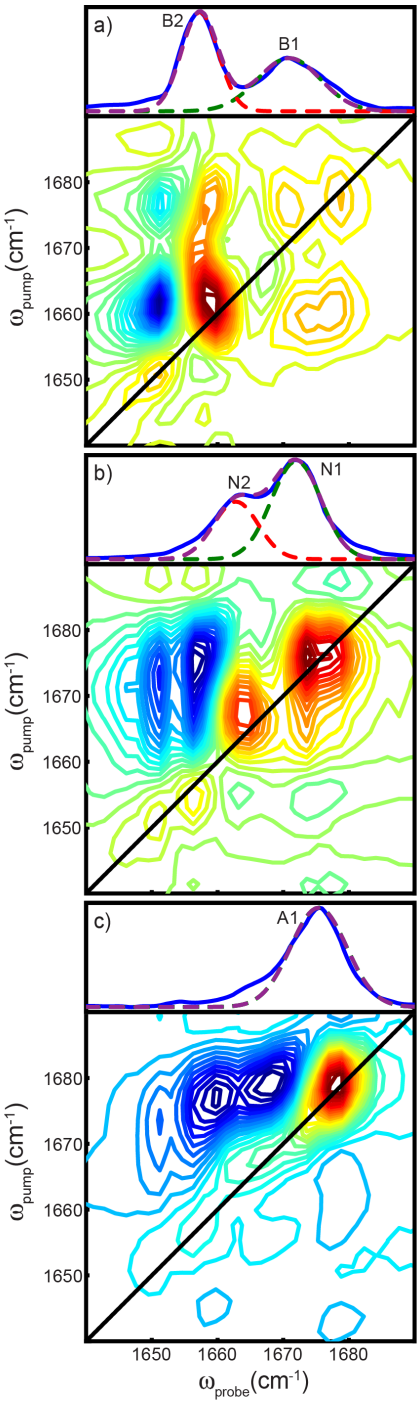

Figure 4.3. Linear and 2D IR spectra of the high frequency modes of (a) benzoquinone, (b) naphthoquinone, and (c) anthraquinone in chloroform. The 2D IR spectrum of benzoquinone is plotted in 3.3% intervals, and the 2D IR spectra of naphthoquinone and anthraquinone are plotted in 4.0% intervals.

The spectra in Figures 4.2 and 4.3 illustrate coupling by the presence of cross peaks. In order to quantitatively describe the coupling of the vibrational modes, the Hamiltonian was inverted to obtain the vibrational coupling values. The diagonal, Δ_i, and off-diagonal, Δ_{ij}, anharmonicities were obtained from slices taken along the ω_{probe}-axis from the 2D IR spectra. Representative ω_{probe}-axis slices are shown in Figure 4.4. The slices were taken from 2D IR spectra collected with a spectral resolution of 1.7 cm^{-1}. The slices were taken at different w_{pump} positions corresponding to peak positions of the fundamental vibrational modes extracted from the linear IR absorption spectra. The slices along the ω_{probe}-axis in Figure 4.4 are representative slices for each quinone and illustrate diagonal and cross peaks. A baseline correction was completed for each slice. The slices shown in Figure 4.4a-c were taken at ω_{pump} = 1671 cm^{-1}, ω_{pump} = 1596 cm^{-1}, and ω_{pump} = 1593 cm^{-1} for benzoquinone, naphthoquinone, and anthraquinone, respectively. The ω_{pump}-axis slices were fit with Gaussian lineshapes to obtain peak positions, full width at half maximum (fwhm) line widths, and peak intensities. The fits were completed using the oscillator strength from the linear absorption spectra for the 0-1 transitions. Normalizing the intensity and taking the fourth root produces the oscillator strength for the slices. The oscillator strengths for the 0-1 transitions of the diagonal peaks in the slices are within 0.06 of the oscillator strengths obtained from the linear absorption spectra. The 1-2 transitions were fit on the basis of the integrated intensity of the 0-1 transition. Therefore, the peak area for the 0-1 transition is the same as the peak area for the 1-2 transition for each peak pair. The slices were taken from both Figures 4.2 and 4.3 to extract the peak positions. Figure 4.3 contains spectra of only the high frequency modes. Therefore, the slices from Figure 4.3 are used to extract the higher frequency peaks positions with less ambiguity. All slices and fully tabulated results can be found in the Supplemental Information. The peak positions are used to

calculate anharmonicities. The diagonal and off-diagonal anharmonicities are calculated by taking the difference in energies of the positive and negative peak pairs along the w_{probe} axis. The anharmonicities are used as starting parameters for the numerical solution of the Hamiltonians. Unfortunately, one diagonal anharmonicity (Δ_{N3}) and five off-diagonal anharmonicities (Δ_{N1N3}, Δ_{N2N3}, Δ_{N3N4}, Δ_{A2A3}, Δ_{A1A3}) cannot be determined from these experiments due to spectral congestion and weak oscillator strengths. However, the diagonal and off-diagonal anharmonicities can also be determined by inverting the 2-Quantum Hamiltonian. The diagonal or off-diagonal anharmonicities are given in Table 4.1.

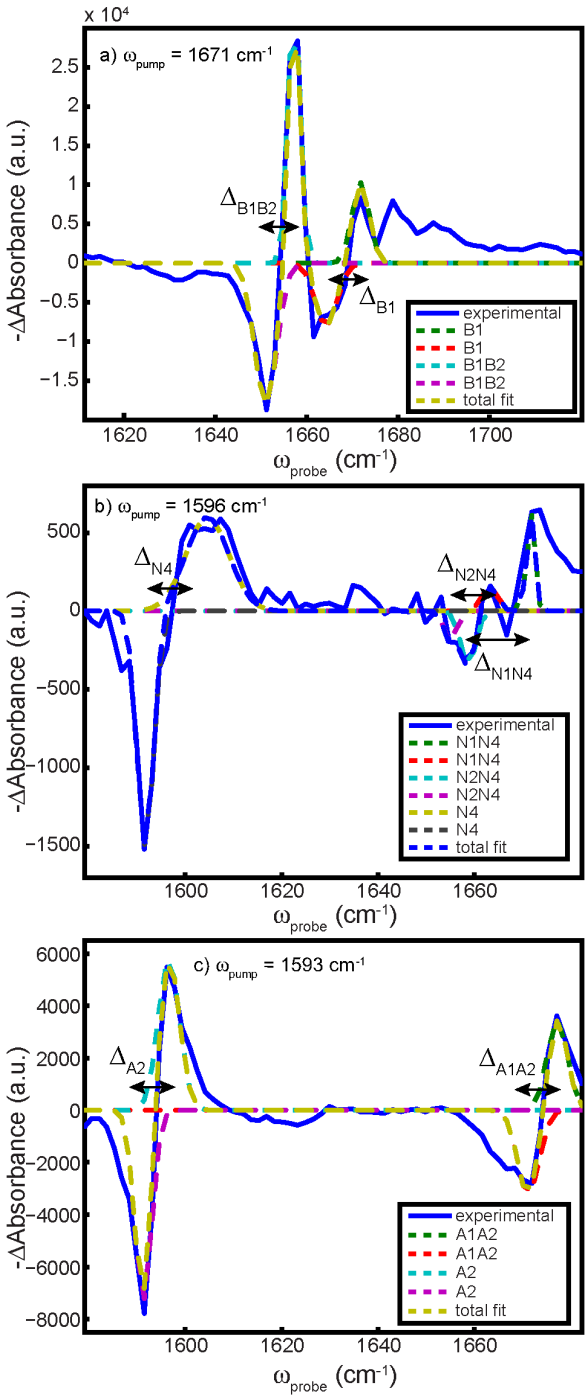

Figure 4.4a-c. Representative slices along the ω_{probe} axis from the 2D IR spectra are presented with fits to each peak pair for benzoquinone, naphthoquinone, and anthraquinone in chloroform. These slices illustrate both diagonal and cross peaks from which diagonal and off-diagonal anharmonicities were extracted.

Table 4.1. Extracted anharmonicities of quinones from 2D IR experiments. Vibrational coupling obtained from inverting the Hamiltonian.

quinone	modes[a]	ω(cm^{-1})	Δω (cm^{-1})[b]	β(cm^{-1})[c]
benzoquinone	B1	1670.9	7.6 ± 0.2	
	B2	1657.3	9.0 ± 0.2	
	B3	1593.1	4.6 ± 0.7	
	B1B2		6.2 ± 0.1	4.6
	B1B3		4.6 ± 0.2	23.6
	B2B3		5.7 ± 0.2	2.5
naphthoquinone	N1	1672.0	17.4 ± 1.0	
	N2	1662.8	13.7 ± 0.2	
	N3	1606.7	1.3[d]	
	N4	1596.4	12.9 ± 0.4	
	N1N2		17.1 ± 0.3	3.3
	N1N3		8.0[d]	2.9
	N1N4		12.9 ± 0.6	7.1
	N2N3		0.5[d]	3.2
	N2N4		8.2 ± 0.3	13.0
	N3N4		12.4[d]	5.9
anthraquinone	A1	1675.4	13.2 ± 0.2	
	A2	1593.8	6.0 ± 0.1	
	A3	1581.7	6.0[d]	
	A1A2		5.3 ± 0.5	11.8
	A1A3		4.0[d]	11.3
	A2A3		8.9[d]	7.3

[a]Normal mode labels are noted in Figure 4.1.

[b]Anharmonicities extracted from Gaussian line shape fits of 2D IR slices in Figure 4.4 and the figures illustrated in the Supporting Information.

[c]Vibrational coupling extracted from inverting the Hamiltonian.

[d]Anharmonicity obtained from inverting the Hamiltonian for the numerical solution.

A platform for comparing the quinones in this series is provided now that the anharmonic characteristics of the vibrational modes in the 1560 cm^{-1} to 1700 cm^{-1} region have been quantified. In this series, benzoquinone and anthraquinone are symmetric molecules, whereas naphthoquinone is asymmetric. In the symmetric benzoquinone and anthraquinone, the high frequency modes have larger diagonal anharmonicities than the low frequency modes. In contrast, the diagonal anharmonicities of the high frequency and low frequency modes are similar in the asymmetric naphthoquinone. These observations have implications on the localized nature of the vibration as well as whether or not these vibrational modes can be depicted by one of the two limiting cases noted above—namely the "near-normal" mode or "near-local" mode pictures. In order to complete the characterization of these vibrational modes in this series of quinones, the magnitude of vibrational coupling between the low and high frequency vibrational modes must be considered.

Inverting the Hamiltonian is one way to calculate the vibrational couplings. The Hamiltonian was inverted by assuming degenerate carbonyl energies and degenerate ring energies for each quinone. The coupling constants were varied until the normal mode energies matched the fundamental frequencies obtained from the linear absorption spectra. The problem with this approach is that the intensities of the transition dipoles are not taken into account. To properly account for the intensities of the transition dipoles, polarization must be completed to find the angle of the transition dipoles.

The vibrational coupling calculated by inverting the Hamiltonian is reported in Table 4.1 for each quinone. For benzoquinone, the vibrational coupling between B1 and B3 is 23.6 cm^{-1}, and between B2 and B3, it is 2.5 cm^{-1}. For naphthoquinone, the vibrational coupling between N1 and N3 is 2.9 cm^{-1}, that between N1 and N4 is 7.1 cm^{-1}, that between N2 and N3 is 3.2 cm^{-1}, and that

between N2 and N4 is 13.0 cm^{-1}. For anthraquinone, the vibrational coupling between A1 and A2 is 11.8 cm^{-1}, that between A1 and A3 is 11.3 cm^{-1}, and that between A2 and A3 is 7.3 cm^{-1}. The magnitudes of the vibrational coupling constants determined from the experiments presented in this work are comparable to the magnitudes of the vibrational coupling between in-plane ring deformation and carbonyl stretching modes in the bases of nucleic acids.[31] For each quinone in this series, the magnitudes of the vibrational coupling between the high and low frequency modes considered are large relative to the diagonal anharmonicities of each mode. This result is perhaps not surprising, considering the extent to which the carbonyl bond stretching motion could be mechanically coupled to the in-plane ring stretching motions in these quinones. The magnitudes of the vibrational coupling constants are large relative to the anharmonicities extracted; thus, the vibrational modes probed in this work are tending toward the "near-normal" mode limit.

The magnitudes of the vibrational coupling between two of the high frequency vibrational modes present in benzoquinone were also determined from these experiments. The vibrational coupling constant that describes the interaction between modes B1 and B2 in benzoquinone is equal to 4.6 cm^{-1}. The magnitude of the vibrational coupling constant is of the same order of the diagonal anharmonicities of the modes contributing to the interaction. In this situation, it is difficult to determine the extent to which the vibrational motion is delocalized from the carbonyl stretch across the in-plane ring motions.

The coupling between naphthoquinone modes N1 and N2 extracted from inverting the Hamiltonian is 3.3 cm^{-1}. The magnitude of the vibrational coupling constant is not of the same order of the diagonal anharmonicities of the modes contributing to the interaction. The zero, first, and second energies from the numerical solution are illustrated in Figure 4.5.

Having quantified the diagonal and off-diagonal anharmonicities for benzoquinone, naphthoquinone, and anthraquinone, energy level diagrams for each quinone can be generated. In Figure 4.5, energy level diagrams are shown for benzoquinone, naphthoquinone and anthraquinone. The energy diagrams illustrated in Figure 4.5 are the relevant energy levels for each quinone probed with 2D IR spectroscopy. The v=2 energy states were calculated using the 0-1 transition energy and the anharmonicity extracted from the 2D IR spectra. The anharmonicities involving N3 and A3 could not be extracted from the 2D IR spectra; the anharmonicities from inverting the 2-Quantum Hamiltonian were used for transitions involving N3 and A3.

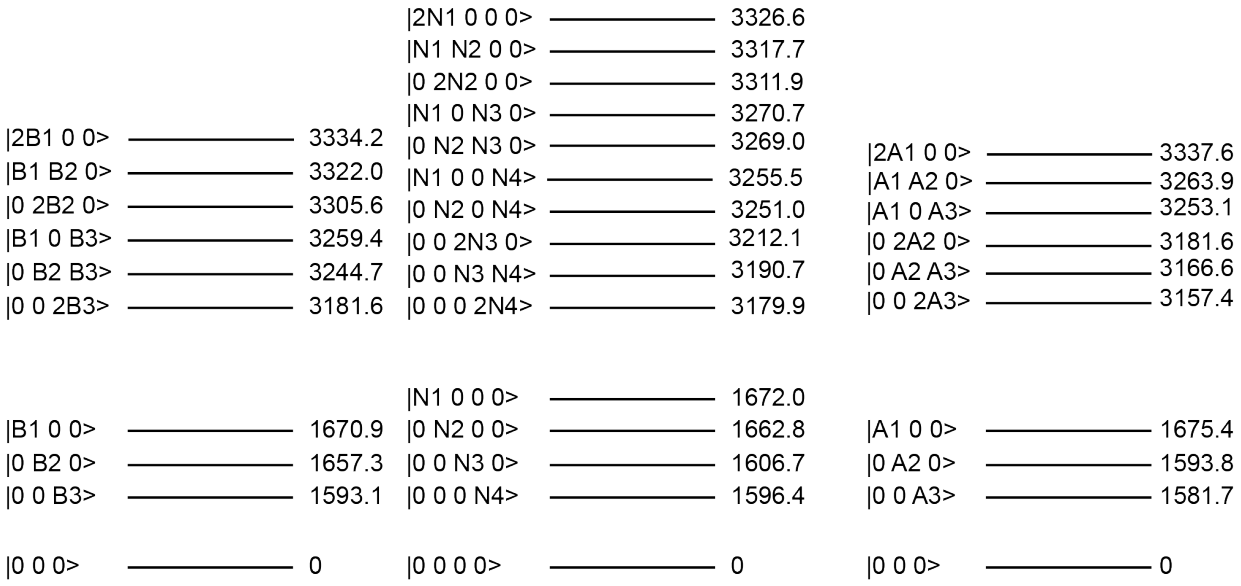

Figure 4.5. Energy level diagrams illustrating the zero, first, and second vibrational energy levels of (a) benzoquinone, (b) naphthoquinone, and (c) anthraquinone. The *v*=2 states are calculated from using the anharmonicities shown in Table 4.1.

4.4. Comparing Experiment and Theory

Along with the linear IR absorption and 2D IR spectroscopy experiments, the quinones in this series were also studied using quantum mechanical calculations. The center vibrational frequencies and oscillator strengths obtained by fitting the linear IR absorption data can be compared to the calculated vibrational frequencies and oscillator strengths for each vibrational mode considered in this work. Benzoquinone and anthraquinone have three vibrational modes to consider, while naphthoquinone has four vibrational modes to consider in the spectral region from 1560 to 1700 cm^{-1} corresponding to the modes labeled in Figure 4.1. The parameters from the fits in Figure 4.1 are found in Table 4.2. The peak intensities are converted into dipole strength according to the scaling $I \propto \mu^2$.[50] The relative oscillator strengths and the center vibrational frequencies from the linear experimental data are compared to the theoretical data for each normal mode of interest. In general, the high frequency modes are known to be dominated by the carbonyl stretching motion and the low frequency modes are dominated by in-plane ring deformations involving C=C and C—C stretching motions.

Table 4.2. Comparison of Experimental and Theoretical Results.

peak	experimental[a]		DFT/6-311G(d,p)		vibrations[c]
	$\omega(cm^{-1})$	μ^b	$\omega(cm^{-1})$	μ^b	
benzoquinone					
B1	1670.9	0.72	1643.3	1.00	C=O(asym),C=C,C-C
B2	1657.3	1.00	1646.1	0.01	C=O(sym),C=C,C-C
B3	1593.1	0.33	1578.0	0.01	C=C,C-C
naphthoquinone					
N1	1672.0	1.00	1641.2	1.00	C=O(asym),C=C,C-C
N2	1662.8	0.78	1638.6	0.16	C=O(sym),C=C,C-C
N3	1606.7	0.40	1568.9	0.29	C=C,C-C
N4	1596.4	0.48	1539.8	0.37	C=O(sym),C=C,C-C
anthraquinone					
A1	1675.4	1.00	1647.9	1.00	C=O(asym),C=C,C-C
A2	1593.8	0.67	1538.9	0.00	C=C,C-C
A3	1581.7	0.35	1534.5	0.63	C=O(asym),C=C,C-C

[a]The experimental data are from the linear fits in Figure 4.1. [b]The dipole strengths are calculated from the square root of the normalized intensities. [c]The vibrations are obtained from the calculations and are the major contributors to each mode.

In this series of quinones, benzoquinone and anthraquinone are highly symmetric molecules, which is in contrast to naphthoquinone. There are significant differences between the experimental and theoretical data with most of the differences occurring in the data related to benzoquinone and anthraquinone. In order to avoid using symmetry arguments to improve the speed of these calculations and thus potentially bias the results of the quantum mechanical calculations, the no symmetry condition in Gaussian 09 was applied. The vibrational frequencies and oscillator strengths from anharmonic frequency calculations for each quinone are provided in Table 4.2. Comparing observables including relative oscillator strengths and energies of each mode, one can quickly notice the deviation between the experimental and theoretical data.

In the symmetric quinones, benzoquinone and anthraquinone, the frequencies of the vibrations calculated are reasonable comparisons to the center frequencies of the observed modes. The calculated vibrations are in better agreement for the higher frequency transitions than the lower frequency transitions within the spectral region of 1560 to 1700 cm^{-1}. The anthraquinone calculations correctly estimate the high frequency modes to carry the greatest oscillator strength, but one of the vibrational frequencies is estimated to carry no oscillator strength. The calculated oscillator strengths for benzoquinone significantly deviate from experiment.

In contrast to benzoquinone and anthraquinone, the theoretical vibrational frequency calculations of naphthoquinone agree quite well with the experimentally observed vibrational modes. The DFT calculation closely resembles the center frequencies and relative oscillator strengths observed for naphthoquinone. The 6-311G(d,p) basis set improves the center frequencies and maintains reasonable oscillator strengths. Inspection of the magnitudes of the nuclear motion in the four vibrational modes of interest provides insight as to why there is good agreement between theory and experiment in the case of naphthoquinone. The vibrational modes

calculated for naphthoquinone each contain carbonyl stretching character and in-plane ring deformation character. Thus, the extent of delocalization or mixing of modes is better estimated in the theoretical calculations of naphthoquinone. It is important to note that performing these calculations with the addition of the dielectric constant for the chloroform solvent did not change the essential results for each quinone calculation.

4.5. Conclusions

2D IR spectroscopy provides a means to directly measure the anharmonic characteristics of quinone vibrational modes that lie between 1560 and 1710 cm^{-1}. Benzoquinone, naphthoquinone, and anthraquinone each have vibrational modes that lie in this region which are generally attributed to carbonyl stretching vibrations at high frequencies and in-plane ring deformations at lower frequencies. The diagonal and off-diagonal anharmonicities were quantified for the quinones investigated in this work. Subsequently, the magnitudes of the vibrational coupling constants between the high and low frequency modes were estimated. 2D IR measurements illustrate the delocalization of the ring and carbonyl contributions to quinone vibrational modes between 1560 and 1710 cm^{-1}. The characterization of the quinones in this chapter rely solely on the experimental analysis from the linear and 2D IR spectra due to the differences between theoretical frequency calculations and the experimental results. However, it is important to note in the case of these quinones that as the vibrations become more localized or the symmetry of the molecule is decreased, the agreement between the theoretical calculations and the experiments presented here is improved. Certainly work toward determining the relative orientation of the vibrational transition dipoles in these quinones needs to be completed. To this end, we are currently implementing polarization control between the laser pulses in our 2D IR

spectrometer. The characterization of the quinones in this chapter provides an important picture of the vibrational states in the region between 1560 and 1710 cm^{-1}. Moreover, understanding the manner in which anharmonicity and vibrational coupling contributes to the mixing of contributions from the in-plane ring deformations and carbonyl stretching vibrations in quinones forms the foundation to investigating quinone derivatives, such as plastoquinone and vitamin K.

4.6 Additional Notes

The authors thank Tony Rappé for access to their cluster and helpful discussions regarding the Gaussian calculations. We also wish to thank Melissa Reynolds for open access to the linear IR absorption and UV-visible absorption spectrometers. A. T. Krummel appreciates the generous funding for this work from the ACS Petroleum Research Fund (grant #51228-DNI6)

References

(1) Cyran, J. D.; Nite, J. M.; Krummel, A. T. Characterizing Anharmonic Vibrational Modes of Quinones with Two-Dimensional Infrared Spectroscopy. *J. Phys. Chem. B* **2015**.

(2) Ghosh, A.; Remorino, A.; Tucker, M. J.; Hochstrasser, R. M. 2D IR Photon Echo Spectroscopy Reveals Hydrogen Bond Dynamics of Aromatic Nitriles. *Chem. Phys. Lett.* **2009**, *469* (4–6), 325–330.

(3) Fayer, M. D. Dynamics of Liquids, Molecules, and Proteins Measured with Ultrafast 2D IR Vibrational Echo Chemical Exchange Spectroscopy. *Annu. Rev. Phys. Chem.* **2009**, *60* (1), 21–38.

(4) Demirdöven, N.; Cheatum, C. M.; Chung, H. S.; Khalil, M.; Knoester, J.; Tokmakoff, A. Two-Dimensional Infrared Spectroscopy of Antiparallel B-Sheet Secondary Structure. *J. Am. Chem. Soc.* **2004**, *126* (25), 7981–7990.

(5) Moran, S. D.; Woys, A. M.; Buchanan, L. E.; Bixby, E.; Decatur, S. M.; Zanni, M. T. Two-Dimensional IR Spectroscopy and Segmental 13C Labeling Reveals the Domain Structure of Human γD-Crystallin Amyloid Fibrils. *Proc. Natl. Acad. Sci.* **2012**, *109* (9), 3329–3334.

(6) Garrett-Roe, S.; Perakis, F.; Rao, F.; Hamm, P. Three-Dimensional Infrared Spectroscopy of Isotope-Substituted Liquid Water Reveals Heterogeneous Dynamics. *J. Phys. Chem. B* **2011**, *115* (21), 6976–6984.

(7) Osborne, D. G.; Dunbar, J. A.; Lapping, J. G.; White, A. M.; Kubarych, K. J. Site-Specific Measurements of Lipid Membrane Interfacial Water Dynamics with Multidimensional Infrared Spectroscopy. *J. Phys. Chem. B* **2013**, *117* (49), 15407–15414.

(8) Ghosh, A.; Wang, J.; Moroz, Y. S.; Korendovych, I. V.; Zanni, M.; DeGrado, W. F.; Gai, F.; Hochstrasser, R. M. 2D IR Spectroscopy Reveals the Role of Water in the Binding of Channel-Blocking Drugs to the Influenza M2 Channel. *J. Chem. Phys.* **2014**, *140* (23), 235105.

(9) Lessing, J.; Roy, S.; Reppert, M.; Baer, M.; Marx, D.; Jansen, T. L. C.; Knoester, J.; Tokmakoff, A. Identifying Residual Structure in Intrinsically Disordered Systems: A 2D IR Spectroscopic Study of the GVGXPGVG Peptide. *J. Am. Chem. Soc.* **2012**, *134* (11), 5032–5035.

(10) Sengupta, N.; Maekawa, H.; Zhuang, W.; Toniolo, C.; Mukamel, S.; Tobias, D. J.; Ge, N.-H. Sensitivity of 2D IR Spectra to Peptide Helicity: A Concerted Experimental and Simulation Study of an Octapeptide. *J. Phys. Chem. B* **2009**, *113* (35), 12037–12049.

(11) Hamm, P.; Lim, M.; DeGrado, W. F.; Hochstrasser, R. M. The Two-Dimensional IR Nonlinear Spectroscopy of a Cyclic Penta-Peptide in Relation to Its Three-Dimensional Structure. *Proc. Natl. Acad. Sci.* **1999**, *96* (5), 2036–2041.

(12) Bredenbeck, J.; Helbing, J.; Nienhaus, K.; Nienhaus, G. U.; Hamm, P. Protein Ligand Migration Mapped by Nonequilibrium 2D-IR Exchange Spectroscopy. *Proc. Natl. Acad. Sci. U. S. A.* **2007**, *104* (36), 14243–14248.

(13) Mukherjee, P.; Kass, I.; Arkin, I. T.; Zanni, M. T. Picosecond Dynamics of a Membrane Protein Revealed by 2D IR. *Proc. Natl. Acad. Sci. U. S. A.* **2006**, *103* (10), 3528–3533.

(14) Ishikawa, H.; Kim, S.; Kwak, K.; Wakasugi, K.; Fayer, M. D. Disulfide Bond Influence on Protein Structural Dynamics Probed with 2D-IR Vibrational Echo Spectroscopy. *Proc. Natl. Acad. Sci.* **2007**, *104* (49), 19309–19314.

(15) Kim, Y. S.; Hochstrasser, R. M. Applications of 2D IR Spectroscopy to Peptides, Proteins, and Hydrogen-Bond Dynamics†. *J. Phys. Chem. B* **2009**, *113* (24), 8231–8251.

(16) Baiz, C. R.; McRobbie, P. L.; Anna, J. M.; Geva, E.; Kubarych, K. J. Two-Dimensional Infrared Spectroscopy of Metal Carbonyls. *Acc. Chem. Res.* **2009**, *42* (9), 1395–1404.

(17) Volkov, V. V.; Chelli, R.; Zhuang, W.; Nuti, F.; Takaoka, Y.; Papini, A. M.; Mukamel, S.; Righini, R. Electrostatic Interactions in Phospholipid Membranes Revealed by Coherent 2D IR Spectroscopy. *Proc. Natl. Acad. Sci.* **2007**, *104* (39), 15323–15327.

(18) Zhao, W.; Moilanen, D. E.; Fenn, E. E.; Fayer, M. D. Water at the Surfaces of Aligned Phospholipid Multibilayer Model Membranes Probed with Ultrafast Vibrational Spectroscopy. *J. Am. Chem. Soc.* **2008**, *130* (42), 13927–13937.

(19) Costard, R.; Greve, C.; Heisler, I. A.; Elsaesser, T. Ultrafast Energy Redistribution in Local Hydration Shells of Phospholipids: A Two-Dimensional Infrared Study. *J. Phys. Chem. Lett.* **2012**, *3* (23), 3646–3651.

(20) Hamm, P.; Lim, M.; Hochstrasser, R. M. Structure of the Amide I Band of Peptides Measured by Femtosecond Nonlinear-Infrared Spectroscopy. *J. Phys. Chem. B* **1998**, *102* (31), 6123–6138.

(21) Ham, S.; Cho, M. Amide I Modes in the N-Methylacetamide Dimer and Glycine Dipeptide Analog: Diagonal Force Constants. *J. Chem. Phys.* **2003**, *118* (15), 6915–6922.

(22) DeCamp, M. F.; DeFlores, L.; McCracken, J. M.; Tokmakoff, A.; Kwac, K.; Cho, M. Amide I Vibrational Dynamics of N-Methylacetamide in Polar Solvents: The Role of Electrostatic Interactions. *J. Phys. Chem. B* **2005**, *109* (21), 11016–11026.

(23) Lin, Y.-S.; Shorb, J. M.; Mukherjee, P.; Zanni, M. T.; Skinner, J. L. Empirical Amide I Vibrational Frequency Map: Application to 2D-IR Line Shapes for Isotope-Edited Membrane Peptide Bundles†. *J. Phys. Chem. B* **2009**, *113* (3), 592–602.

(24) Bagchi, S.; Falvo, C.; Mukamel, S.; Hochstrasser, R. M. 2D-IR Experiments and Simulations of the Coupling between Amide-I and Ionizable Side Chains in Proteins: Application to the Villin Headpiece. *J. Phys. Chem. B* **2009**, *113* (32), 11260–11273.

(25) Krummel, A. T.; Mukherjee, P.; Zanni, M. T. Inter and Intrastrand Vibrational Coupling in DNA Studied with Heterodyned 2D-IR Spectroscopy. *J. Phys. Chem. B* **2003**, *107* (35), 9165–9169.

(26) Elsaesser, T. Two-Dimensional Infrared Spectroscopy of Intermolecular Hydrogen Bonds in the Condensed Phase. *Acc. Chem. Res.* **2009**, *42* (9), 1220–1228.

(27) Dwyer, J. R.; Szyc, Ł.; Nibbering, E. T. J.; Elsaesser, T. Ultrafast Vibrational Dynamics of Adenine-Thymine Base Pairs in DNA Oligomers. *J. Phys. Chem. B* **2008**, *112* (36), 11194–11197.

(28) Yang, M.; Szyc, Ł.; Röttger, K.; Fidder, H.; Nibbering, E. T. J.; Elsaesser, T.; Temps, F. Dynamics and Couplings of N−H Stretching Excitations of Guanosine−Cytidine Base Pairs in Solution. *J. Phys. Chem. B* **2011**, *115* (18), 5484–5492.

(29) Mantsch, H. H.; Chapman, D. *Infrared Spectroscopy of Biomolecules*; Wiley-Liss, 1996.

(30) Krummel, A. T.; Zanni, M. T. Evidence for Coupling between Nitrile Groups Using DNA Templates: A Promising New Method for Monitoring Structures with Infrared Spectroscopy. *J. Phys. Chem. B* **2008**, *112* (5), 1336–1338.

(31) Peng, C. S.; Jones, K. C.; Tokmakoff, A. Anharmonic Vibrational Modes of Nucleic Acid Bases Revealed by 2D IR Spectroscopy. *J. Am. Chem. Soc.* **2011**, *133* (39), 15650–15660.

(32) Lee, C.; Park, K.-H.; Cho, M. Vibrational Dynamics of DNA. I. Vibrational Basis Modes and Couplings. *J. Chem. Phys.* **2006**, *125* (11), 114508.

(33) Allen, J. F.; Bennett, J.; Steinback, K. E.; Arntzen, C. J. Chloroplast Protein Phosphorylation Couples Plastoquinone Redox State to Distribution of Excitation Energy between Photosystems. *Nature* **1981**, *291* (5810), 25–29.

(34) Kussmaul, L.; Hirst, J. The Mechanism of Superoxide Production by NADH:ubiquinone Oxidoreductase (complex I) from Bovine Heart Mitochondria. *Proc. Natl. Acad. Sci.* **2006**, *103* (20), 7607–7612.

(35) Morris, D. P.; Stevens, R. D.; Wright, D. J.; Stafford, D. W. Processive Post-Translational Modification VITAMIN K-DEPENDENT CARBOXYLATION OF A PEPTIDE SUBSTRATE. *J. Biol. Chem.* **1995**, *270* (51), 30491–30498.

(36) Winter, R. W.; Cornell, K. A.; Johnson, L. L.; Isabelle, L. M.; Hinrichs, D. J.; Riscoe, M. K. Hydroxy-Anthraquinones as Antimalarial Agents. *Bioorg. Med. Chem. Lett.* **1995**, *5* (17), 1927–1932.

(37) El-Gogary, T. M. Molecular Complexes of Some Anthraquinone Anti-Cancer Drugs: Experimental and Computational Study. *Spectrochim. Acta. A. Mol. Biomol. Spectrosc.* **2003**, *59* (5), 1009–1015.

(38) Child, M. S.; Lawton, R. T. Local and Normal Vibrational States: A Harmonically Coupled Anharmonic-Oscillator Model. *Faraday Discuss. Chem. Soc.* **1981**, *71* (0), 273–285.

(39) Hamm, P.; Hochstrasser, R. M. Structure and Dynamics of Proteins and Peptides: Femtosecond Two-Dimenaional Infrared Spectroscopy. In *Ultrafast Infrared And Raman Spectroscopy*; Fayer, M. D., Ed.; Marcel Dekker: New York, 2001; pp 273–347.

(40) Shim, S.-H.; Strasfeld, D. B.; Fulmer, E. C.; Zanni, M. T. Femtosecond Pulse Shaping Directly in the Mid-IR Using Acousto-Optic Modulation. *Opt. Lett.* **2006**, *31* (6), 838–840.

(41) Shim, S.-H.; Strasfeld, D. B.; Zanni, M. T. Generation and Characterization of Phase and Amplitude Shaped Femtosecond Mid-IR Pulses. *Opt. Express* **2006**, *14* (26), 13120–13130.

(42) Nite, J. M.; Cyran, J. D.; Krummel, A. T. Active Bragg Angle Compensation for Shaping Ultrafast Mid-Infrared Pulses. *Opt. Express* **2012**, *20* (21), 23912.

(43) Shim, S.-H.; Zanni, M. T. How to Turn Your Pump–probe Instrument into a Multidimensional Spectrometer: 2D IR and Vis Spectroscopies via Pulse Shaping. *Phys. Chem. Chem. Phys.* **2009**, *11* (5), 748–761.

(44) Frisch, M. J.; Trucks, G. W.; Schlegel, H. B.; Scuseria, G. E.; Robb, M. A.; Cheeseman, J. R.; Scalmani, G.; Barone, V.; Mennucci, B.; Petersson, G. A.; et al. *Gaussian 09 Revision D.01*.

(45) Andersson, M. P.; Uvdal, P. New Scale Factors for Harmonic Vibrational Frequencies Using the B3LYP Density Functional Method with the Triple-Z Basis Set 6-311+G(d,p). *J. Phys. Chem. A* **2005**, *109* (12), 2937–2941.

(46) Josien, M.-L.; Fuson, N.; Lebas, J.-M.; Gregory, T. M. An Infrared Spectroscopic Study of the Carbonyl Stretching Frequency in a Group of Ortho and Para Quinones. *J. Chem. Phys.* **2004**, *21* (2), 331–340.

(47) Anno, T. Molecular Vibrations of Quinones. V. Normal Coordinate Analysis of P-Benzoquinone and Its Isotopic Derivatives. *J. Chem. Phys.* **1965**, *42* (3), 932.

(48) Dunn, T. M.; Francis, A. H. The Ground State Fundamentals of P-Benzoquinone and P-Benzoquinone-d4. *J. Mol. Spectrosc.* **1974**, *50* (1–3), 1–13.

(49) Singh, S. N.; Singh, R. S. Vibrational Spectra of Condensed Ring quinones—I 1,4-Naphthoquinone and 9,10-Anthraquinone. *Spectrochim. Acta Part Mol. Spectrosc.* **1968**, *24* (10), 1591–1597.

(50) Wilson, E. B.; Decius, J. C.; Cross, P. C. *Molecular Vibrations: The Theory of Infrared and Raman Vibration Spectra*; Dover: Mineola (N.Y.), 1980.

Chapter 4 Supplemental Materials

The remaining slices along w_{probe} are illustrated in Figure S4.1-3. These slices were used to extract diagonal and off-diagonal anharmonicities. The Figures S4.1-3 are slices from Figures 4.2a-c and 4.3a-c found in the paper. The slices from Figure 4.2a-c include both ring and carbonyl modes. However, the slices are also taken from Figure 4.3a-c to only look at the higher frequency modes. The supplemental tables contain the fitting parameters, including peak postion, FWHM and dipole strength, used to fit the slices in the supplemental figures as well as Figure 4.4a-c. The slices along w_{probe} were fit with Gaussian lineshapes.

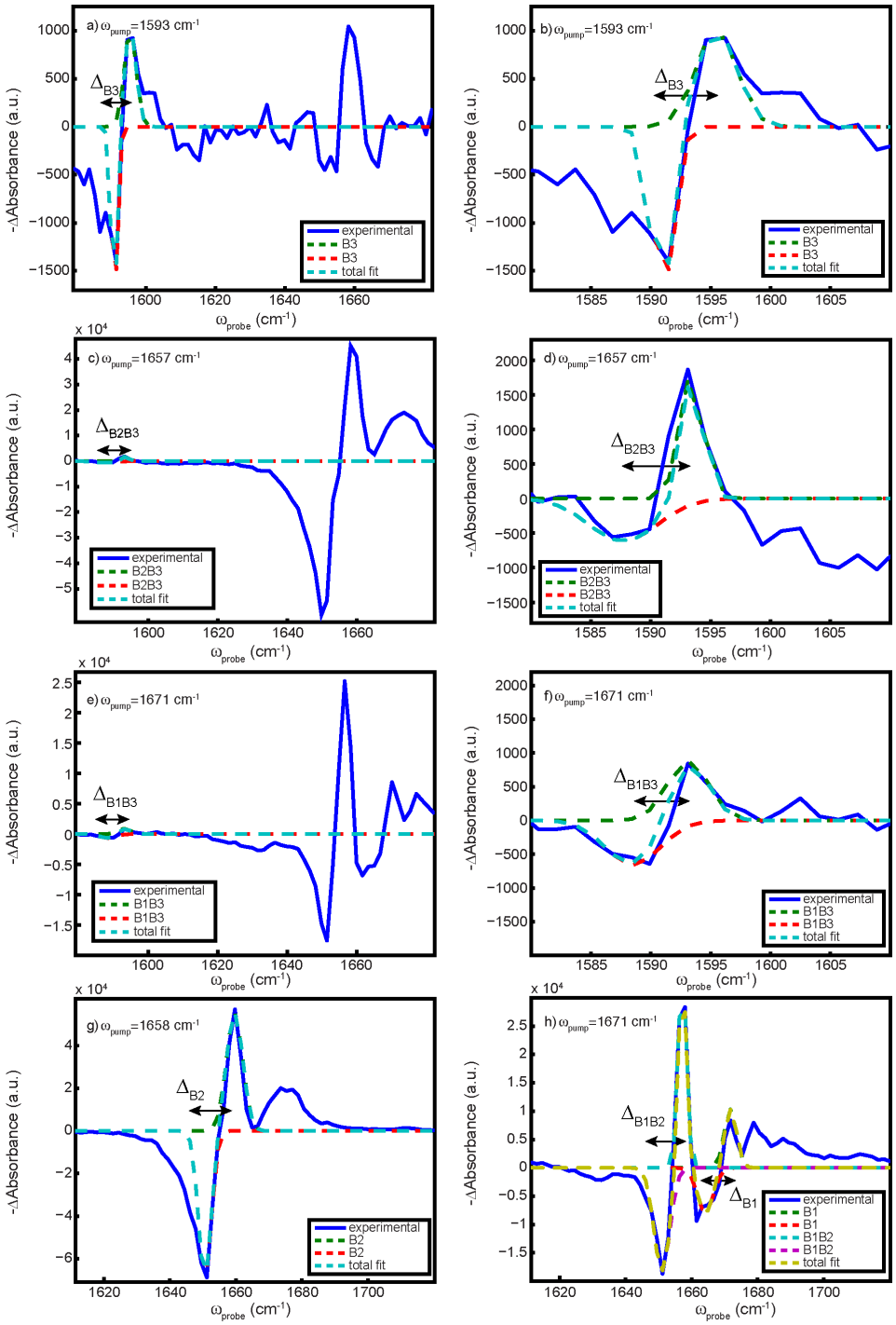

Figure S4.1. Benzoquinone slice were taken at a) and b) ω_{pump} = 1593 cm^{-1}, c) and d) ω_{pump} = 1657 cm^{-1}, e) and f) ω_{pump} = 1671 cm^{-1}, g) ω_{pump} = 1658 cm^{-1} and h) ω_{pump} = 1671 cm^{-1}. Figure S4.1b, S4.1d, and S4.1f) are zoomed in versions of S4.1a, S4.1c, and S4.1e, respectively. Figures S4.1a-f are slices from Figure 4.2a in the paper. Figure S4.1g-h are from Figure 4.3a in the paper. The slices along ω_{probe} were fit with Gaussian lineshapes and the fitting parameters were peak position, FWHM and dipole strength.

Table S4.1. Benzoquinone slices peak positions, FWHM and oscillator strengths.

Benzoquinone

ω_{pump} =1593	Peak position (cm^{-1})	FWHM (cm^{-1})	μ
(Figure S1a-b)	1595.5	4.00	0.36
	1590.9	2.27	-0.39
ω_{pump} =1657			
(Figure S1c-d)	1593.4	2.00	0.44
	1587.7	5.90	-0.34
ω_{pump} =1671			
(Figure S1e-f)	1593.1	3.50	0.36
	1588.5	5.00	-0.33
ω_{pump} =1658			
(Figure S1g)	1659.6	5.80	0.95
	1650.6	4.59	-1.00
ω_{pump} =1671			
(Figure S1h)	1671.8	3.90	0.65
	1664.2	5.15	-0.60
	1657.2	3.20	0.84
	1651.0	5.14	-0.74

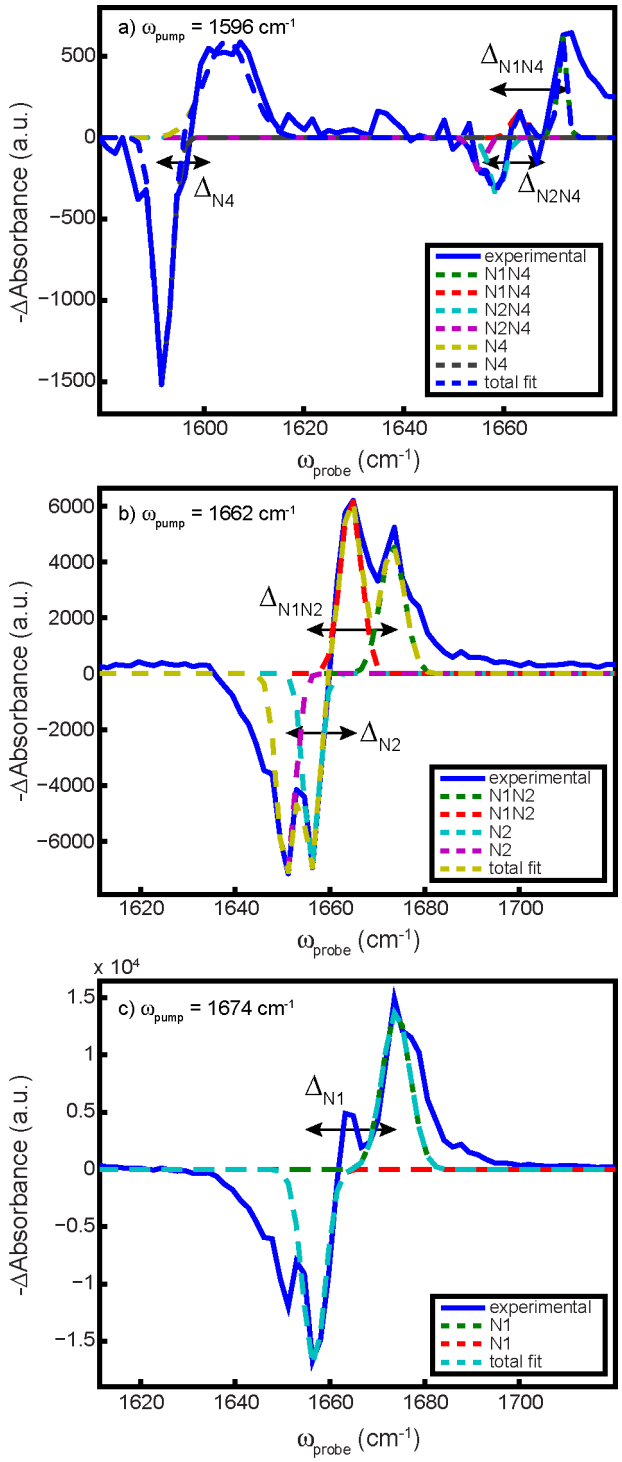

Figure S4.2. Naphthoquinone probe slices were taken at a) ω_{pump} = 1596 cm^{-1}, b) ω_{pump} = 1662 cm^{-1} and c) ω_{pump} = 1674 cm^{-1}. Figure S4.2a is a slice from Figure 4.2b in the paper. Figure S4.2b-c are slices from Figure 4.3b in the paper. The slices along ω_{pump} were fit with Gaussian lineshapes and the fitting parameters were peak position, FWHM and dipole strength.

Table S4.2. Naphthoquinone slices peak positions, FWHM and oscillator strengths.

Naphthoquinone

ω_{pump} = 1596	Peak position (cm^{-1})	FWHM (cm^{-1})	μ
(Figure S2a)	1671.6	1.90	0.50
	1663.2	3.00	0.38
	1658.7	4.10	-0.41
	1655.0	3.00	-0.38
	1604.6	10.07	0.48
	1591.7	5.10	-0.57
ω_{pump} = 1662			
(Figure S2b)	1673.2	6.00	0.72
	1664.4	5.15	0.78
	1656.1	3.90	0.80
	1650.7	4.40	0.81
ω_{pump} = 1674			
(Figure S2c)	1674.0	6.95	0.95
	1656.6	5.50	-1.00

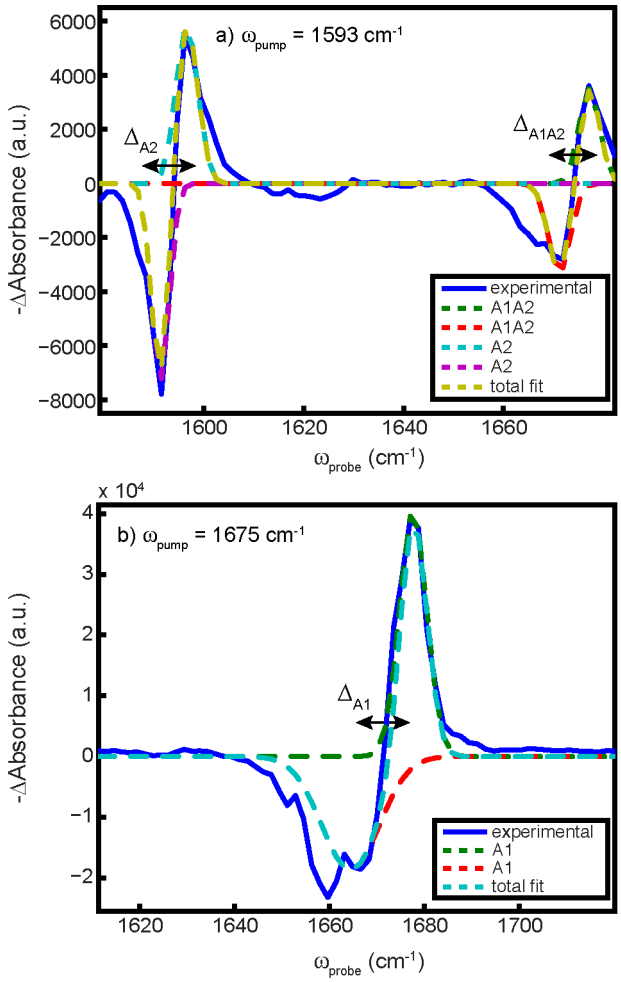

Figure S4.3. Anthraquinone probe slices were taken at ω_{pump} = 1593 cm^{-1} and ω_{pump} = 1675 cm^{-1}. Figure S4.3a is a slice from Figure 4.2c in the paper. Figure S4.3b is a slice from Figure 4.3b in the paper. The slices along ω_{pump} were fit with Gaussian lineshapes and the fitting parameters were peak position, FWHM and dipole strength.

Table S4.3. Anthraquinone slices peak positions, FWHM and oscillator strengths.

Anthraquinone

ω_{pump} = 1596	Peak position (cm^{-1})	FWHM (cm^{-1})	μ
	1677.2	4.85	0.56
	1671.2	5.17	-0.56
	1596.6	5.15	0.64
	1591.3	4.85	-0.68
ω_{pump} = 1675			
	1677.7	6.70	1.00
	1664.5	14.30	-0.82

Chapter 5

Probing Structural Features of Self-assembled Violanthrone-79 using Two Dimensional Infrared Spectroscopy

This chapter is a publication from 2015 and is published in the Journal of Chemical Physics.[1] This work focuses on probing the structure of a nanoaggregated PAH in solution using 2D IR spectroscopy.

5.1. Introduction

Polycyclic aromatic hydrocarbons (PAHs) are prevalent in synthetic materials and our natural environment. PAHs are a broad class of molecules that include molecular structures containing condensed homocyclic and heterocyclic aromatic rings. Non-covalent interactions such as π-π interactions between the aromatic cores are largely responsible for the self-assembled aggregate structures that can be formed. In addition, the aggregated structures can be altered depending on the solvent environment used during the self-assembly process. In materials science, PAHs have been widely used to develop light-harvesting arrays,[2,3] organic thin-film transistors,[4,5] liquid crystals,[6,7] laser dyes,[8,9] and organic solar cells.[10] The prevalence of PAHs in materials science applications such as these is in part due to the supramolecular structures that can be readily formed through solution based self-assembly processes. In these cases the nanoaggregate structures are sought after, but in other industrial applications, the PAH nanoaggregates are detrimental. The nanoaggregates that form from naturally occurring PAHs can be detrimental on the processing of petroleum resources.[11,12] For example, humic acids and asphaltenes are naturally occurring PAHs that form nanoaggregates through solution based self-

assembly. These nanoaggregates are known to create flow assurance problems in pipelines and generally produce an overall reduction in oil recovery.[13–15] The multitude of industrial applications influenced by the self-assembly of PAHs has driven the need to fully understand and characterize the self-assembly processes of PAHs.

Recently, several experimental and theoretical methods have been used to investigate the self-assembled structures of solar dye nanoaggregates including nanoaggregates of perylene tetracarboxylic diimide (PTCDI) derivatives and violanthrone derivatives.[16–18] These PAHs are relevant to industrial applications in light-harvesting arrays and asphaltene nanoaggregation. The PTCDI and violanthrone derivatives are recognized as good molecular models of asphaltenes because they have similar characteristics to natural asphaltenes and are thus referred to as "asphaltene-like" compounds. The asphaltene-like PAHs have physical attributes that are similar to asphaltenes: their molecular diffusion behaviors are similar, they have similarly sized PAH cores consisting of seven to ten fused aromatic rings that are pericondensed, and they have heteroatom contents similar to those found in natural asphaltenes.[19] Use of the asphaltene-like compounds are prevalent because it is convenient to modify their peripheral chains via synthetic routes and these compounds provide a route to exploring the consequences of the peripheral side chains being symmetrically versus asymmetrically distributed about the PAH core. In this work the investigation is focused on gaining insights on the nanoaggregate structures formed by the asphaltene-like molecule violanthrone-79 in chloroform.

The nanoaggregate structures of asphaltene-like molecules have been probed previously with proton nuclear magnetic resonance (H-NMR) spectroscopy,[18] scanning and transmission electron microscopy (SEM and TEM),[20,21] time-resolved fluorescence depolarization (TRFD) spectroscopy,[22] fluorescence correlation spectroscopy (FCS),[19,23] and molecular dynamics (MD)

simulations.[16,24] The SEM and TEM experiments were used to visualize the morphology of the nanoaggregates and to determine the spacing between individual molecules within a nanoaggregate. It was determined that the nanoaggregates can form one-dimensional rod-like structures where the spacing between monomer constituents ranged from 3.3 Å to 3.8 Å.[20,21] H-NMR spectroscopy, TRFD spectroscopy, and FCS experiments have been used to determine the critical nanoaggregate concentration (CNAC), molecular diffusion constants, and some structural parameters of the nanoaggregate in bulk solvent environments. The FCS and TRFD spectroscopy measurements are limited to investigations of the formation of dimers and trimers due to natural absorption and fluorescence characteristics of violanthrone derivatives. One investigation utilized H-NMR spectroscopy to probe the molecular arrangements in violanthrone nanoaggregates and confirmed the formation of H-type aggregate structures.[18] In addition to investigations regarding the static structures of nanoaggregates, the flocculation kinetics has been studied using confocal fluorescence and NMR imaging.[25] Despite the surge in experimental approaches used to measure structural parameters of PAH monomers and nanoaggregates, there continues to be a gap in the experimental literature describing the mechanisms for and kinetics of the nanoaggregation of PAHs. Molecular dynamics investigations have been able to approach these questions recently.

Recently, MD simulations have been performed to survey solute-solute and solute-solvent interactions that can drive PAH nanoaggregate formation.[16,17,24] PTCDI and violanthrone derivatives serve as model PAHs in many of these investigations. MD simulations can readily sample chemical space including effects of molecular structure on the nanoaggregate formation and the influence of solvent conditions on nanoaggregate formation. For example, the effect of the structure of the alkyl side chain on nanoaggregate microstructure has revealed the statistical

distributions of nanoaggregate size, persistence length, and confirmed the formation of H-type aggregate structures.[26] MD simulations have also revealed the modulation of nanoaggregate structures formed depending on the solvent conditions utilized. The MD simulations have provided some insights into the mechanistic details of PAH nanoaggregate formation, but the direct measurement of nanoaggregate formation remains elusive.

Asphaltenes and "asphaltene-like" compounds strongly absorb visible light and are naturally fluorescent. Thus, TRFD spectroscopy and FCS have been useful to investigate diffusion and rotational dynamics of asphaltene monomers and dimers, but the overwhelming signal makes it difficult to perform these measurements beyond dimerization. Moving into the mid-infrared region and using molecular vibrations to probe these molecules allows accessibility to a much broader range of asphaltene concentrations. Linear and non-linear infrared spectroscopies are ideally suited to investigate the role of π-stacking in the asphaltene nanoaggregation processes—these spectroscopies are intrinsically chemoselective and have high time resolution. In particular, 2D IR spectroscopy is especially useful in exploring these problems because we can access information regarding molecular structure,[27,28] dynamics,[29] and the surrounding molecular environment,[30,31] while maintaining flexibility with regard to the state of the sample.

The earliest works exploiting the structural sensitivity of 2D IR spectroscopy focused on describing structural dynamics in small peptides.[27] Later, 2D IR was extended to probing structural motifs of proteins in aqueous and lipid environments.[32,33] Significant efforts were made to adapt and apply vibrational coupling models to peptides and proteins that accounted for electrostatic interactions within the molecules. The models ranged in sophistication from the simplest electrostatic model, Transition Dipole Coupling (TDC),[34] to the most sophisticated model, Transition Dipole Density Distribution (TDDD),[35] and Transition Charge Models

(TCM),[36] providing a level of sophistication between TDC and TDDD. In addition, 2D IR spectroscopy was extended to probe DNA structural characteristics.[37–40] However, in order to develop 2D IR spectroscopy as a tool to monitor nucleic acid structures, the electrostatic models for vibrational coupling noted above had to be applied to DNA in order to develop new vibrational coupling models for nucleic acids—these efforts still continue today.[37,41] The work presented herein, describes a local mode basis derived from the normal modes of anthrone and violanthrone-79 that can be used to describe nanoaggregate structures formed by the asphaltene-like PAH, violanthrone-79. We present the site energies, vibrational coupling constants, and anharmonicities required for the local mode Hamiltonians describing anthrone and monomeric violanthrone-79. We use the monomer data and a simple electrostatic coupling model to describe nearest-neighbor interactions that exist in violanthrone-79 nanoaggregates. Three idealized structural models of the nanoaggregates are used to explore the dependence of the 2D IR spectral signatures on nanoaggregate structure. The 2D IR spectrum of each idealized nanoaggregate structure is calculated using no adjustable parameters and compared to the experimental 2D IR spectrum of violanthrone-79 nanoaggregates.

5.2. Methods

5.2.1. Visible Absorption Spectroscopy

Visible absorption spectroscopy experiments were completed at room temperature on a Nicolet Evolution 300 spectrophotometer (Thermo Electron Corporation). Samples of anthrone and violanthrone-79 in chloroform were prepared at various concentrations. Anthrone (>97%) was purchased from Santa Cruz Biotechnology, violanthrone-79 was purchased from Sigma Aldrich, and chloroform (ACS grade) was purchased from Fisher Scientific. Anthrone and

violanthrone-79 samples were placed between two CaF_2 windows with a Teflon spacer ranging from 25 micron to 100 micron thickness. The pathlength was divided by the absorbance to account for the different pathlengths used in the UV-vis experiments. The spectra are baseline corrected and normalized using MATLAB.

5.2.2. Linear IR Absorption and 2D IR Spectroscopy

Linear IR absorption spectra were collected on 10 mM anthrone, 0.5 mM violanthrone-79, and 10 mM violanthrone-79 in chloroform at room temperature using a Nicolet 6700 spectrometer (Thermo Fisher Scientific). Samples were prepared similar to UV-vis measurements except a 200 micron spacer was used for linear IR absorption and 2D IR measurements. Each linear IR absorption spectrum was collected with a spectral resolution of 4 cm^{-1} and was the result of averaging 64 scans. The atmospheric suppression correction within the Omnic software was applied to the spectra. Air background and a percentage of chloroform background were subtracted from each spectrum. All spectra were baseline corrected and fit with Gaussian lineshapes using MATLAB.

The 10 mM anthrone and violanthrone-79 samples were probed with 2D IR spectroscopy, where a third-order signal is emitted from the sample following excitation with three mid-IR electric fields. A description of the 2D IR spectrometer can be found elsewhere.[42] Briefly, the pulses are produced from a Ti:Sapphire oscillator operating at 75 MHz, which seeds a regenerative amplifier (Wyvern 1000, KM Labs) to produce sub-45 fs pulses that are centered at 800nm. The regenerative amplifier produces pulses at a 1 kHz repetition rate. The output pulses are used to pump an optical parametric amplifier (OPA, Light Conversion TOPAS-C) with a difference frequency generation stage ($AgGaS_2$) in order to generate mid-IR pulses centered at 6000 nm; the mid-IR pulses are 70 fs in duration with 9 μJ of energy. The mid-IR light is split

into a pump and a probe line in which 90% of the mid-IR is in the pump beam and 10% is in the probe beam. The pump beam is directed to a Ge-acoustic optic modulator (Ge-AOM, Isomet Corporation LS600-1109) based pulse shaper for direct pulse-shaping in the mid-IR.[43,44] The pulse shaper set up has a 4-*f* geometry and the mid-IR light is first directed onto a grating with a groove density of 100 grooves/mm. The diffracted beams reflect off a cylindrical mirror (129.4 mm f.l.) and a 3-inch gold mirror directs the beam onto the Ge-AOM at the Bragg angle. The beam is directed to identical optics in the second half of the pulse shaper. An arbitrary waveform generator (AWG, DynamicSignals LLC PXDAC4800) in conjunction with a RF amplifier produces the acoustic wave required for pulse shaping. Active Bragg angle compensation was utilized.[45] The output pulses from the pulse shaper are 134 fs in duration as measured by autocorrelation. A pump-probe beam geometry is used, and the self-heterodyned third order signal is detected on a linear 64-element mercury cadmium telluride (MCT) array detector. The pulse delay is scanned from 0 to 2500 fs in 7 fs steps with the pulse shaper. Contributions to the signal from transient absorption and background scatter are removed with phase cycling.[46] Additional noise is minimized by averaging 300 scans. The grating utilized in the 2D IR spectrometer had a groove density of 75 grooves/mm; based on the grating chosen and the configuration of the monochromator a spectral resolution of 1.7 cm^{-1} was achieved. The polarization is set to parallel for the three mid-IR electric fields and the emitted third order electric field. The absorptive 2D IR spectra are observed under the above experimental conditions.

5.2.3. Computational Methods

Electronic structure calculations were completed to obtain relative dipole angles and transition dipole vectors. Density functional theory (DFT) with the Becke-3-Lee-Yang-Parr

(B3LYP) exchange-correlation functional is used for geometry optimizations and frequency calculations. All calculations were completed in Gaussian 09[47] with a 6-31G(d) basis set. The violanthrone-79 calculation was completed on a truncated violanthrone-79 molecule with ethyl groups instead of the longer aliphatic side chains. The geometry optimization does not change significantly, and the smaller side groups decreases the computational time required for the calculation. The calculations are completed to obtain the dipole vectors for the modes between 1560 to 1680 cm^{-1}. The dipole vectors are used as inputs to simulate 2D IR spectra of aggregated violanthrone-79.

5.2.4. Simulated Linear Absorption and 2D IR Spectra

Parameters, including eigenenergies, dipole strengths and anharmonicities, from linear IR absorption spectra, 2D IR spectra and frequency calculations are used as inputs to calculate linear IR absorption and 2D IR spectra. The parameters obtained from the experimental data and theoretical calculations are held constant and not allowed to vary. The linear IR absorption spectra are calculated using a linear response function and the 2D IR spectra are calculated using a third order nonlinear response function. The vibrational states in the calculations have a maximum quantum number of 2. The vibrational states consist of combination bands, overtones, and fundamental states. The calculations use a pure dephasing time of 1.0 picosecond.

5.3. Results and Discussion

5.3.1. Nanoaggregation Concentration

It is known that the molecular order in self-assembled PAHs is partially driven by the dynamics of solvent molecules surrounding the PAHs. For example, molecular dynamics

simulations of solar dyes in water and toluene reveal different propensities for various self-assembled structures. PAH nanostructures formed in water tend to resemble three-dimensional spheres due to the PAHs simply being entangled rather than forming nanostructures with higher degrees of ordering.[24] In contrast, nanostructures formed by PAHs in toluene exhibit greater ordering where the three-dimensional structures resembled short cylinders made of fewer than 11 PAH monomers with their cores stacked on top of each other.[24] Moreover, self-assembled structures of PAHs in thin films exhibit structures that result in J-aggregate type configurations.[18] The goal of this chapter is to provide insights to the structure of self-assembled nanoaggregates of violanthrone-79 in bulk chloroform.

In order to approximate the molecular organization within nanoaggregates formed by violanthrone-79 in chloroform, we examine the visible absorption spectrum as a function of violanthrone-79 concentration. The maximum concentration for monomer violanthrone-79 in chloroform was determined to be 1.0 mM using visible absorption spectroscopy. The normalized visible absorption spectra of violanthrone-79 in chloroform are shown in Figure 5.1a. The spectral region from 450 to 800 nm has one absorption peak for violanthrone-79 in chloroform. The spectrum for 1 mM violanthrone-79 in chloroform is of monomer form. As the concentration of violanthrone-79 is increased from 0.1 mM to 20 mM, there is a blue-shifted maximum absorption, indicative of H-type aggregates. The absorbance intensity of the new feature at 620 nm is plotted as a function of violanthrone-79 concentration in Figure 5.1b. The spectra were normalized to the 652 nm peak. The nonlinearity suggests a significant change in molar absorptivity. As concentration is increased, there is an increase in absorption at 620 nm. In comparison, studies have been completed to understand the stacking of violanthrone derivatives formed in thin films prepared by spin coating.[18] The visible absorption spectra of

violanthrone in thin films exhibits differences in peak shifts; the difference in the peak shifts indicates a J-aggregate type structure in thin films. We focus on the H-type aggregate structures in this work.

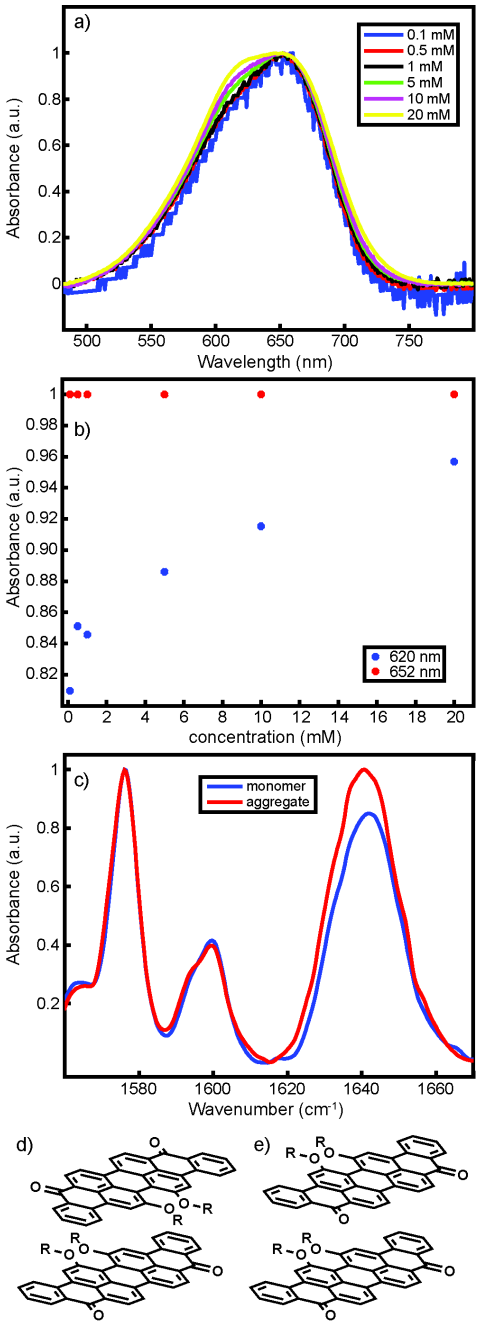

Figure 5.1a-e. a) Visible absorption spectra of violanthrone-79 in chloroform with concentrations ranging from 0.1 mM to 20 mM. The blue shift is indicative of H-type aggregation. b) Plot of the absorbance in arbitrary units versus concentration of the peaks at 620 nm (blue) and 652 nm (red) from the visible absorption spectra. c) Linear IR absorption spectra of 0.5 mM and 10 mM violanthrone-79 in chloroform. The structures in d) and e) are possible aggregated structures based on the H-type aggregate response exhibited in the visible absorption data.

Based on the visible absorption data, violanthrone-79 forms an H-aggregate type structure in chloroform as expected from previous results in the literature.[18] However, the visible absorption results are insufficient for determining the relative position of each constituent violanthrone-79 molecule with respect to each other in the nanoaggregates. For instance, the visible absorption data is not sufficient to determine the difference between the structures in Figure 5.1d and Figure 5.1e. Therefore, other forms of spectroscopy, including linear IR absorption and 2D IR absorption, are necessary in order to discriminate between the possible structures of self-assembled violanthrone-79 aggregates in bulk solutions.

The linear IR absorption spectra of monomeric and aggregated violanthrone-79 in chloroform are shown in Figure 5.1c. There are differences in the high frequency peak intensity between the monomer and aggregated spectra. On the one hand, the linear IR absorption spectra are not sufficient to uniquely describe the structure of aggregated violanthrone-79 because there are not enough observables. On the other hand, the linear IR absorption does provide insight into which vibrational modes are coupled in the aggregate form; only changes in the high frequency peak dominated by in-plane carbonyl stretching are observed. In reality, given the molecular size of violanthrone-79 and the extensive ring system, there are many atoms that can contribute to the collective vibrational motions observed in the normal modes of the molecule. Hence to gain further insight into the vibrational coupling between the carbonyl stretching motions and the in-plane stretching motions of the ring system, we examine the smaller molecule anthrone.

5.3.2. Anthrone

In order to build a local mode picture of the vibrational motion in violanthrone-79 that has the potential to be a model more broadly utilized we must gain an understanding of the vibrational interactions between the carbonyl stretching motion and the in-plane ring stretching

motions in these molecules. The molecular structure of anthrone is shown in Figure 5.2b. Anthrone is a ketone with the extended ring system of anthracene. It is possible that the vibrational interactions between the carbonyl and ring system in anthrone are analogous to those in violanthrone-79. Here we present the linear IR absorption spectrum, the 2D IR spectrum, and electronic structure calculations of anthrone. We use the results of the electronic structure calculations in conjunction with the spectroscopy results to determine the site energies, vibrational coupling, diagonal anharmonicities, the off-diagonal anharmonicities, and the relative orientations of the transition dipoles required to compute the linear IR absorption spectrum and 2D IR spectrum of anthrone.

The linear IR absorption spectrum presented in Figure 5.2a was collected on 10 mM anthrone in chloroform; the normalized spectrum is plotted in Figure 5.2a. The peaks in the spectral region from 1560 to 1720 cm^{-1} originate from in-plane stretching vibrational modes that are dominated by ring and carbonyl motions. The spectrum in Figure 5.2a is of monomeric anthrone. In order to describe the anthrone spectrum, we assume a single vibrational mode related to the carbonyl stretching motion and two normal modes related to the antisymmetric and symmetric stretching of the ring system; these three vibrational modes are labeled A1, A2, and A3, respectively. The experimental spectrum is fit with Gaussian lineshapes resulting in linewidths of 15.8 cm^{-1} for A1, and 12.1 cm^{-1} for each A2 and A3. The center peak positions are 1661.1 cm^{-1}, 1603.5 cm^{-1}, and 1602.5 cm^{-1} for A1, A2, and A3, respectively, and correspond to the normal mode eigenenergies of anthrone. The theoretical spectrum generated from the electronic structure frequency calculations is illustrated in Figure 5.2b. The stick spectrum is produced from the calculated eigenenergies and intensities; Gaussian lineshapes with linewidths equal to the experimental linewidths given above are used to convolute over the stick spectrum.

A scaling factor of 0.9614 for the B3LYP/6-31G frequency calculations was applied to the frequencies.[48] The results of the electronic structure calculations are used to gain insights to the nuclear motions involved with each vibrational mode.

Based on the electronic structure frequency calculations, the three vibrational modes considered for modeling anthrone, A1, A2, and A3, are dominated by in-plane stretching motions of the carbonyl bond and in-plane stretching motions of the carbon atoms in the ring system. The stretching of the carbon and oxygen atom that compose the carbonyl functional group contribute 90.5% of the displacement to the vibrational mode A1. The ring breathing from the carbon-carbon double bonds contribute 8.9% of the displacement to the vibrational mode A1. The percentage of displacement is calculated using the high precision displacements given for a specific vibrational mode calculated in the frequency calculations performed and then the magnitude of displacement is calculated for each atom. The carbonyl displacement was calculated by the summation of the carbon and oxygen displacements, whereas the ring breathing displacements were calculated by the summation of the carbon displacements in the rings, excluding the carbon that is part of the carbonyl functional group. Thus, the vibrational mode A1 is mostly composed of the carbonyl motion. The displacements of the atoms were also determined for vibrational modes A2 and A3. Mode A2 is 89.6% ring breathing and 0.6% carbonyl stretching. Mode A3 is 85.5% ring breathing and 4.8% carbonyl stretching. Therefore, the two low frequency modes correspond to ring breathing. More specifically, A2 is the antisymmetric ring breathing mode, and A3 is the symmetric ring breathing mode. The angle between the two ring breathing transition dipoles is equal to 91.1 degrees. The transition dipole for the carbonyl stretch mode A1 is found to lie along the carbonyl bond.

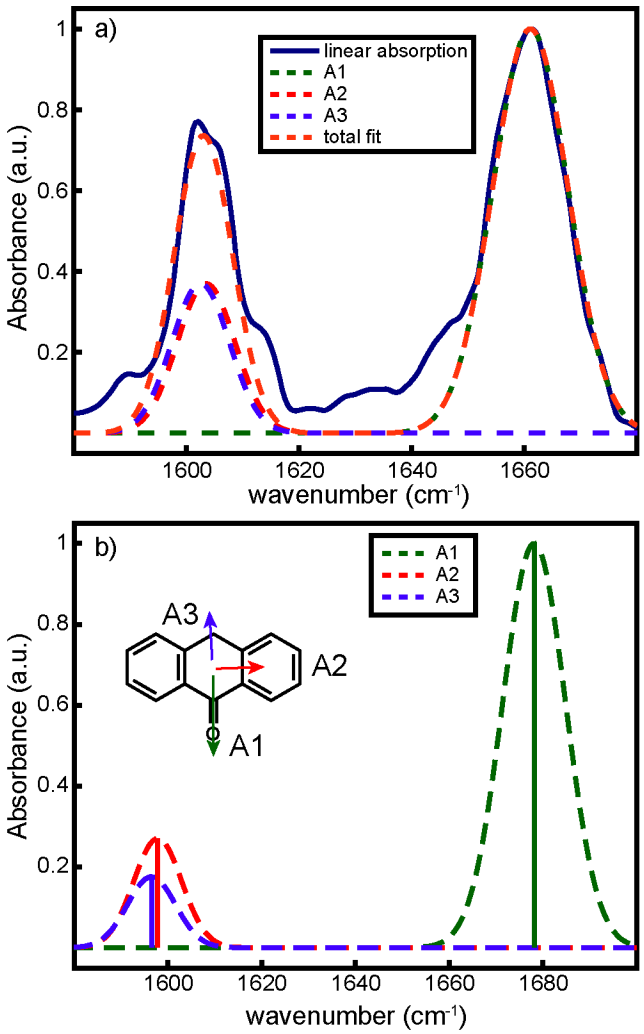

Figure 5.2a-b. Linear absorption spectra of a) experimental anthrone in chloroform and b) electronic structure frequency calculation of anthrone. The resulting site energies and intensities were convoluted with a Gaussian lineshape to produce the spectrum. The transition dipole vectors projected on the anthrone structure were obtained from the frequency calculations. The dipoles, depicted on the molecule, are scaled based on the transition dipole strength from the fits from the experimental linear absorption spectrum.

2D IR experiments were completed on anthrone in chloroform; the experimental spectrum is illustrated in Figure 5.3a. Figure 5.3b illustrates the calculated linear IR absorption and 2D IR spectra. The 2D IR spectra include peak pairs along the diagonal and off of the diagonal as illustrated in Figure 5.3a-b. Each peak pair contains a negative-going peak (blue) for the bleach and a positive-going peak (red) for the stimulated emission. The peak pairs observed along the diagonal are separated along ω_{probe} by the anharmonicity, Δ_i, of the vibrational mode. The off-diagonal peak pairs, or cross peaks, are separated along ω_{probe} by the off-diagonal anharmonicity, Δ_{ij}, of the vibrational mode. In order to extract the diagonal and off-diagonal anharmonicities, slices are taken along ω_{probe} and the peaks are fitted to Gaussian lineshapes. The separation between the negative-going and positive-going peak in the peak pair is the anharmonicity. The anharmonicities were subsequently utilized to calculate the observed 2D IR spectra. The diagonal anharmonicity for the carbonyl mode is 10 cm^{-1}, and the off-diagonal anharmonicity is 5 cm^{-1}. The magnitudes of these anharmonicities are similar to those observed recently in a quinone series.[42]

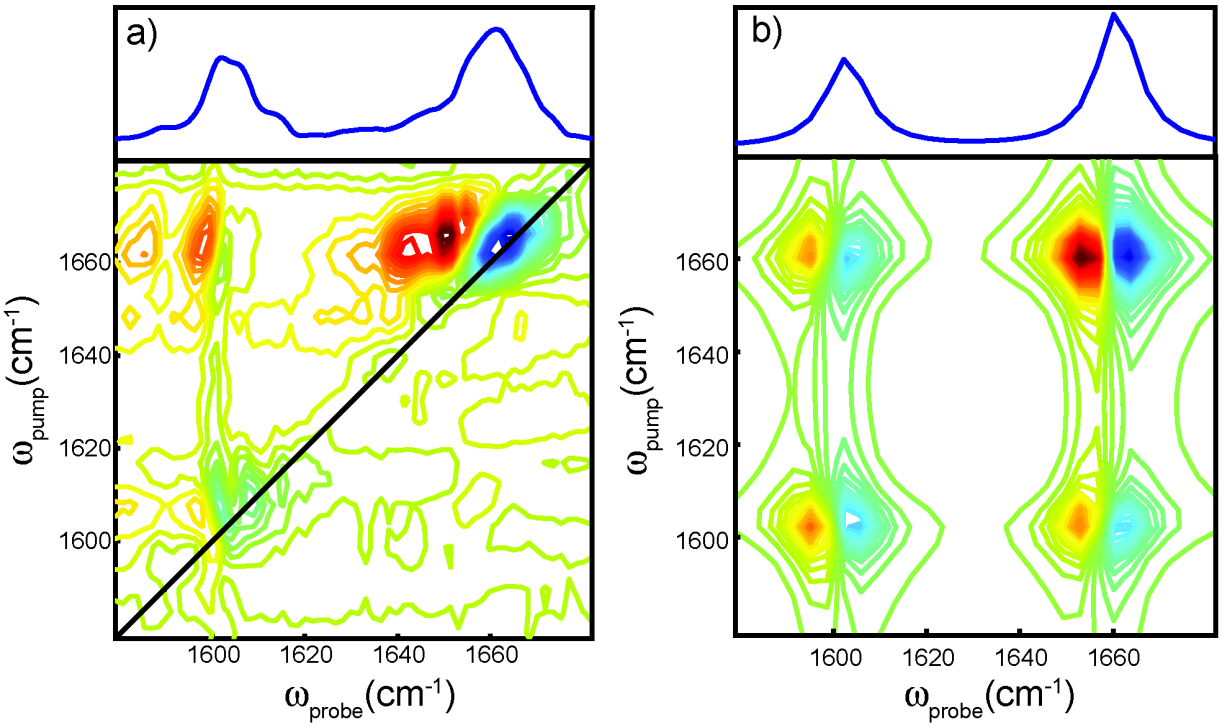

Figure 5.3a-b. Linear IR absorption and 2D IR spectra of a) experimental spectra of anthrone in chloroform and b) calculated spectra of anthrone.

Figure 5.3a also contains cross peaks, which are well defined in the top left corner of the spectrum. The cross peaks are indicative of vibrational coupling, β, between the high and low frequency modes. The time between pulse 2 and 3, known as T_w, was held at zero. Therefore, the cross peaks originate from vibrational coupling and not from a chemical exchange or energy transfers process. The magnitude of β is determined by inverting the 1Q Hamiltonian. The local mode site energies used were 1655 cm^{-1} for the high frequency mode, A1, and 1606 cm^{-1} for the degenerate low frequency modes, A2 and A3. The vibrational couplings are equal to -12.5 cm^{-1} between A1 and A2, 12.5 cm^{-1} between A1 and A3, and -2.5 cm^{-1} between A2 and A3. The local mode site energies, the vibrational coupling constants, and the anharmonicities are each parameters given by the observed spectra and are used to calculate the 2D IR spectrum of

anthrone. The normal mode energies, local mode energies, and vibrational couplings between the vibrational modes can be found in Table 5.1.

The calculated linear IR absorption and 2D IR spectra are illustrated in Figure 5.3b. The dipole derivative unit vectors are obtained from the electronic structure frequency calculations. The relative transition dipole strengths are determined from the linear IR absorption spectrum. Thus, there are no variable parameters in this calculation. The calculated spectra in Figure 5.3b reproduce the experimental spectra in Figure 5.3a well. One issue between the calculated and experimental is the lower right off diagonal peaks. The asymmetry in the 2D IR spectra can arise from several factors including destructive interference between the molecular responses probed, phase twist between the pulses at different frequencies, and the differences in oscillator strengths between the μ_{12} states probed. Of these situations, phase twist between pulses is not taken into account in the calculated 2D IR spectra and the μ_{12} oscillator strengths are written in terms of the μ_{01} oscillator strength. The above is true for all calculated 2D IR spectra presented in this chapter. The parameters used to calculate the linear IR absorption and 2D IR spectra of anthrone are used as the local mode basis for monomer and aggregated violanthrone-79 below.

5.3.3. Monomer Violanthrone-79

It is critical to understand the vibrational interactions involved in a violanthrone-79 molecule prior to developing a model to examine the nanoaggregate structures. If the normal modes observed for monomeric violanthrone-79 can be related to vibrational motions localized on specific bonds in the molecule, then it is possible to use 2D IR spectroscopy as a tool to determine the relative orientations of monomer units in the nanoaggregate structures of violanthrone-79. For example, the carbonyl bonds located on the violanthrone-79 ring system can potentially be very nice handles to extract structural information related to the nanoaggregate

structures. This requires the ability to transform the normal modes describing the symmetric and antisymmetric stretching vibrations of these carbonyl bonds into a new basis in which these vibrational modes are localized on these carbonyl bonds. To this end, we present the linear IR absorption spectrum and electronic structure calculations necessary to complete the transformation from a normal mode basis to a local mode basis useful for structure determination.

There are five vibrational modes that dominate the linear IR absorption spectrum of monomeric violanthrone-79. The linear IR absorption spectrum and the molecular structure with the five transition dipole vectors considered is shown in Figure 5.4a. Violanthrone-79 has three vibrational modes that are analogous to anthrone; the modes labeled V1, V3, and V4 are analogous to the anthrone vibrational modes labeled A1, A2, and A3, respectively. Violanthrone-79 has an additional carbonyl vibrational mode labeled V2 and a low frequency mode centered at 1576 cm^{-1} labeled V5. The modes V1 and V2 are the symmetric and antisymmetric carbonyl stretching modes and are centered at 1645.6 cm^{-1} and 1637.1 cm^{-1}, respectively. The modes V3 and V4 are in-plane ring breathing motions and have center frequencies equal to 1600 cm^{-1} and 1598 cm^{-1} for V3 and V4, respectively. The vibrational motions for V5 are composed of in-plane stretching motions involving atoms that comprise the inner core rings of violanthrone-79; the center frequency of V5 is equal to 1576 cm^{-1}.

Electronic structure frequency calculations were performed on violanthrone-79 where the alkyl chains were truncated to be ethyl groups. The results of these calculations yield the atomic displacements that are involved in each vibrational mode of interest and the corresponding transition dipole vectors. The displacements of the carbon and oxygen atoms that compose the carbonyl functional group contribute 86.6% and 85.1% of the displacements to vibrational modes

V1 and V2, respectively. The ring breathing displacements analogous to anthrone contribute 12.0% and 13.2% of the displacements to the vibrational modes V1 and V2. The middle core rings contribute 1.4% and 1.7% to V1 and V2. The ring breathing displacement was calculated by the summation of the carbons in the three rings closest to the carbonyl, excluding the carbon that is part of the carbonyl functional group. The middle core ring breathing displacement is calculated by the summation of the five center ring carbons. The vibrational modes V3 and V4 are composed of 85.6% and 75.8% of the ring breathing vibrational motion, respectively. In modes V3 and V4, the carbonyl displacements contribute modestly to the total displacements: the carbonyl displacements are 4.0% and 2.5% for modes V3 and V4. In mode V3, the contribution of the middle core ring displacement is also minimal at 1.7%. In contrast, the V4 mode involves carbon atoms in the entire ring system of the molecule resulting in 97.5% of the total displacements coming from carbons in the entire ring system. The remaining 8.8% and 2.5% displacements for the V3 and V4 vibrational modes, respectively, are from the atoms from the aliphatic chains and ester functional group. The displacements in mode V5 are dominated by the middle core ring displacements. The middle core ring displacements contribute to 87.1% of the motion, and the carbonyl displacements and ring breathing displacements contribute 5.5% and 7.4% respectively. These results indicate mixing of the carbonyl motion in violanthrone-79 is similar to that of anthrone.

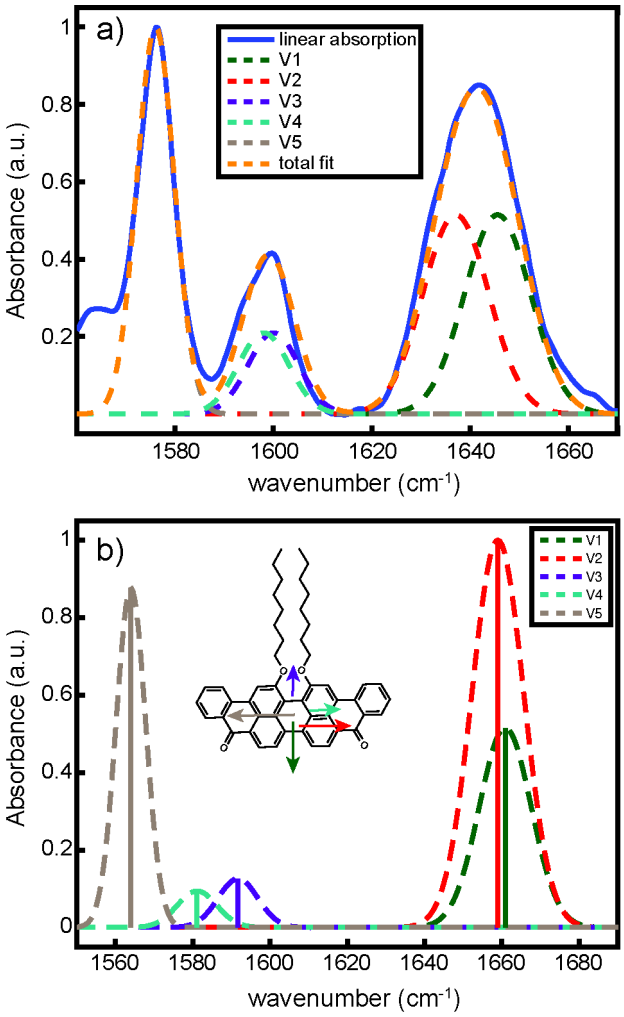

Figure 5.4a-b. Linear absorption spectra of a) experimental violanthrone-79 in chloroform and b) electronic structure frequency calculation of violanthrone-79. The resulting site energies and intensities were convoluted with a Gaussian lineshape to produce the spectrum. The transition dipole vectors projected on the violanthrone-79 structure were obtained from the frequency calculations. The dipoles, depicted on the molecule, are scaled based on the transition dipole strength from the fits from the experimental linear absorption spectrum.

The 1Q Hamiltonian was also inverted for monomeric violanthrone-79 in order to extract the local mode energies and intramolecular vibrational couplings necessary to describe the vibrational characteristics of the molecule. The 1Q Hamiltonian for monomeric violanthrone-79 written in a local mode basis is given in Equation 5.1,

$$H = \sum_i E_i^C \left|C_i\right\rangle\left\langle C_i\right| + \sum_i E_i^R \left|R_i\right\rangle\left\langle R_i\right| + \sum_i E_i^M \left|M_i\right\rangle\left\langle M_i\right| + \sum_{i<j} \beta_{ij}^C \left|C_i\right\rangle\left\langle C_j\right| + \ldots$$
$$\sum_{i<j} \beta_{ij}^R \left|R_i\right\rangle\left\langle R_j\right| + \sum_{i,j} \beta_{ij}^{CR} \left(\left|C_i\right\rangle\left\langle R_j\right| + \left|R_j\right\rangle\left\langle C_i\right|\right) + \sum_{i,j} \beta_{ij}^{RM} \left(\left|R_i\right\rangle\left\langle M_j\right| + \left|M_j\right\rangle\left\langle R_i\right|\right) \qquad \text{Equation 5.1}$$

where E^C, E^R, and E^M are the site energies for the carbonyl stretching, ring breathing, and middle ring breathing vibrational modes, and β^C, β^R, β^{CR}, and β^{RM} are intramolecular vibrational couplings. Given the vibrational motions that exist in violanthrone-79 that are analogous to the vibrational motions in anthrone, we use the parameters obtained from the analysis of the anthrone spectra as a starting point to model monomeric violanthrone-79. Thus, the vibrational coupling constants and site energies used for anthrone were also used for violanthrone-79 with one caveat. The caveat is in regard to the local mode site energy used for the high frequency peak observed at 1655 cm^{-1}. This peak is observed 20 cm^{-1} lower in violanthrone-79 than in anthrone in both the linear IR absorption spectra and the electronic structure frequency calculations. Therefore, the site energy used for the degenerate carbonyl stretch local modes in violanthrone-79 is shifted 23 cm^{-1} lower than the site energy corresponding to the carbonyl stretch in anthrone. As such, we set E_i^C equal to 1632 cm^{-1}. The coupling parameters from inverting the Hamiltonian are -4.5 cm^{-1} for β^C, 12.5 cm^{-1} for β^{CR} and -5.7 cm^{-1} for β^{RM}. This model of monomeric violanthrone-79 assumes there is no vibrational coupling between the carbonyl and middle ring vibrational modes, β^{CM}. These parameters

utilized as inputs to the 1Q Hamiltonian reproduced the experimental linear IR spectrum of monomer violanthrone-79 quantitatively are listed in Table 5.1. Furthermore, these parameters are input to the 1Q and 2Q Hamiltonians required to describe violanthrone-79 nanoaggregates; these input parameters are held fixed in the calculated spectra presented below.

Table 5.1. Parameters from linear IR absorption spectra and electronic structure frequency calculations of anthrone and monomer violanthrone-79.

	normal mode energy (cm^{-1})	local mode energy (cm^{-1})	β (cm^{-1})
anthrone			
A1	1661.0 ± 1.0	1655.0 ± 1.6	
A2	1603.5 ± 1.4	1606.0 ± 1.8	
A3	1602.5 ± 2.1	1606.0 ± 1.8	
A1A2			-12.5 ± 1.4
A1A3			12.5 ± 1.4
A2A3			-2.5 ± 1.8
violanthrone-79			
V1	1645.6 ± 1.4	1632.0 ± 2.3	
V2	1637.1 ± 1.6	1632.0 ± 2.3	
V3	1600.0 ± 1.5	1606.0 ± 2.4	
V4	1598.0 ± 1.0	1606.0 ± 2.4	
V5	1576.0 ± 0.9	1579.0 ± 1.5	
V1V2			-4.5 ± 1.1
V1V3			-12.5 ± 0.4
V1V4			12.5 ± 0.4
V1V5			0
V2V3			12.5 ± 0.4
V2V4			12.5 ± 0.4
V2V5			0
V3V4			-2.5 ± 1.0
V3V5			-5.7 ± 0.7
V4V5			-5.7 ± 0.7

5.3.4. Aggregated Violanthrone-79

The ultimate goal of this work is to develop an approach to model PAH nanoaggregate structures, thus expanding 2D IR spectroscopy as a tool for probing self-assembled structures of PAHs in general. In sections 5.3.1 and 5.3.2, we developed models of anthrone and monomeric violanthrone-79 in a localized basis by inverting the 1Q Hamiltonians required for each molecule and subsequently transforming the normal mode transition dipoles into a local mode transition dipole basis.[49] In this section, we use the parameters developed in sections 5.3.2 and 5.3.3 to account for the intramolecular vibrational interactions for violanthrone-79 molecules within a nanoaggregate. In order to account for vibrational interactions between violanthrone-79 sites in a nanoaggregate we utilize a simple electrostatic coupling model, TDC, to provide the vibrational couplings present in the nanoaggregate to a first approximation. A true test of the modeling presented here is whether we can distinguish the possible relative orientations of violanthrone-79 monomer units in nanoaggregate structures.

The linear IR absorption and 2D IR spectra of aggregated violanthrone-79 in chloroform are illustrated in Figure 5.5. The structure of violanthrone-79 with local transition dipole vectors is also depicted in Figure 5.5. The local modes are calculated by transforming the normal modes from the monomer according to the eigenvectors required to invert the 1Q Hamiltonian. The two carbonyl stretch local modes labeled A and B are rotated 20 degrees off of the carbonyl functional groups. The projection of local mode B onto A results in an angle of 166 degrees. The angle between the carbonyl functional groups is 122 degrees. Therefore, each carbonyl transition dipole must lie 22 degrees off of the carbonyl functional group according to the projection of local mode B onto A. The ring modes labeled C, D, and E are rotated 10.7 degrees, 11.0 degrees, and 20.0 degrees from carbonyl A, respectively. The transition dipoles

associated with the ring modes are placed at the center of mass of the violanthrone-79 monomer. These five local transition dipoles are set into several idealized nanoaggregate structures below. Furthermore, these local mode transition dipoles are used to calculate nearest neighbor vibrational couplings in the nanoaggregate structures.

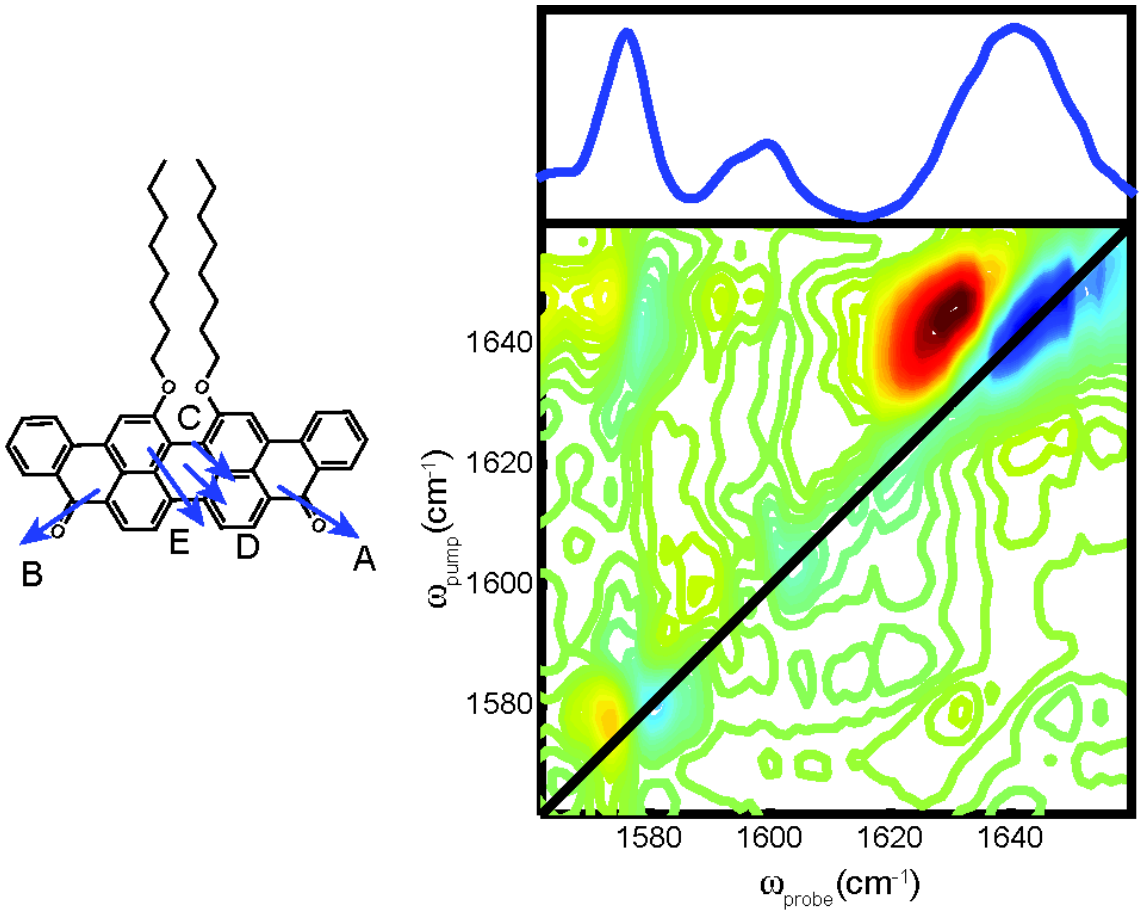

Figure 5.5. Linear IR absorption and 2D IR spectra of experimental violanthrone-79 in chloroform and structure of violanthrone-79 with local mode transition dipoles.

The spectra of the aggregated violanthrone-79 were calculated using three molecules. Asphaltenes and model asphaltenes, including violanthrone-79, have reported stacking distances ranging from 3.4 - 4.5 Å apart, a distance determined with molecular dynamics simulations,[16]

NMR,[25] HRTEM,[20] and SEM[21] experiments. In the nanoaggregate models used in this study, the violanthrone-79 molecules are stacked 4.5 Å apart in order to use comparable geometries to those observed in molecular dynamics simulations of violanthrone-78; violanthrone-78 and violanthrone-79 only differ in the length of their alkyl chains. The coupling parameters and site energies from the monomeric violanthrone-79 were used for each individual molecule within the nanoaggregate and held fixed. A pure dephasing time of 1.0 picosecond is used in the calculated spectra. The spectra were calculated for a parallel-stacked aggregate, an anti-parallel-stacked aggregate with molecules rotated 180 degrees relative to each other, and an aggregate stacked with the molecules rotated 28 degrees relative to each other producing a chiral geometry. In addition, angular disorder was examined by calculating spectra using the parallel and anti-parallel nanoaggregate structures wherein the center molecule was rotated ±28 degrees from parallel or antiparallel. The angle utilized to examine angular disorder was chosen based on the angular distribution observed in MD simulations of violanthrone-78 under similar solvent conditions.[24] All calculated linear IR absorption and 2D IR spectra used for examining angular disorder can be found in the supplemental information.[50] Nearest neighbor vibrational couplings were calculated between the molecules in each stacked configuration using transition dipole coupling model.

The simplest vibrational coupling model to describe the electrostatic interactions between two dipoles is transition dipole coupling (TDC) and is given by Equation 5.2.[34] TDC works well for molecules that are not covalently bonded, have reasonable separations, and have no electrodynamic contributions to the vibrational coupling.

$$\beta_{ij} = \frac{1}{4\pi\epsilon_0} \frac{|\mu_i||\mu_j|-3(\mu_i \cdot \hat{n})(\mu_j \cdot \hat{n})}{R_{ij}^3}$$

Equation 5.2

where μ_i and μ_j are the magnitudes of the vibrational transition dipoles in the local mode basis, $\hat{n}$ is the unit vector pointing in the direction of the transition dipoles, and R_{ij} is the distance between the vibrational transition dipoles in the molecular frame. Below, TDC is used to calculate the vibrational coupling between nearest neighbor units in the nanoaggregate structures.

The calculated 1D- and 2D IR spectra for the parallel configuration is illustrated in Figure 5.6a-b. The coupling constants are the largest between carbonyl modes that are stacked directly on top of each other, ranging from 23.6 to 31.7 cm^{-1}. The coupling between the carbonyl modes and the middle core rings of another molecule ranges from -2.1 to -6.5 cm^{-1}. The coupling constants for the carbonyl and the ring breathing modes are smaller in magnitude and range from -2.0 to -12.3 cm^{-1}. The coupling between two middle core rings is 44.4 cm^{-1}. The vibrational coupling constants describing the carbonyl-carbonyl interactions and the interactions between nearest neighbor middle core are strikingly large. On the one hand, it is possible that TDC produces coupling constants that are largely overestimated. On the other hand, it is possible that using a multipole expansion of an electrostatic potential would result in magnitudes of coupling constants that are not overestimated. However, even if the largest coupling constants calculated for this model are reduced by one half using a multipole expansion, the splitting between the eigenenergies would still be too large to be in agreement with the experimental spectrum. In addition, it is not clear that the relative intensities of the eigenstates would be dramatically improved. Moreover, the TDC results for the idealized anti-parallel model have reasonable magnitudes. Thus, the magnitudes of these coupling constants are not simply a product of utilizing an electrostatic coupling model that is not expanded to higher order multipole terms.

The simulated spectra for the anti-parallel configuration are found in Figure 5.6c-d. The coupling constant between the carbonyl modes of molecule 1 and molecule 2 range from -0.3 to -

6.0 cm^{-1}. The coupling constants for the carbonyls for the anti-parallel configuration are an order of magnitude smaller than the parallel configuration. The coupling constants between the carbonyl and the middle core ring range from 0.3 to 6.7 cm^{-1}. Similar to the parallel configuration, the ring breathing and carbonyl modes have coupling constants ranging from 0.1 to 3.1 cm^{-1}. The middle core ring coupling between molecule 1 and 2 is 7 cm^{-1}. The coupling between molecule 2 and 3 is the same as between 1 and 2. It is important to note that the anti-parallel configuration does not simply result in the nearest neighbor local modes being nearly orthogonal to each other. For example, the relative angle between the middle core ring mode on molecule 1 and on molecule 2 is equal to 168 degrees. Thus, the coupling constants computed for this molecular configuration are not artificially diminished due to modes being nearly orthogonal to each other.

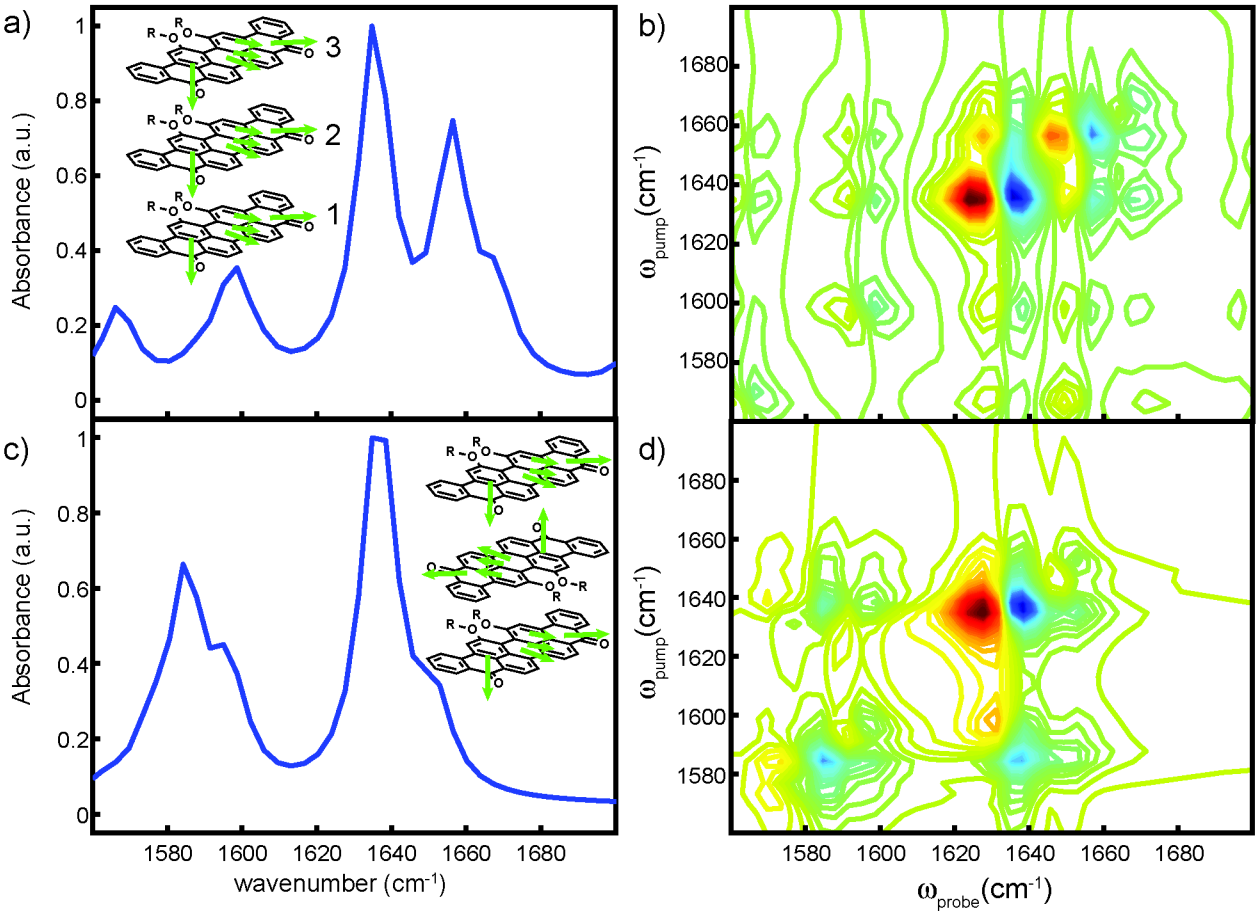

Figure 5.6a-d. Calculated linear IR absorption and 2D IR spectra of a) and b) parallel configurations and c) and d) anti-parallel configurations. The molecules are labeled 1-3 with the molecule on the bottom being molecule 1, as noted in a).

The TDC analysis of these idealized nanoaggregate structures provide insight to the intramolecular structure of self-assembled violanthrone-79 nanoaggregates. The parallel and anti-parallel structures cannot be distinguished using visible absorption spectroscopy. The linear IR absorption and 2D IR spectra calculated from the anti-parallel nanoaggregate structure most closely resemble the experimental spectra of self-assembled violanthrone-79 in chloroform. One could imagine that in reality the nanoaggregates consist of monomer units situated such that they have an angular distribution centered at 180 degrees. Linear and 2D IR spectra were calculated based on a weighted average of anti-parallel, +28 degrees from anti-parallel and -28 degrees

from anti-parallel. The spectra are illustrated in Figure 5.7 along with the experimental for comparison.

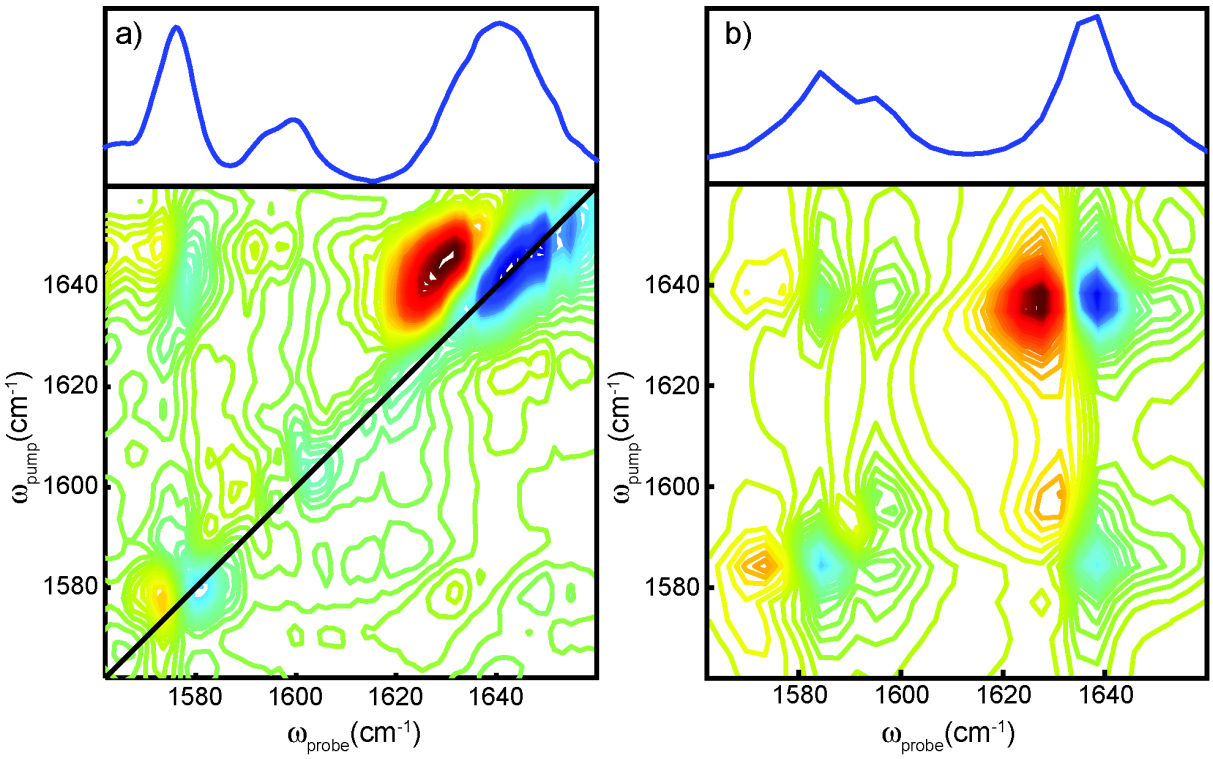

Figure 5.7a-b. Linear IR absorption and 2D IR spectra of a) experimental violanthrone in chloroform and b) a calculated spectra from a weighted average of 60% of the antiparallel configuration, 30% of the -28 degrees from antiparallel configuration, and 10% of the +28 degrees from antiparallel configuration.

The nanoaggregate linear IR absorption and 2D IR spectra consisting of the anti-parallel configuration, -28 degrees from anti-parallel configuration, and +28 degrees from anti-parallel configuration, contributing 60%, 30% and 10% respectively, produced calculated spectra that best reproduces the experimental spectra. For instance, the peak near 1640 cm^{-1} is broad in the experimental and the calculated spectra in Figure 5.7a-b. The intensities of the diagonal peaks in the calculated 2D IR spectrum are remarkably similar to the experimental 2D IR spectrum. In addition, the cross peaks are reproduced nicely. The results presented here indicate that the 2D

IR spectra are dominated by nanoaggregates that have an anti-parallel intramolecular configuration, with some angular disorder present. Moreover, the calculated linear IR absorption and 2D IR spectra of these idealized nanoaggregate structures demonstrate the sensitivity of 2D IR spectroscopy to the relative orientation of monomers in PAH nanoaggregates.

5.4. Conclusions

Two-dimensional infrared (2D IR) spectroscopy is a promising tool for probing PAH nanoaggregate formation due to the inherent structural sensitivity and high time resolution of the technique. 2D IR spectroscopy enables the direct measurement of vibrational coupling constants, which report on the structure of molecules. In this work, we determine a local mode basis suitable to model the natural vibrational signatures of violanthrone-79 in the monomeric and self-assembled nanoaggregates. The local mode basis we developed is informed by spectroscopic and computational investigations of anthrone and monomeric violanthrone-79. The information gained from the spectroscopic response of anthrone and monomeric violanthrone-79 is utilized to describe the spectroscopic response of self-assembled violanthrone-79. In order to describe the relative orientations of violanthrone-79 molecules within a nanoaggregate structure, we applied an electrostatic vibrational coupling model to three idealized nanoaggregate structures. TDC was used to calculate the vibrational coupling between nearest neighbors. In addition, angular disorder within the nanoaggregates was explored by perturbing the idealized structures. The analysis presented here demonstrates the sensitivity of 2D IR to the intramolecular structure of violanthrone-79 nanoaggregates. Based on this analysis, we propose that the predominant stacking configuration is anti-parallel for nanoaggregates produced from

violanthrone-79 self-assembly in chloroform and that some angular disorder exists in the nanoaggregate structures.

This investigation represents the first steps toward extending vibrational spectroscopy to investigate molecular order in self-assembled polycyclic aromatic molecules. The sensitivity of 2D IR to PAH nanoaggregate structure has now been clearly demonstrated. However, it is critical that future efforts include estimating the extent of vibrational delocalization along the aggregate and quantifying the number of molecules per aggregate. Moreover, we are now in a position to probe the influence of solvent environments on intermolecular nanoaggregate structure directly with 2D IR spectroscopy.

5.5 Additional Notes

The authors thank Tony Rappé for open access to their cluster and Melissa Reynolds for access to the linear IR absorption and UV-visible absorption spectrometers. A.T.K. appreciates the generous funding for this work from the ACS Petroleum Research Fund (grant #51228-DNI6).

References

(1) Cyran, J. D.; Krummel, A. T. Probing Structural Features of Self-Assembled Violanthrone-79 Using Two Dimensional Infrared Spectroscopy. *J. Chem. Phys.* **2015**, *142* (21), 212435.

(2) Hippius, C.; Schlosser, F.; Vysotsky, M. O.; Böhmer, V.; Würthner, F. Energy Transfer in Calixarene-Based Cofacial-Positioned Perylene Bisimide Arrays. *J. Am. Chem. Soc.* **2006**, *128* (12), 3870–3871.

(3) Wong, W. W. H.; Khoury, T.; Vak, D.; Yan, C.; Jones, D. J.; Crossley, M. J.; Holmes, A. B. A Porphyrin-Hexa-Peri-Hexabenzocoronene-Porphyrin Triad: Synthesis, Photophysical Properties and Performance in a Photovoltaic Device. *J. Mater. Chem.* **2010**, *20* (33), 7005–7014.

(4) Facchetti, A. Π-Conjugated Polymers for Organic Electronics and Photovoltaic Cell Applications. *Chem. Mater.* **2010**, *23* (3), 733–758.

(5) Wong, W. W. H.; Singh, T. B.; Vak, D.; Pisula, W.; Yan, C.; Feng, X.; Williams, E. L.; Chan, K. L.; Mao, Q.; Jones, D. J.; et al. Solution Processable Fluorenyl Hexa-Peri-Hexabenzocoronenes in Organic Field-Effect Transistors and Solar Cells. *Adv. Funct. Mater.* **2010**, *20* (6), 927–938.

(6) Mizoshita, N.; Tani, T.; Inagaki, S. Highly Conductive Organosilica Hybrid Films Prepared from a Liquid-Crystal Perylene Bisimide Precursor. *Adv. Funct. Mater.* **2011**, *21* (17), 3291–3296.

(7) Schmidt-Mende, L.; Fechtenkötter, A.; Müllen, K.; Moons, E.; Friend, R. H.; MacKenzie, J. D. Self-Organized Discotic Liquid Crystals for High-Efficiency Organic Photovoltaics. *Science* **2001**, *293* (5532), 1119–1122.

(8) Law, K. Y. Organic Photoconductive Materials: Recent Trends and Developments. *Chem. Rev.* **1993**, *93* (1), 449–486.

(9) Díaz-García, M. A.; Calzado, E. M.; Villalvilla, J. M.; Boj, P. G.; Quintana, J. A.; Céspedes-Guirao, F. J.; Fernández-Lázaro, F.; Sastre-Santos, Á. Effect of Structural Modifications in the Laser Properties of Polymer Films Doped with Perylenebisimide Derivatives. *Synth. Met.* **2009**, *159* (21–22), 2293–2295.

(10) Choi, H.; Paek, S.; Song, J.; Kim, C.; Cho, N.; Ko, J. Synthesis of Annulated Thiophene Perylene Bisimide Analogues: Their Applications to Bulk Heterojunction Organic Solar Cells. *Chem. Commun.* **2011**, *47* (19), 5509–5511.

(11) Speight, J. G. The Chemical and Physical Structure of Petroleum: Effects on Recovery Operations. *J. Pet. Sci. Eng.* **1999**, *22* (1–3), 3–15.

(12) Marshall, A. G.; Rodgers, R. P. Petroleomics: The Next Grand Challenge for Chemical Analysis. *Acc. Chem. Res.* **2003**, *37* (1), 53–59.

(13) Rogel, E. Studies on Asphaltene Aggregation via Computational Chemistry. *Colloids Surf. Physicochem. Eng. Asp.* **1995**, *104* (1), 85–93.

(14) Pierre, C.; Barré, L.; Pina, A.; Moan, M. Composition and Heavy Oil Rheology. *Oil Gas Sci. Technol.* **2004**, *59* (5), 489–501.

(15) Spiecker, P. M.; Gawrys, K. L.; Trail, C. B.; Kilpatrick, P. K. Effects of Petroleum Resins on Asphaltene Aggregation and Water-in-Oil Emulsion Formation. *Colloids Surf. Physicochem. Eng. Asp.* **2003**, *220* (1–3), 9–27.

(16) Jian, C.; Tang, T.; Bhattacharjee, S. Molecular Dynamics Investigation on the Aggregation of Violanthrone78-Based Model Asphaltenes in Toluene. *Energy Fuels* **2014**, *28* (6), 3604–3613.

(17) Teklebrhan, R. B.; Ge, L.; Bhattacharjee, S.; Xu, Z.; Sjöblom, J. Probing Structure–Nanoaggregation Relations of Polyaromatic Surfactants: A Molecular Dynamics Simulation and Dynamic Light Scattering Study. *J. Phys. Chem. B* **2012**, *116* (20), 5907–5918.

(18) Shi, M.-M.; Chen, Y.; Nan, Y.-X.; Ling, J.; Zuo, L.-J.; Qiu, W.-M.; Wang, M.; Chen, H.-Z. Π−π Interaction among Violanthrone Molecules: Observation, Enhancement, and Resulting Charge Transport Properties. *J. Phys. Chem. B* **2011**, *115* (4), 618–623.

(19) ANDREWS, A. B.; SHIH, W.-C.; MULLINS, O. C.; NORINAGA, K. Molecular Size Determination of Coal-Derived Asphaltene by Fluorescence Correlation Spectroscopy. *Appl. Spectrosc.* **2011**, *65* (12), 1348–1356.

(20) Sharma, A.; Groenzin, H.; Tomita, A.; Mullins, O. C. Probing Order in Asphaltenes and Aromatic Ring Systems by HRTEM. *Energy Fuels* **2002**, *16* (2), 490–496.

(21) Trejo, F.; Ancheyta, J.; Rana, M. S. Structural Characterization of Asphaltenes Obtained from Hydroprocessed Crude Oils by SEM and TEM. *Energy Fuels* **2009**, *23* (1), 429–439.

(22) Badre, S.; Carla Goncalves, C.; Norinaga, K.; Gustavson, G.; Mullins, O. C. Molecular Size and Weight of Asphaltene and Asphaltene Solubility Fractions from Coals, Crude Oils and Bitumen. *Fuel* **2006**, *85* (1), 1–11.

(23) Andrews, A. B.; Guerra, R. E.; Mullins, O. C.; Sen, P. N. Diffusivity of Asphaltene Molecules by Fluorescence Correlation Spectroscopy. *J. Phys. Chem. A* **2006**, *110* (26), 8093–8097.

(24) Jian, C.; Tang, T. One-Dimensional Self-Assembly of Polyaromatic Compounds Revealed by Molecular Dynamics Simulations. *J. Phys. Chem. B* **2014**, *118* (44), 12772–12780.

(25) Lisitza, N. V.; Freed, D. E.; Sen, P. N.; Song, Y.-Q. Study of Asphaltene Nanoaggregation by Nuclear Magnetic Resonance (NMR)†. *Energy Fuels* **2009**, *23* (3), 1189–1193.

(26) Jian, C.; Tang, T.; Bhattacharjee, S. Probing the Effect of Side-Chain Length on the Aggregation of a Model Asphaltene Using Molecular Dynamics Simulations. *Energy Fuels* **2013**, *27* (4), 2057–2067.

(27) Hamm, P.; Lim, M.; DeGrado, W. F.; Hochstrasser, R. M. The Two-Dimensional IR Nonlinear Spectroscopy of a Cyclic Penta-Peptide in Relation to Its Three-Dimensional Structure. *Proc. Natl. Acad. Sci.* **1999**, *96* (5), 2036–2041.

(28) Woutersen, S.; Hamm, P. Structure Determination of Trialanine in Water Using Polarization Sensitive Two-Dimensional Vibrational Spectroscopy. *J. Phys. Chem. B* **2000**, *104* (47), 11316–11320.

(29) Park, S.; Kwak, K.; Fayer, M. D. Ultrafast 2D-IR Vibrational Echo Spectroscopy: A Probe of Molecular Dynamics. *Laser Phys. Lett.* **2007**, *4* (10), 704.

(30) Zanni, M. T.; Gnanakaran, S.; Stenger, J.; Hochstrasser, R. M. Heterodyned Two-Dimensional Infrared Spectroscopy of Solvent-Dependent Conformations of Acetylproline-NH2†. *J. Phys. Chem. B* **2001**, *105* (28), 6520–6535.

(31) Ghosh, A.; Remorino, A.; Tucker, M. J.; Hochstrasser, R. M. 2D IR Photon Echo Spectroscopy Reveals Hydrogen Bond Dynamics of Aromatic Nitriles. *Chem. Phys. Lett.* **2009**, *469* (4–6), 325–330.

(32) DeFlores, L. P.; Ganim, Z.; Nicodemus, R. A.; Tokmakoff, A. Amide I′−II′ 2D IR Spectroscopy Provides Enhanced Protein Secondary Structural Sensitivity. *J. Am. Chem. Soc.* **2009**, *131* (9), 3385–3391.

(33) Middleton, C. T.; Woys, A. M.; Mukherjee, S. S.; Zanni, M. T. Residue-Specific Structural Kinetics of Proteins through the Union of Isotope Labeling, Mid-IR Pulse Shaping, and Coherent 2D IR Spectroscopy. *Methods* **2010**, *52* (1), 12–22.

(34) Krimm, S.; Bandekar, J. Vibrational Spectroscopy and Conformation of Peptides, Polypeptides, and Proteins. In *Advances in Protein Chemistry*; C.B. Anfinsen, J. T. E. and F. M. R., Ed.; Academic Press, 1986; Vol. 38, pp 181–364.

(35) Moran, A.; Mukamel, S. The Origin of Vibrational Mode Couplings in Various Secondary Structural Motifs of Polypeptides. *Proc. Natl. Acad. Sci. U. S. A.* **2004**, *101* (2), 506–510.

(36) Hamm, P.; Woutersen, S. Coupling of the Amide I Modes of the Glycine Dipeptide. *Bull. Chem. Soc. Jpn.* **2002**, *75* (5), 985–988.

(37) Krummel, A. T.; Zanni, M. T. DNA Vibrational Coupling Revealed with Two-Dimensional Infrared Spectroscopy: Insight into Why Vibrational Spectroscopy Is Sensitive to DNA Structure. *J. Phys. Chem. B* **2006**, *110* (28), 13991–14000.

(38) Krummel, A. T.; Mukherjee, P.; Zanni, M. T. Inter and Intrastrand Vibrational Coupling in DNA Studied with Heterodyned 2D-IR Spectroscopy. *J. Phys. Chem. B* **2003**, *107* (35), 9165–9169.

(39) Peng, C. S.; Jones, K. C.; Tokmakoff, A. Anharmonic Vibrational Modes of Nucleic Acid Bases Revealed by 2D IR Spectroscopy. *J. Am. Chem. Soc.* **2011**, *133* (39), 15650–15660.

(40) Fidder, H.; Yang, M.; Nibbering, E. T. J.; Elsaesser, T.; Röttger, K.; Temps, F. N–H Stretching Vibrations of Guanosine–Cytidine Base Pairs in Solution: Ultrafast Dynamics, Couplings, and Line Shapes. *J. Phys. Chem. A* **2013**, *117* (5), 845–854.

(41) Lee, C.; Park, K.-H.; Cho, M. Vibrational Dynamics of DNA. I. Vibrational Basis Modes and Couplings. *J. Chem. Phys.* **2006**, *125* (11), 114508.

(42) Cyran, J. D.; Nite, J. M.; Krummel, A. T. Characterizing Anharmonic Vibrational Modes of Quinones with Two-Dimensional Infrared Spectroscopy. *J. Phys. Chem. B* **2015**.

(43) Shim, S.-H.; Strasfeld, D. B.; Fulmer, E. C.; Zanni, M. T. Femtosecond Pulse Shaping Directly in the Mid-IR Using Acousto-Optic Modulation. *Opt. Lett.* **2006**, *31* (6), 838–840.

(44) Shim, S.-H.; Strasfeld, D. B.; Zanni, M. T. Generation and Characterization of Phase and Amplitude Shaped Femtosecond Mid-IR Pulses. *Opt. Express* **2006**, *14* (26), 13120–13130.

(45) Nite, J. M.; Cyran, J. D.; Krummel, A. T. Active Bragg Angle Compensation for Shaping Ultrafast Mid-Infrared Pulses. *Opt. Express* **2012**, *20* (21), 23912.

(46) Shim, S.-H.; Zanni, M. T. How to Turn Your Pump–probe Instrument into a Multidimensional Spectrometer: 2D IR and Vis Spectroscopies via Pulse Shaping. *Phys. Chem. Chem. Phys.* **2009**, *11* (5), 748–761.

(47) Frisch, M. J. *Gaussian 09. Revision D.01*.

(48) Scott, A. P.; Radom, L. Harmonic Vibrational Frequencies: An Evaluation of Hartree−Fock, Møller−Plesset, Quadratic Configuration Interaction, Density Functional Theory, and Semiempirical Scale Factors. *J. Phys. Chem.* **1996**, *100* (41), 16502–16513.

(49) McHale, J. L. *Molecular Spectroscopy*, 1st edition.; Prentice Hall: Upper Saddle River, N.J, 1998.

(50) See Supplementary Material for the Details of Other Calculated Spectra.

Chapter 5 Supplemental Information

The remaining calculated spectra are illustrated in Figure S5.1. The configurations are a chiral 28 degrees from parallel, an aggregate with only the second molecule rotated +28 degrees from parallel, an aggregate with only the second molecule rotated -28 degrees from parallel, an aggregate with only the second molecule rotated -28 degrees from antiparallel, and an aggregate with only the second molecule rotated +28 degrees from antiparallel. The rotation for each aggregate was only around the z-axis in the calculation. The molecules 2 in Figure S5.1 are rotated ±28 degrees from molecules 1 however the rotation perturbs the molecules in all directions

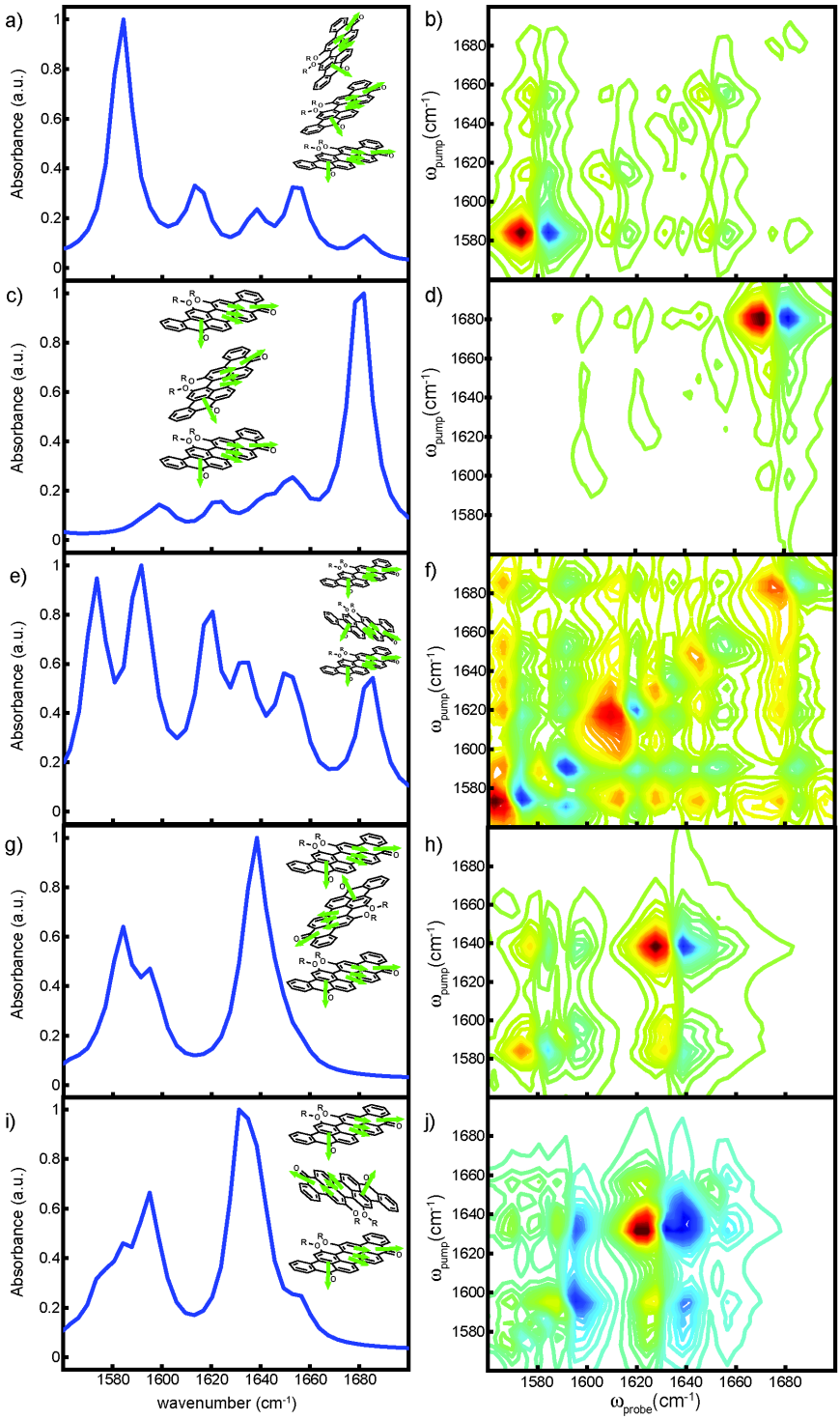

Figure S5.1. Simulated linear IR absorption and 2D IR spectra of a) and b) chiral 28 degrees from parallel configurations, c) and d) an aggregate with only the second molecule rotated +28 degrees from parallel, e) and f) an aggregate with only the second molecule rotated -28 degrees from parallel, g) and h) an aggregate with only the second molecule rotated -28 degrees from antiparallel and i) and j) an aggregate with only the second molecule rotated +28 degrees from antiparallel**.** The molecules are labeled 1-3 with the molecule on the bottom being molecule 1, as noted in a).

Chapter 6

Ultrafast Vibrational Dynamics and Structural Features Probed for an Aggregated Perylene Derivative Using Two-Dimensional Infrared Spectroscopy

6.1. Introduction

Noncovalent supramolecular interactions have important roles in material and biological sciences. For instance, there are self-assembled chlorophyll dyes in photosynthesis,[1] and the tobacco mosaic virus self assembles into disk-shaped subunits.[2] These self-assembly mechanisms are critical for processes, such as photosynthesis, to continue. On one hand, these well-structured natural supramolecules are often the end goal for synthetic molecules to be used for materials or semiconductors. On the other hand, self-assembly processes can be unwarranted in systems such as asphaltene nanoaggregation. Understanding self-assembly processes is critical for preventing the corrosion and fouling of oil pipelines due to asphaltene aggregation. Regardless of the application, the self-assembly processes are intriguing and need to be studied to understand how to mimic the formation of supramolecules or inhibit the formation of nanoaggregates from occurring.

One synthetic dye used to study aggregation processes is perylene derivatives. Perylene derivative dyes are planar π-conjugated molecules known to self organize because of the intermolecular forces, mostly π-π interactions. Perylene derivative dyes are used for their self-assembling abilities as well as their ability to be n-type semiconductors and as pigments with a large range of colors.[3–5] Perylene derivatives have the ability to form both H- and J-aggregates.[6]

The versatility of the perylene derivative molecules makes them ideal as model compounds for different complex systems.

Many studies have been completed on perylene derviative molecules to determine the structure of the self-assembled molecules. Crystallography studies have been completed to determine the distance between stacked perylene derivative molecules. Based on crystallography measurements on substituted perylene derivatives, the dye molecules are stacked as close as 3.4 Å apart. The addition of substituents can cause the molecules to stack farther apart at 4.6 Å.[4] Thus, self-assembled perylene derivatives can be tailored into desired configurations for different materials or changed to best resemble asphaltenes found in different locations.

Other techniques including UV-vis absorption and fluorescence emission spectroscopic studies have been completed on perylene derivatives as well.[7] The nonlinearity in temperature UV-vis experiments and concentration dependent UV-vis experiments illustrates the self-assembly process of the PDI molecules. However, UV-vis absorption does not report on the orientation of the molecules in the aggregate.

The stacked dimer structure of a perylene bisimide (PBI) was probed with NMR and molecular modeling. The results indicated the dimer is stacked 3.46 Å apart and had a rotational angle of 26° for each molecule.[8] The separation between stacked perylene molecules is also similar to results found by molecular dynamic simulations.[9] While the formation of larger aggregates is discussed, studies to determine the number of molecules per aggregate and to determine the structure of the larger aggregates have not been completed. Two-dimensional infrared spectroscopy (2D IR) has the potential to probe the structural features of the nanoaggregates beyond dimer formation. 2D IR spectroscopy is a technique that offers high time resolution and structural sensitivity. 2D IR spectroscopy has been used to obtain

information of molecular structures[10,11] and dynamics of molecular systems.[12,13] Extending 2D IR spectroscopy to the nanoaggregate PDI system provides valuable insight into the self-assembly process.

The work presented in this chapter describes the ultrafast vibrational dynamics and the structural information probed for a perylene derivative, *N*,*N*'-bis(2,6-diisopropylphenyl)-3,4,9,10-perylenetetracarboxylic diimide (PDI) using linear and nonlinear vibrational spectroscopy. The nanoaggregate structure of PDI can be probed using 2D IR spectroscopy. Also, 2D IR spectroscopy is used to look at the ultrafast dynamics on the femtosecond time scale. Waiting time experiments provide the dynamics information on the PDI system. Probing the structural features and the dynamics of the PDI system are important for understanding the self-assembly process.

6.2. Methods and Materials

6.2.1. UV-vis Spectroscopy

UV-vis spectroscopy experiments were completed on a Nicolet Evolution 300 spectrophotometer (Thermo Electron Corporation). The PDI samples were prepared at room temperature with varying concentrations. *N*,*N*'-Bis(2,6-diisopropylphenyl)-3,4,9,10-perylenetetracarboxylic diimide (PDI) was purchased from TCI America, and chloroform (ACS grade) was purchased from Fisher Scientific. PDI samples were placed between two CaF_2 windows with a 25 micron Teflon spacer. The UV-vis spectra were baseline corrected using MATLAB.

6.2.2. Linear IR Absorption Spectroscopy

Linear IR absorption spectra were collected at room temperature using a Nicolet 6700 spectrometer (Thermo Fisher Scientific). Samples prepared for linear IR absorption experiments were similar to UV-vis with the exception of the Teflon spacer thickness, using a 200 micron spacer. The spectral resolution was 4 cm^{-1} and 64 scans were averaged per spectrum. The Omnic software was used to collect the spectra, to correct for atmospheric suppression, and to subtract the air background. A percentage of chloroform was subtracted from the spectra, and the baseline was corrected using MATLAB code.

6.2.3. 2D IR Spectroscopy

PDI samples, prepared similarly to linear IR absorption experiments, were studied using 2D IR spectroscopy. A description of the spectrometer and experimental setup can be found elsewhere.[14] 2D IR spectroscopy involves three mid-IR pulse interactions at a sample to produce a third order signal. The mid-IR light, centered at 6100 nm, was split into a probe pathway and majority going to the pump pathway. The pump light is directed to a Ge-based pulse shaper, which produces pump-pulse pairs with controllable time delays and phases. The pump and the probe are directed towards a parabolic mirror, used to focus the beams in the sample. The third order signal follows the probe beam and is detected on a 64-element mercury cadmium telluride (MCT) array. The pump delay was scanned from 0 to 2500 fs with a 7 fs step size. The waiting time experiments were scanned out to 2 ps with steps of 200 fs. The polarization was set to parallel for all of these experiments.

6.3. Results and Discussion

The structure of the PDI compound used in the experiments in this chapter can be found in Figure 6.1a. This specific PDI was chosen over other perylene derivatives due to the solubility and the ability to self-assemble at high concentrations. This PDI is soluble in chloroform until about 15 mM. The self-assembly process is monitored with UV-vis experiments. UV-vis spectra of PDI in chloroform are shown in Figure 6.1b. There are four main peaks in the UV-vis spectra: 435 nm, 459 nm, 491 nm, and 527 nm. The concentration for the UV-vis spectra ranged from 0.5 mM to 10 mM. The plot of the intensity of each peak with respect to the concentration is illustrated in Figure 6.1c. The intensity of peaks at 491 nm and 527 nm are nonlinear above 6 mM concentration. The nonlinearity implies an aggregation process occurring at concentrations above 6 mM. Previous studies have found that the aggregation occurs at 2 mM of similar perylene derivatives in chloroform.[7] Of course, the aggregation process is solvent dependent and also depends on the exact perylene derivative.

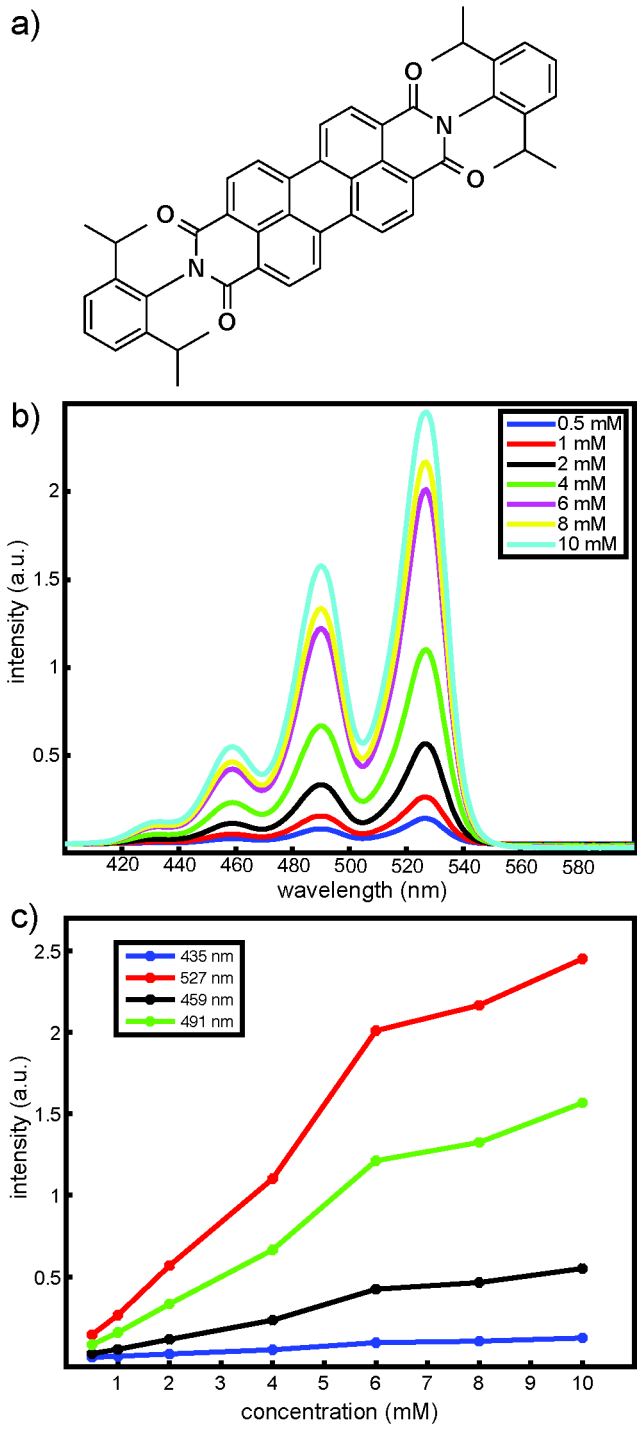

Figure 6.1 a) Molecular structure of *N*,*N*'-bis(2,6-diisopropylphenyl)-3,4,9,10-perylenetetracarboxylic diimide. b) UV-vis spectra of PDI in chloroform with concentration ranging from 0.5 mM to 10 mM. c) A plot of the absorption versus concentration for four different UV-vis absorption peaks: 435 nm, 459 nm, 491 nm and 527 nm.

Linear IR absorption and 2D IR spectra were collected on 1 mM, 5 mM, and 10 mM PDI in chloroform in the spectral region from 1500 to 1800 cm^{-1}. An example of the linear IR absorption and 2D IR spectra of 10 mM PDI in chloroform is shown in Figure 6.2 in the spectral region from 1635 to 1720 cm^{-1}. The peaks in the linear IR absorption spectrum and the diagonal peaks in the 2D IR spectrum correspond to the symmetric and antisymmetric carbonyl stretching vibrational modes. The cross peaks in the 2D IR spectrum at T_w=0 fs are indicative of vibrational coupling between the symmetric and antisymmetric carbonyl stretch. The blue peaks in the 2D IR spectra are negative and correspond to a v=0-1 transition. The red peaks are positive and correspond to a v=1-2 transition.

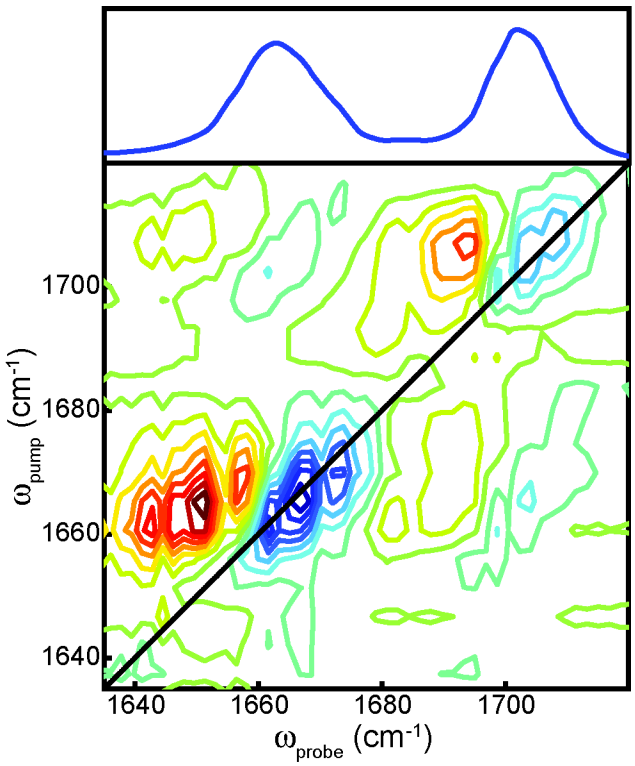

Figure 6.2 Linear IR absorption and 2D IR spectra of 10 mM PDI in chloroform. The spectra are of the carbonyl stretch vibrational mode region from 1635 to 1720 cm^{-1}. The peaks along the diagonal correspond to the symmetric and antisymmetric carbonyl stretching vibration. The cross peaks are indicative of vibrational coupling between the symmetric and antisymmetric carbonyl stretching vibrational modes.

Other regions of interest include the ring breathing vibrational modes from 1550 cm^{-1} to 1650 cm^{-1}. An example 2D IR spectrum of the spectral region from 1550 to 1650 is illustrated in Figure 6.3a. There are also cross peaks between the two different ring breathing vibrational modes. Figure 6.3b is a full spectrum of the carbonyl stretching and the ring breathing vibrational modes. While the cross peaks between the two carbonyl modes and between the two ring modes are intense, the cross peaks between the ring and the carbonyl peaks are weak. This is different compared to the 2D IR spectrum of violanthrone-79 in chloroform, which has intense cross peaks between the ring and carbonyl vibrational modes.[15]

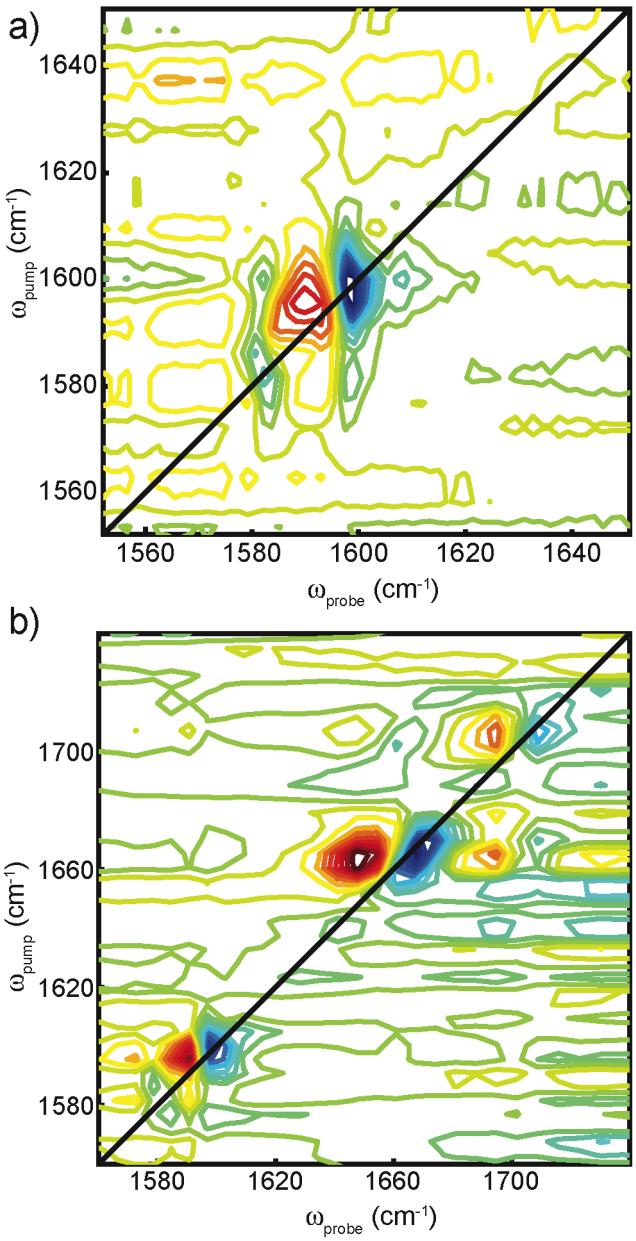

Figure 6.3 2D IR spectra of 5 mM PDI in chloroform. a) The spectrum is of the ring breathing vibrational mode region from 1550 to 1650 cm^{-1}. The peaks along the diagonal correspond to the fundamental ring breathing vibrations. The cross peaks are indicative of vibrational coupling between the ring breathing vibrational modes. b) The spectrum is of both the ring breathing and carbonyl stretching vibrational modes.

Dynamic cross peaks are also seen in 2D IR spectra with waiting time experiments.[16] Waiting time experiments are completed by stepping the time between the second pump pulse and the probe pulse, known as T_w. This is completed using a computer delay stage to step the probe pulse. The probe pulse was stepped from 0 fs to 2000 fs in these experiments. Dynamic cross peaks result from population relaxation, population transfer, and chemical exchange processes.[17–19] The waiting time experiments completed on PDI in chloroform revealed dynamic cross peaks. An example of a waiting time spectrum at 200 fs of 10 mM PDI in chloroform is illustrated in Figure 6.4a. Figure 6.4b is zoomed into the upper left cross peaks from Figure 6.4a. The intensity was recorded for the sum of the absolute value within this area and was completed for all time from 0 fs to 2000 fs. A plot of the intensity of the cross peaks with respect to time is shown in Figure 6.4c. The cross peaks oscillate in intensity as the waiting time is changed. The oscillations occur every 200 fs based on the plot in Figure 6.4c. Oscillations in the integrated cross peak intensities have been seen previously and the time intervals of the oscillations vary with the molecular system.[19] The oscillations of the cross peaks could be due to exciton transport.[20]

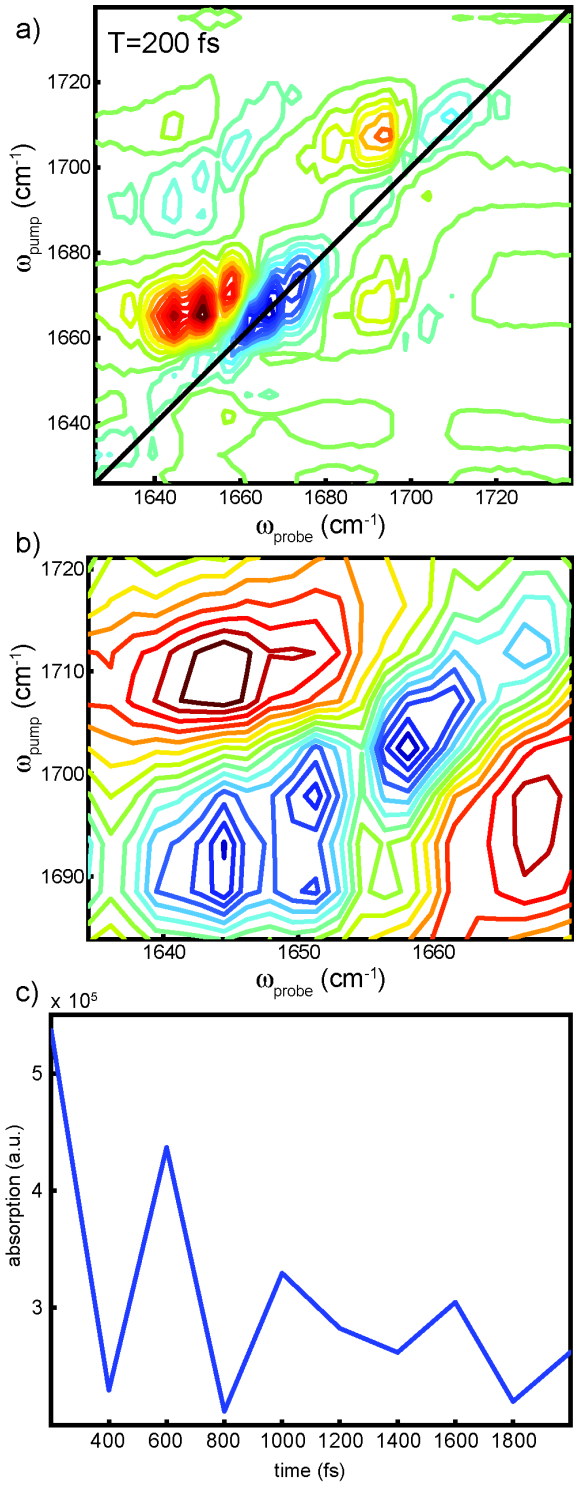

Figure 6.4. a) Waiting time experiments were completed on PDI in chloroform from T_w=200 fs to 2000 fs. b) Area integrated for analyzing oscillating cross peaks. The sum of the absolute value of the cross peaks was determined for each T-waiting time. c) Plot of absorption of cross peak intensity versus the waiting time.

6.4. Conclusion

The structure and dynamics of self-assembled PDI have been probed using 2D IR spectroscopy. This chapter represents only the initial studies completed on studying PDI with 2D IR spectroscopy. 2D IR spectroscopy is sensitive to the structure of PAH nanoaggregates in the solvent environment. The vibrational dynamics of the PDI in chloroform were also studies with 2D IR spectroscopy. 2D IR spectroscopy is a high time resolution technique and can measure event occurring on the femtosecond time scale.

Future work to calculate a 2D IR spectrum of the aggregated structure is essential for understanding the rotational angle between molecules in an aggregate. The aggregated structure will depend on the number of molecules per aggregate and the distance between the molecules in the nanoaggregate. The calculations would be similar to those completed on violanthrone-79.[15] A comparison between violanthrone-79 and perylene derivatives would shed light on the differences in stack nanoaggregate structures based on the position of the aliphatic side chains on the PAH molecules.

6.5. Additional Notes

The authors would like to thank Tony Rappé for open access to the cluster and Melissa Reynolds for access to the linear IR absorption and UV-visible absorption spectrometers.

References

(1) Krasnovsky, A. A.; Bystrova, M. I. Self-Assembly of Chlorophyll Aggregated Structures. *Biosystems* **1980**, *12* (3–4), 181–194.

(2) Klug, A. The Tobacco Mosaic Virus Particle: Structure and Assembly. *Philos. Trans. R. Soc. Lond. B Biol. Sci.* **1999**, *354* (1383), 531–535.

(3) Dimitrakopoulos, C. d.; Malenfant, P. r. l. Organic Thin Film Transistors for Large Area Electronics. *Adv. Mater.* **2002**, *14* (2), 99–117.

(4) Würthner, F. Perylene Bisimide Dyes as Versatile Building Blocks for Functional Supramolecular Architectures. *Chem. Commun.* **2004**, No. 14, 1564–1579.

(5) Li, C.; Wonneberger, H. Perylene Imides for Organic Photovoltaics: Yesterday, Today, and Tomorrow. *Adv. Mater.* **2012**, *24* (5), 613–636.

(6) Fennel, F.; Wolter, S.; Xie, Z.; Plötz, P.-A.; Kühn, O.; Würthner, F.; Lochbrunner, S. Biphasic Self-Assembly Pathways and Size-Dependent Photophysical Properties of Perylene Bisimide Dye Aggregates. *J. Am. Chem. Soc.* **2013**, *135* (50), 18722–18725.

(7) Dehm, V.; Büchner, M.; Seibt, J.; Engel, V.; Würthner, F. Foldamer with a Spiral Perylene Bisimide Staircase Aggregate Structure. *Chem. Sci.* **2011**, *2* (11), 2094.

(8) Shao, C.; Grüne, M.; Stolte, M.; Würthner, F. Perylene Bisimide Dimer Aggregates: Fundamental Insights into Self-Assembly by NMR and UV/Vis Spectroscopy. *Chem. – Eur. J.* **2012**, *18* (43), 13665–13677.

(9) Marcon, V.; Breiby, D. W.; Pisula, W.; Dahl, J.; Kirkpatrick, J.; Patwardhan, S.; Grozema, F.; Andrienko, D. Understanding Structure−Mobility Relations for Perylene Tetracarboxydiimide Derivatives. *J. Am. Chem. Soc.* **2009**, *131* (32), 11426–11432.

(10) Hamm, P.; Lim, M.; DeGrado, W. F.; Hochstrasser, R. M. The Two-Dimensional IR Nonlinear Spectroscopy of a Cyclic Penta-Peptide in Relation to Its Three-Dimensional Structure. *Proc. Natl. Acad. Sci.* **1999**, *96* (5), 2036–2041.

(11) Demirdöven, N.; Cheatum, C. M.; Chung, H. S.; Khalil, M.; Knoester, J.; Tokmakoff, A. Two-Dimensional Infrared Spectroscopy of Antiparallel B-Sheet Secondary Structure. *J. Am. Chem. Soc.* **2004**, *126* (25), 7981–7990.

(12) Fayer, M. D. Dynamics of Liquids, Molecules, and Proteins Measured with Ultrafast 2D IR Vibrational Echo Chemical Exchange Spectroscopy. *Annu. Rev. Phys. Chem.* **2009**, *60* (1), 21–38.

(13) Elsaesser, T.; Huse, N.; Dreyer, J.; Dwyer, J. R.; Heyne, K.; Nibbering, E. T. J. Ultrafast Vibrational Dynamics and Anharmonic Couplings of Hydrogen-Bonded Dimers in Solution. *Chem. Phys.* **2007**, *341* (1–3), 175–188.

(14) Cyran, J. D.; Nite, J. M.; Krummel, A. T. Characterizing Anharmonic Vibrational Modes of Quinones with Two-Dimensional Infrared Spectroscopy. *J. Phys. Chem. B* **2015**.

(15) Cyran, J. D.; Krummel, A. T. Probing Structural Features of Self-Assembled Violanthrone-79 Using Two Dimensional Infrared Spectroscopy. *J. Chem. Phys.* **2015**, *142* (21), 212435.

(16) Hamm, P.; Zanni, M. T. *Concepts and Methods of 2D Infrared Spectroscopy*; Cambridge, 2011.

(17) Cheng, Y.-C.; Engel, G. S.; Fleming, G. R. Elucidation of Population and Coherence Dynamics Using Cross-Peaks in Two-Dimensional Electronic Spectroscopy. *Chem. Phys.* **2007**, *341* (1–3), 285–295.

(18) Kwak, K.; Zheng, J.; Cang, H.; Fayer, M. D. Ultrafast Two-Dimensional Infrared Vibrational Echo Chemical Exchange Experiments and Theory†. *J. Phys. Chem. B* **2006**, *110* (40), 19998–20013.

(19) Khalil, M.; Demirdöven, N.; Tokmakoff, A. Vibrational Coherence Transfer Characterized with Fourier-Transform 2D IR Spectroscopy. *J. Chem. Phys.* **2004**, *121* (1), 362–373.

(20) Mukamel, S.; Abramavicius, D. Many-Body Approaches for Simulating Coherent Nonlinear Spectroscopies of Electronic and Vibrational Excitons. *Chem. Rev.* **2004**, *104* (4), 2073–2098.

Chapter 7

Conclusions/Future Work

7.1. Conclusions

2D IR spectroscopy was determined to be an optimal technique to study the nanoaggregate structure of model asphaltenes, violanthrone-79 and lumogen orange, in chloroform. 2D IR spectroscopy offers both femtosecond time resolution and structural resolution needed to study the nanoaggregate structure and the dynamics of nanoaggregation. The 2D IR spectrometer used in this thesis consisted of mid-IR pulse shaper techniques with active-Bragg correction. The first step was to understand ring breathing and carbonyl stretching vibrational mode. A quinone series of benzoquinone, naphthoquinone, and anthraquinone was studied to understand the ring breathing and carbonyl stretching vibrational mode coupling. The anharmonicities were extracted and can be used to calculate the vibrational coupling. The coupling can also be extracted by inverting the 1-quantum Hamiltonian. It should be noted that for the quinone series the two vibrational coupling parameters extracted from the 2D IR experimental anharmonicities and the coupling extracted from inverting the 1-quantum anharmonicity varied by orders of magnitude. The quinone series set the foundation for the larger PAHs, and similar anharmonicities, both diagonal and off-diagonal, were found for the quinone series and the larger PAHs.

The structural features of nanoaggregate violanthrone-79 were probed using anthrone and monomer violanthrone-79 as local mode basis. UV-Vis, linear IR absorption, and 2D IR absorption were the experimental techniques used to study the nanoaggregate structure of

violanthrone in chloroform. The 2D IR spectra were calculated using the local mode basis on different trimer configurations. This work concluded that the H-aggregated structure of violanthrone-79 was for the majority antiparallel with a distribution including contributions from ±28 degrees from antiparallel. The calculated 2D IR spectra were based on a trimer, and future work could benefit from a sixmer or larger nanoaggregate.

Lumogen orange results indicate vibrational coupling between the antisymmetric and symmetric carbonyl stretch, as well as the ring vibrational modes. 2D IR waiting time experiments were completed and illustrated the oscillation of the presence and disappearance of cross peaks. Thus, there is a vibrational energy flow between the vibrational modes.

7.2. Future Work

There are many pathways that this work can be continued. The first avenue is to look at polarization studies of the quinone series. The goal of the polarization studies is to determine the angle of the transition dipole for the ring breathing and carbonyl stretching vibrational modes. The angle is important for determining the coupling between vibrational modes. The polarization studies need to be completed using a BOXcars setup. The polarization needs to be set to -45°,45°,90°,0°.

The model asphaltene work, with violanthrone-79 and lumogen orange, would benefit from 2D IR experiments in different solvents and different mixtures of solvents. Differing the mixture of solvents is another way to probe the nanoaggregation structure and the dynamics of the system. One experiment that could be completed is to study the kinetic of the nanoaggregation by using a flow cell and adding *n*-heptane to a solution of the model asphaltenes in toluene or chloroform. The kinetics of the nanoaggregation would be helpful for remedying the clogging of

oil pipelines. If the nanoaggregation could be halted when the aggregates reach a certain size, the potential of clogging and fouling the pipelines could decrease. The ultimate goal is to know in which conditions and solvents the nanoaggregation occurs and then to use the data to correct or mitigate the problem. There are still many great questions that need to be answered. The work completed in this thesis is the beginning to answering the question of asphaltene nanoaggregation.

Appendix I

MATLAB Programs

A1.1. MATLAB Program Used to Simulate 1D- and 2D IR Spectra

This example code is for a 15-oscillator system. This is used to calculated 1D- and 2D IR spectra of a violanthrone-79 trimer.

```
%% First vibrational states
s=15; %number of oscillators total
E1=[1579 1606 1606 1632 1632,...
   1579 1606 1606 1632 1632,...
   1579 1606 1606 1632 1632];
dipole_strength=1; %1; %oscillator strength in Debye (D)
dipole_strength_r=0.6; %oscillator strength in Debye (D)
dipole_strength_r2=1.3;
anharm=10;
anharm_2=5;

%% Loading the coordinates
dipole = [0.82415,0.40985,5.0801;...
   1.1033,0.51113,6.5755;...
   -0.20011,0.9733,1.8891;...
   0.54562,-0.18132,-2.0467;...
   -0.12531,0.46646,4.8517;...
   0.53527,0.74879,5.0801;...
   0.7342,0.96927,6.5755;...
   -0.63362,0.76543,1.8891;...
   0.56688,0.096057,-2.0467;...
   -0.32963,0.35303,4.8517;...
   0.82415,0.40985,5.0801;...
   1.1033,0.51113,6.5755;...
   -0.20011,0.9733,1.8891;...
   0.54562,-0.18132,-2.0467;...
   -0.12531,0.46646,4.8517];

for i=1:s
dipoley(i,:) = dipole(i,:)./sqrt(sum(dipole(i,:).^2));
```

```
end

dipoles2=dipoley(6:10,3)+4.5;
dipoles3=dipoley(11:15,3)+4.5;

dipoles = [dipoley(1:5,1) dipoley(1:5,2) dipoley(1:5,3);...
    dipoley(6:10,1) dipoley(6:10,2) dipoles2(:,1);...
    dipoley(11:15,1) dipoley(11:15,2) dipoles3(:,1)];
ur_c = dipoles(1,:)*dipole_strength_r2;
ur = dipoles(2:3,:)*dipole_strength_r;
uc = dipoles(4:5,:)*dipole_strength;
ur2_c = dipoles(6,:)*dipole_strength_r2;
ur2 = dipoles(7:8,:)*dipole_strength_r;
uc2 = dipoles(9:10,:)*dipole_strength;
ur3_c = dipoles(11,:)*dipole_strength_r2;
ur3 = dipoles(12:13,:)*dipole_strength_r;
uc3 = dipoles(14:15,:)*dipole_strength;

u=[ur_c(1,:);ur(1,:);ur(2,:);uc(1,:);uc(2,:);...
    ur2_c(1,:);ur2(1,:);ur2(2,:);uc2(1,:);uc2(2,:);...
    ur3_c(1,:);ur3(1,:);ur3(2,:);uc3(1,:);uc3(2,:)];

%%TDC input
B=zeros(s,s);
B(1:5,1:5) =[0 -5.7 -5.7 0 0;...
   -5.7 0 -2.5 12.5 12.5;...
   -5.7 -2.5 0 -12.5 12.5;...
   0 12.5 -12.5 0 -4.5;...
   0 12.5 12.5 -4.5 0];

B(6:10,1:5)=[26.1197037194460,11.9798134579243,10.5780465483059,-2.84257759382743,-
16.0017937728823;...
    11.9046509249003,5.45992645244368,4.81615462334745,-1.29907654320631,-
7.32198510315157;...
    8.00307205500803,3.66558103191612,3.06874042433609,-0.991108861668857,-
5.88968376268479;...
    -41.5491165924275,-19.1937948687386,-
21.5295553906937,2.13359794346100,0.0748207094653921;...
    -1.71403379993968,-0.806018130604902,-1.37507476469635,-
0.338207466296945,13.3875894645402];

B(1:5,6:10)=[26.1197037194460,11.9046509249003,8.00307205500803,-41.5491165924275,-
1.71403379993968;...
    11.9798134579243,5.45992645244368,3.66558103191612,-19.1937948687386,-
0.806018130604902;...
    10.5780465483059,4.81615462334745,3.06874042433609,-21.5295553906937,-
```

```
1.37507476469635;...
   -2.84257759382743,-1.29907654320631,-0.991108861668857,2.13359794346100,-
0.338207466296945;...
   -16.0017937728823,-7.32198510315158,-
5.88968376268479,0.0748207094653910,13.3875894645402];

B(6:10,6:10) = [0 -5.7 -5.7 0 0;...
  -5.7 0 -2.5 12.5 12.5;...
  -5.7 -2.5 0 -12.5 12.5;...
  0 12.5 -12.5 0 -4.5;...
  0 12.5 12.5 -4.5 0];

B(11:15,6:10)=[40.7658259347637,18.6901146128335,16.2645616406313,-
7.08821645329145,1.97696118237908;...
   18.8067541566347,8.62281063485076,7.51654779825914,-
3.26142100728856,0.885547558519235;...
   20.2604867127939,9.30204348892915,8.53275870904156,-
3.22715632920842,0.0748118488402671;...
   -12.5394082045566,-5.74904216097540,-5.00415536748168,10.8340923821469,-
1.04750043658417;...
   -6.03792293148544,-2.78888794844622,-3.11645510636626,-
0.452738982259051,11.4718730013574];

B(6:10,11:15)=[40.7658259347637,18.8067541566347,20.2604867127939,-
12.5394082045566,-6.03792293148544;...
   18.6901146128335,8.62281063485076,9.30204348892915,-5.74904216097540,-
2.78888794844622;...
   16.2645616406313,7.51654779825914,8.53275870904156,-5.00415536748168,-
3.11645510636626;...
   -7.08821645329145,-3.26142100728856,-3.22715632920842,10.8340923821469,-
0.452738982259051;...
   1.97696118237908,0.885547558519235,0.0748118488402665,-
1.04750043658417,11.4718730013574];

B(11:15,11:15) =[0 -5.7 -5.7 0 0;...
  -5.7 0 -2.5 12.5 12.5;...
  -5.7 -2.5 0 -12.5 12.5;...
  0 12.5 -12.5 0 -4.5;...
  0 12.5 12.5 -4.5 0];

%% Eigenstates
E0=diag(E1)+B;
[V1, D1] = eig(E0); %D1 is a matrix containing the eigenvalues of H1 and V1 is a matrix
containing the corresponding eigenvectors listed in column form
E1n = diag(D1); %Defines the eigenenergy of the oscillators
u1m(:,1:3) = (u.'*V1).'; %The transition dipole moments after diagonalization
```

```
% u1m=u;


%% plot linear

w=E1n;
mu=u1m;
n_t = 1024;
dt = 9e-15; %fs
T2 = 1000e-15; %dephasing time
c = 2*pi; %unit conversion factor
wf=w*3e10; %Hz
R = zeros(n_t);
R = R(1,:);
t = (0:n_t-1)*dt;

mui=zeros(s,3);
for ii = 1:s
   mui(ii,:) = sqrt(mu(ii,:)*mu(ii,:)');
end


for j = 1:s
   ker = mui(j)^2*exp(-1i*wf(j)*c.*t - (t)/T2);
  for i  = 1:s
   R = R - mui(i)^2 * ker;
  end
end

R = R/2;
% xc=-R(:,:);

R= fftshift(fft2(real(R)));
R = fliplr(circshift(R,[0 -1]));
% figure()
% xf=fftshift(fft(real(xc)));
% plot(real(xf))

step=dt;
n=length(t);
q=1/(n*step);
i=0:length(t)-1;
wf=((i.*q)-(1/(2*step)));
ww=wf/(3e10);
R=real(-R')./max(real(-R'));
figure(8)
```

```
plot(ww,R,'b')
xlim([1560 1700])
ylim([-0.05 1.05])

%%2 quantum
E1=E1n;
E0=[2*E1(1,:) 2*E1(2,:) 2*E1(3,:) 2*E1(4,:) 2*E1(5,:), 2*E1(6,:),...
   2*E1(7,:) 2*E1(8,:) 2*E1(9,:) 2*E1(10,:),2*E1(11,:) 2*E1(12,:) 2*E1(13,:) 2*E1(14,:)
2*E1(15,:),...
   E1(1,:)+E1(2,:) E1(1,:)+E1(3,:) E1(1,:)+E1(4,:) E1(1,:)+E1(5,:) E1(1,:)+E1(6,:),...
   E1(1,:)+E1(7,:) E1(1,:)+E1(8,:) E1(1,:)+E1(9,:) E1(1,:)+E1(10,:),...
   E1(1,:)+E1(11,:) E1(1,:)+E1(12,:) E1(1,:)+E1(13,:) E1(1,:)+E1(14,:) E1(1,:)+E1(15,:),...
   E1(2,:)+E1(3,:) E1(2,:)+E1(4,:) E1(2,:)+E1(5,:) E1(2,:)+E1(6,:),...
   E1(2,:)+E1(7,:) E1(2,:)+E1(8,:) E1(2,:)+E1(9,:) E1(2,:)+E1(10,:),...
   E1(2,:)+E1(11,:) E1(2,:)+E1(12,:) E1(2,:)+E1(13,:) E1(2,:)+E1(14,:)  E1(2,:)+E1(15,:),...
   E1(3,:)+E1(4,:) E1(3,:)+E1(5,:)  E1(3,:)+E1(6,:) E1(3,:)+E1(7,:) E1(3,:)+E1(8,:)
E1(3,:)+E1(9,:),...
   E1(3,:)+E1(10,:) E1(3,:)+E1(11,:)  E1(3,:)+E1(12,:) E1(3,:)+E1(13,:) E1(3,:)+E1(14,:)
E1(3,:)+E1(15,:),...
   E1(4,:)+E1(5,:) E1(4,:)+E1(6,:) E1(4,:)+E1(7,:) E1(4,:)+E1(8,:) E1(4,:)+E1(9,:),...
   E1(4,:)+E1(10,:) E1(4,:)+E1(11,:) E1(4,:)+E1(12,:) E1(4,:)+E1(13,:) E1(4,:)+E1(14,:)
E1(4,:)+E1(15,:),...
   E1(5,:)+E1(6,:) E1(5,:)+E1(7,:) E1(5,:)+E1(8,:) E1(5,:)+E1(9,:) E1(5,:)+E1(10,:),...
   E1(5,:)+E1(11,:) E1(5,:)+E1(12,:) E1(5,:)+E1(13,:) E1(5,:)+E1(14,:) E1(5,:)+E1(15,:),...
   E1(6,:)+E1(7,:) E1(6,:)+E1(8,:) E1(6,:)+E1(9,:) E1(6,:)+E1(10,:),...
   E1(6,:)+E1(11,:) E1(6,:)+E1(12,:) E1(6,:)+E1(13,:) E1(6,:)+E1(14,:) E1(6,:)+E1(15,:),...
   E1(7,:)+E1(8,:) E1(7,:)+E1(9,:) E1(7,:)+E1(10,:),...
   E1(7,:)+E1(11,:) E1(7,:)+E1(12,:) E1(7,:)+E1(13,:) E1(7,:)+E1(14,:) E1(7,:)+E1(15,:),...
   E1(8,:)+E1(9,:) E1(8,:)+E1(10,:) E1(8,:)+E1(11,:) E1(8,:)+E1(12,:),...
   E1(8,:)+E1(13,:) E1(8,:)+E1(14,:) E1(8,:)+E1(15,:),...
   E1(9,:)+E1(10,:) E1(9,:)+E1(11,:) E1(9,:)+E1(12,:) E1(9,:)+E1(13,:),...
   E1(9,:)+E1(14,:) E1(9,:)+E1(15,:),...
   E1(10,:)+E1(11,:) E1(10,:)+E1(12,:) E1(10,:)+E1(13,:) E1(10,:)+E1(14,:) E1(10,:)+E1(15,:),...
   E1(11,:)+E1(12,:) E1(11,:)+E1(13,:) E1(11,:)+E1(14,:) E1(11,:)+E1(15,:),...
   E1(12,:)+E1(13,:) E1(12,:)+E1(14,:) E1(12,:)+E1(15,:),...
   E1(13,:)+E1(14,:) E1(13,:)+E1(15,:),...
   E1(14,:)+E1(15,:)];

H2=[(E0(:,1:15)-anharm),(E0(:,16:120)-anharm_2)];

w=E1;
w2=H2;
mu=u1m;
n2=120;
mu2=zeros(n2,3,s);
mu2(1,:,1) = sqrt(2).*mu(1,:);
```

```
mu2(16:29,:,1) = mu(2:15,:);

mu2(2,:,2) = sqrt(2).*mu(2,:);
mu2(16,:,2) = mu(1,:);
mu2(30:42,:,2) = mu(3:15,:);

mu2(3,:,3) = sqrt(2).*mu(3,:);
mu2(17,:,3) = mu(1,:);
mu2(30,:,3) = mu(2,:);
mu2(43:54,:,2) = mu(4:15,:);

mu2(4,:,4) = sqrt(2).*mu(4,:);
mu2(18,:,4) = mu(1,:);
mu2(31,:,4) = mu(2,:);
mu2(43,:,4) = mu(3,:);
mu2(55:65,:,4) = mu(5:15,:);

mu2(5,:,5) = sqrt(2).*mu(5,:);
mu2(19,:,5) = mu(1,:);
mu2(32,:,5) = mu(2,:);
mu2(44,:,5) = mu(3,:);
mu2(55,:,5) = mu(4,:);
mu2(66:75,:,5) = mu(6:15,:);

mu2(6,:,6) = sqrt(2).*mu(6,:);
mu2(20,:,6) = mu(1,:);
mu2(33,:,6) = mu(2,:);
mu2(45,:,6) = mu(3,:);
mu2(56,:,6) = mu(4,:);
mu2(66,:,6) = mu(5,:);
mu2(76:84,:,6) = mu(7:15,:);

mu2(7,:,7) = sqrt(2).*mu(7,:);
mu2(21,:,7) = mu(1,:);
mu2(34,:,7) = mu(2,:);
mu2(46,:,7) = mu(3,:);
mu2(57,:,7) = mu(4,:);
mu2(67,:,7) = mu(5,:);
mu2(76,:,7) = mu(6,:);
mu2(85:92,:,7) = mu(8:15,:);


mu2(8,:,8) = sqrt(2).*mu(8,:);
mu2(22,:,8) = mu(1,:);
mu2(35,:,8) = mu(2,:);
mu2(47,:,8) = mu(3,:);
```

```
mu2(58,:,8) = mu(4,:);
mu2(68,:,8) = mu(5,:);
mu2(77,:,8) = mu(6,:);
mu2(85,:,8) = mu(7,:);
mu2(93:99,:,8) = mu(9:15,:);


mu2(9,:,9) = sqrt(2).*mu(9,:);
mu2(23,:,9) = mu(1,:);
mu2(36,:,9) = mu(2,:);
mu2(48,:,9) = mu(3,:);
mu2(59,:,9) = mu(4,:);
mu2(69,:,9) = mu(5,:);
mu2(78,:,9) = mu(6,:);
mu2(86,:,9) = mu(7,:);
mu2(93,:,9) = mu(8,:);
mu2(100:105,:,9) = mu(10:15,:);

mu2(10,:,10) = sqrt(2).*mu(10,:);
mu2(24,:,10) = mu(1,:);
mu2(37,:,10) = mu(2,:);
mu2(49,:,10) = mu(3,:);
mu2(60,:,10) = mu(4,:);
mu2(70,:,10) = mu(5,:);
mu2(79,:,10) = mu(6,:);
mu2(87,:,10) = mu(7,:);
mu2(94,:,10) = mu(8,:);
mu2(100,:,10) = mu(9,:);
mu2(106:110,:,10) = mu(11:15,:);

mu2(11,:,11) = sqrt(2).*mu(11,:);
mu2(25,:,11) = mu(1,:);
mu2(38,:,11) = mu(2,:);
mu2(50,:,11) = mu(3,:);
mu2(61,:,11) = mu(4,:);
mu2(71,:,11) = mu(5,:);
mu2(80,:,11) = mu(6,:);
mu2(88,:,11) = mu(7,:);
mu2(95,:,11) = mu(8,:);
mu2(101,:,11) = mu(9,:);
mu2(106,:,11) = mu(10,:);
mu2(111:114,:,11) = mu(12:15,:);

mu2(12,:,12) = sqrt(2).*mu(12,:);
mu2(26,:,12) = mu(1,:);
mu2(39,:,12) = mu(2,:);
```

```
mu2(51,:,12) = mu(3,:);
mu2(62,:,12) = mu(4,:);
mu2(72,:,12) = mu(5,:);
mu2(81,:,12) = mu(6,:);
mu2(89,:,12) = mu(7,:);
mu2(96,:,12) = mu(8,:);
mu2(102,:,12) = mu(9,:);
mu2(107,:,12) = mu(10,:);
mu2(111,:,12) = mu(11,:);
mu2(115:117,:,12) = mu(13:15,:);


mu2(13,:,13) = sqrt(2).*mu(13,:);
mu2(27,:,13) = mu(1,:);
mu2(40,:,13) = mu(2,:);
mu2(52,:,13) = mu(3,:);
mu2(63,:,13) = mu(4,:);
mu2(73,:,13) = mu(5,:);
mu2(82,:,13) = mu(6,:);
mu2(90,:,13) = mu(7,:);
mu2(97,:,13) = mu(8,:);
mu2(103,:,13) = mu(9,:);
mu2(108,:,13) = mu(10,:);
mu2(112,:,13) = mu(11,:);
mu2(115,:,13) = mu(12,:);
mu2(118:119,:,13) = mu(14:15,:);


mu2(14,:,14) = sqrt(2).*mu(14,:);
mu2(28,:,14) = mu(1,:);
mu2(41,:,14) = mu(2,:);
mu2(53,:,14) = mu(3,:);
mu2(64,:,14) = mu(4,:);
mu2(74,:,14) = mu(5,:);
mu2(83,:,14) = mu(6,:);
mu2(91,:,14) = mu(7,:);
mu2(98,:,14) = mu(8,:);
mu2(104,:,14) = mu(9,:);
mu2(109,:,14) = mu(10,:);
mu2(113,:,14) = mu(11,:);
mu2(116,:,14) = mu(12,:);
mu2(118,:,14) = mu(13,:);
mu2(120,:,14) = mu(15,:);

mu2(15,:,15) = sqrt(2).*mu(15,:);
mu2(29,:,15) = mu(1,:);
```

```
mu2(42,:,15) = mu(2,:);
mu2(54,:,15) = mu(3,:);
mu2(65,:,15) = mu(4,:);
mu2(75,:,15) = mu(5,:);
mu2(84,:,15) = mu(6,:);
mu2(92,:,15) = mu(7,:);
mu2(99,:,15) = mu(8,:);
mu2(105,:,15) = mu(9,:);
mu2(110,:,15) = mu(10,:);
mu2(114,:,15) = mu(11,:);
mu2(117,:,15) = mu(12,:);
mu2(119,:,15) = mu(13,:);
mu2(120,:,15) = mu(14,:);

%% Parameters of the simulation
n_t = 1024;
n_zp = 2*n_t; % the zeropadded length
dt = 9e-15; %fs
T2 = 1000e-15; %dephasing time
c = 2*pi; %unit conversion factor

wf=w*3e10; %Hz
wf2=w2*3e10;

R_r = zeros(n_t,n_t);
R_nr = zeros(n_t,n_t);
t = (0:n_t-1)*dt;
 [T1,T3] = meshgrid(t,t);

% first calculate all rephasing diagrams
for j = 1:s
  for i  = 1:s

    mui = sqrt(mu(i,:)*mu(i,:)');
    muj = sqrt(mu(j,:)*mu(j,:)');
    cos1 = mu(i,:)*mu(j,:)'/(mui*muj);
    angle = (1 + 2*cos1^2 )/15;
    dipole = mui^2*muj^2;

    % rephasing diagram R1
    R_r = R_r - dipole*angle*exp(+ 1i*wf(j)*c.*T1 ...
              - 1i*wf(i)*c.*T3 ...
              - (T1+T3)/T2);
    % rephasing diagram R2
    R_r = R_r - dipole*angle*exp(+ 1i*wf(j)*c.*T1 ...
              - 1i*wf(i)*c.*T3 ...
```

```
            - (T1+T3)/T2);

    for k = 1:n2
      mujk = sqrt(mu2(k,:,j)*mu2(k,:,j)');
      muik = sqrt(mu2(k,:,i)*mu2(k,:,i)');

      dipole = mui*muj*muik*mujk;
      if muik~=0 &&  mujk~=0
    cos2 = mu2(k,:,i)*mu2(k,:,j)'/(muik*mujk);
      else
    cos2 = 0;
      end
      if muik~=0
    cos3 = mu(i,:)*mu2(k,:,i)'/(mui*muik);
    cos6 = mu(j,:)*mu2(k,:,i)'/(muj*muik);
      else
    cos3 = 0;
    cos6 = 0;
      end
      if mujk~=0
    cos4 = mu(j,:)*mu2(k,:,j)'/(muj*mujk);
    cos5 = mu(i,:)*mu2(k,:,j)'/(mui*mujk);
      else
    cos4 = 0;
    cos5 = 0;
      end
      angle2 = (cos1*cos2+cos3*cos4+cos5*cos6)/15;

      %rephasing diagram R3
      R_r = R_r + dipole*angle2*exp(+ 1i*wf(j)*c.*T1 ...
                - 1i*(wf2(k)-wf(j))*c.*T3 ...
                - (T1+T3)/T2);
    end
  end
end

% now non-rephasing diagrams
for j = 1:s
  for i  = 1:s
    mui = sqrt(mu(i,:)*mu(i,:)');
    muj = sqrt(mu(j,:)*mu(j,:)');
    cos1 = mu(i,:)*mu(j,:)'/(mui*muj);
    angle = (1 + 2*cos1^2 )/15;
    dipole = mui^2*muj^2;

    % non-rephasing diagram R4
```

```
    R_nr = R_nr - dipole*angle*exp(- 1i*wf(j)*c.*T1 ...
                - 1i*wf(j)*c.*T3 ...
                - (T1+T3)/T2);
    % non-rephasing diagram R5
    R_nr = R_nr - dipole*angle*exp(- 1i*wf(j)*c.*T1 ...
                - 1i*wf(i)*c.*T3 ...
                - (T1+T3)/T2);

    for k = 1:n2
      mujk = sqrt(mu2(k,:,j)*mu2(k,:,j)');
      muik = sqrt(mu2(k,:,i)*mu2(k,:,i)');

      dipole = mui*muj*muik*mujk;
      if muik~=0 && mujk~=0
    cos2 = mu2(k,:,i)*mu2(k,:,j)'/(muik*mujk);
      else
    cos2 = 0;
      end
      if muik~=0
    cos3 = mu(i,:)*mu2(k,:,i)'/(mui*muik);
    cos6 = mu(j,:)*mu2(k,:,i)'/(muj*muik);
      else
    cos3 = 0;
    cos6 = 0;
      end
      if mujk~=0
    cos4 = mu(j,:)*mu2(k,:,j)'/(muj*mujk);
    cos5 = mu(i,:)*mu2(k,:,j)'/(mui*mujk);
      else
    cos4 = 0;
    cos5 = 0;
      end
      angle2 = (cos1*cos2+cos3*cos4+cos5*cos6)/15;

      %non-rephasing diagram R6
      R_nr = R_nr + dipole*angle2*exp(- 1i*wf(j)*c.*T1 ...
                  - 1i*(wf2(k)-wf(i))*c.*T3 ...
                  - (T1+T3)/T2);
    end
  end
end

% divide first points (by row and column) by 2
R_r(:,1) = R_r(:,1)./2;
R_r(1,:) = R_r(1,:)./2;
R_nr(:,1) = R_nr(:,1)./2;
```

```
R_nr(1,:) = R_nr(1,:)./2;

%what we have so far in the time domain
xc=R_r(64,:);
% figure()
% plot(real(xc))

% do the fft
R_r = fftshift(fft2(real(R_r)));
R_nr =fftshift(fft2(real(R_nr)));

R =(real(fliplr(circshift(R_r,[0 -1]))+R_nr));

figure(17)
xf=fftshift(fft(real(xc)));
plot(real(xf))

step=dt;
n=length(t);
q=1/(n*step);
l=q*(0:n-1);
i=0:length(t)-1;
wf=((i.*q)-(1/(2*step)));
ww=wf/(3e10);
wp=ww;
figure(21)
plot(ww,((xf)))
contour(ww,wp,(R'),50)
xlim([1560 1700])
ylim([1560 1700])
```

A1.2. MATLAB Program to Calculate TDC

```
clear all;
close all;

theta=20; %transition dipole angle relative to CO in degrees
s=6;
osc=15;
dipole_strength=0.77;%1; %oscillator strength in Debye (D)
dipole_strength_r= 0.46;%0.6; %oscillator strength in Debye (D)
dipole_strength_r2=1; %1.3;

%% Loading the coordinates
Oxygen = [ -0.690179   -6.360154   -3.474759;...
    7.756225   -1.011115    1.827739];
```

```
Carbon = [-0.905426   -5.303824   -2.878577;...
    6.701686   -0.419467    1.591780];

Carbon2 =[0.188374   -4.534075   -2.242996;...
    5.543281   -1.111680    0.981777];

oxy_180=[0.69018,6.3602,-3.4748
-7.7562,1.0111,1.8277];

carb_180 =[0.90543,5.3038,-2.8786
-6.7017,0.41947,1.5918];

carb2_180 = [-0.18837,4.5341,-2.243
-5.5433,1.1117,0.98178];


oxy_180_up=  oxy_180(:,3)+4.5;
carb_180_up=  carb_180(:,3)+4.5;
carb2_180_up = carb2_180(:,3)+4.5;
Oxy3 = Oxygen(:,3)+4.5+4.5;
Carb3 = Carbon(:,3)+4.5+4.5;
C3=  Carbon2(:,3)+4.5+4.5;

Oxy = [Oxygen(:,1) Oxygen(:,2) Oxygen(:,3);...
    oxy_180(:,1) oxy_180(:,2) oxy_180_up(:,1);...
    Oxygen(:,1) Oxygen(:,2) Oxy3(:,1)];

Carb = [Carbon(:,1) Carbon(:,2) Carbon(:,3);...
    carb_180(:,1) carb_180(:,2) carb_180_up(:,1);...
    Carbon(:,1) Carbon(:,2) Carb3(:,1)];

Nitro = [Carbon2(:,1) Carbon2(:,2) Carbon2(:,3);...
    carb2_180(:,1) carb2_180(:,2) carb2_180_up(:,1);...
    Carbon2(:,1) Carbon2(:,2) C3(:,1)];


%% Defining the coordinate system to use in defining the transition dipoles

dtheta = theta*pi/180; %Converts the angle of rotation into radians
% dtheta_2 = -theta*pi/180; %Converts the angle of rotation into radians
% dtheta=[dtheta_1 dtheta_2];
CO = (Carb-Oxy); %Takes the coordinates for the oxygens and subtracts them from those for the
carbons.  This defines the carbonyl vector.
COn = sqrt(diag(CO*CO.')); %Normalizes the C=O vector to itself, so COn means the
normalized CO vector
```

```
for l=1:s
   COu(l,:)=CO(l,:)./COn(l); %Filling in the matrix defining the unit vector for the C=O bond
end


%Repeat the code for CO now for the C-N bond
CN = (Carb-Nitro);
CNn = sqrt(diag(CN*CN.'));
for l=1:s
   CNu(l,:)=CN(l,:)./CNn(l);
end

%Defining the coordinate system with the carbonyl bond as the x axis
xp = COu; %Defines the x axis to be along the vector defined by the C=O bond

zp = cross(COu,CNu); %Defines the z axis by taking the cross product of the vectors defining
the C=O and C-N bonds that we know lie in the same plane.  The cross product then gives the
vector orthogonal to this plane.
zpn = sqrt(diag(zp*zp.')); %Normalizes the z axis to itself.
for l=1:s
   zpu(l,:) = zp(l,:)./zpn(l); %Turns the z axis into a unit vector.  Prevents having to do other
scaling calculations later.
end

yp = cross(xp, zpu); %Defines the y axis for this 3D space.  It is already normalized to a unit
vector

for l=1:s
   uc(l,:)= COn(l)*cos(dtheta).*xp(l,:) + COn(l)*sin(dtheta).*yp(l,:); %rotates the transition
dipole
end
uc = uc./(sqrt(diag(uc*uc.'))*ones(1,3)); %Normalizes the transition dipole to itself
coordc = (Carb+Oxy)/2; %Defines the coordinates for the midpoint of the transition dipole.
uc = uc*dipole_strength; %defines the length of the transition dipole and therefore its magnitude

%% coords for rings
theta15=10.69;
dtheta15 = theta15*pi/180; %Converts the angle of rotation into radians
for l=1:s
   ur15(l,:)= COn(l)*cos(dtheta15).*xp(l,:) + COn(l)*sin(dtheta15).*yp(l,:); %rotates the
transition dipole
end
ur15 = ur15./(sqrt(diag(ur15*ur15.'))*ones(1,3)); %Normalizes the transition dipole to itself

ur15d=ur15*dipole_strength_r2;
```

```
theta25=11.02;
dtheta25 = theta25*pi/180; %Converts the angle of rotation into radians
for l=1:s
   ur25(l,:)= COn(l)*cos(dtheta25).*xp(l,:) + COn(l)*sin(dtheta25).*yp(l,:); %rotates the
transition dipole
end
ur25 = ur25./(sqrt(diag(ur25*ur25.'))*ones(1,3)); %Normalizes the transition dipole to itself

ur25d=ur25*dipole_strength_r;

theta35=22.07;
dtheta35 = theta35*pi/180; %Converts the angle of rotation into radians
for l=1:s
   ur35(l,:)= COn(l)*cos(dtheta35).*xp(l,:) + COn(l)*sin(dtheta35).*yp(l,:); %rotates the
transition dipole
end
ur35 = ur35./(sqrt(diag(ur35*ur35.'))*ones(1,3)); %Normalizes the transition dipole to itself

ur35d=ur35*dipole_strength_r;

theta45=166.59;
dtheta45 = theta45*pi/180; %Converts the angle of rotation into radians
for l=1:s
   ur45(l,:)= COn(l)*cos(dtheta45).*xp(l,:) + COn(l)*sin(dtheta45).*yp(l,:); %rotates the
transition dipole
end
ur45 = ur45./(sqrt(diag(ur45*ur45.'))*ones(1,3)); %Normalizes the transition dipole to itself

ur45d=ur45*dipole_strength;

ring1 = [3.218364   -1.133669    0.166171];
ring2 = [1.016301   -2.581777   -0.990552];

ring1_180 =[-3.2184,1.1337,0.16617];
ring2_180 =[-1.0163,2.5818,-0.99055];


ring1_2=  ring1_180(:,3)+4.5;
ring2_2=  ring2_180(:,3)+4.5;
ring1_3 = ring1(:,3)+4.5+4.5;
ring2_3 = ring2(:,3)+4.5+4.5;

R_1= [ring1(:,1) ring1(:,2) ring1(:,3);...
   ring1_180(:,1) ring1_180(:,2) ring1_2(:,1);...
   ring1(:,1) ring1(:,2) ring1_3(:,1)];
```

```
R_2= [ring2(:,1) ring2(:,2) ring2(:,3);...
   ring2_180(:,1) ring2_180(:,2) ring2_2(:,1);...
   ring2(:,1) ring2(:,2) ring2_3(:,1)];
% ur;
coordr=(R_1+R_2)/2;
%

%%

u = [ur15d(2,:); ur25d(2,:); ur35d(2,:); ur45d(2,:); uc(2,:);...
   ur15d(4,:); ur25d(4,:); ur35d(4,:); ur45d(4,:); uc(4,:);...
   ur15d(6,:); ur25d(6,:); ur35d(6,:); ur45d(6,:); uc(6,:)];
coord = [coordr(1,:); coordr(1,:); coordr(1,:); coordc(1,:); coordc(2,:);...
   coordr(2,:); coordr(2,:); coordr(2,:); coordc(3,:); coordc(4,:);...
   coordr(3,:); coordr(3,:); coordr(3,:); coordc(5,:); coordc(6,:)];
% coord = [coordc(2,:); coordc(2,:); coordc(2,:); coordc(2,:); coordc(2,:);...
%     coordc(4,:); coordc(4,:); coordc(4,:); coordc(4,:); coordc(4,:);...
%     coordc(6,:); coordc(6,:); coordc(6,:); coordc(6,:); coordc(6,:)];
%% Preparing the dipoles for plotting

u_factor = 5; %enlarges or shrinks u by this factor so you can see it clearly, this is essentially a
zooming command
u_coord1 = -u/2*u_factor+coord; %this and the next line of code provide the end coordinates for
the transition dipoles
u_coord2 = u/2*u_factor+coord;


uline1 = [u_coord1(:,1) u_coord2(:,1)].'; %This line and the following two lines of code define
the vector direction of the transition dipole
uline2 = [u_coord1(:,2) u_coord2(:,2)].';
uline3 = [u_coord1(:,3) u_coord2(:,3)].';

%% Plotting the transition dipoles
figure (2)
plot3(Carb(:,1),Carb(:,2),Carb(:,3),'k*',...
   Oxy(:,1),Oxy(:,2),Oxy(:,3),'r*',...
   u_coord1(:,1), u_coord1(:,2), u_coord1(:,3), 'ro',...
   u_coord2(:,1), u_coord2(:,2), u_coord2(:,3), 'ro',...
   uline1, uline2, uline3, 'g')


%% Calculating the coupling constants and resulting eigen energies
B = zeros(15,15);
for m = 1:5,
   for n = 6:10,
      rvec = coord(m,:)-coord(n,:);
```

```
      r = sqrt(rvec*rvec.');
      B(m,n) = (u(m,:)*u(n,:).'/r^3)-3*(u(m,:)*rvec.')*(u(n,:)*rvec.')/r^5; %coupling defined by
the TDC model
      B(m,n) = B(m,n)*5034;
      B(n,m) = B(m,n); %fills in the other half of the coupling constant matrix
   end
end

% for m = 5,
%    for n = 6:10,
%       rvec = coord(m,:)-coord(n,:);
%       r = sqrt(rvec*rvec.');
%       B(m,n) = (u(m,:)*u(n,:).'/r^3)-3*(u(m,:)*rvec.')*(u(n,:)*rvec.')/r^5; %coupling defined by
the TDC model
%       B(m,n) = B(m,n)*5034;
%       B(n,m) = B(m,n); %fills in the other half of the coupling constant matrix
%    end
% end

for m = 6:10,
   for n = 1:5,
      rvec = coord(m,:)-coord(n,:);
      r = sqrt(rvec*rvec.');
      B(m,n) = (u(m,:)*u(n,:).'/r^3)-3*(u(m,:)*rvec.')*(u(n,:)*rvec.')/r^5; %coupling defined by
the TDC model
      B(m,n) = B(m,n)*5034;
%       B(n,m) = B(m,n); %fills in the other half of the coupling constant matrix
   end
end

% for m = 10,
%    for n = 1:5,
%       rvec = coord(m,:)-coord(n,:);
%       r = sqrt(rvec*rvec.');
%       B(m,n) = (u(m,:)*u(n,:).'/r^3)-3*(u(m,:)*rvec.')*(u(n,:)*rvec.')/r^5; %coupling defined by
the TDC model
%       B(m,n) = B(m,n)*5034;
%       B(n,m) = B(m,n); %fills in the other half of the coupling constant matrix
%    end
% end

for m = 6:10,
   for n = 11:15,
      rvec = coord(m,:)-coord(n,:);
      r = sqrt(rvec*rvec.');
      B(m,n) = (u(m,:)*u(n,:).'/r^3)-3*(u(m,:)*rvec.')*(u(n,:)*rvec.')/r^5; %coupling defined by
```

```
the TDC model
        B(m,n) = B(m,n)*5034;
%       B(n,m) = B(m,n); %fills in the other half of the coupling constant matrix
    end
end


for m = 11:15,
    for n = 6:10,
        rvec = coord(m,:)-coord(n,:);
        r = sqrt(rvec*rvec.');
        B(m,n) = (u(m,:)*u(n,:).'/r^3)-3*(u(m,:)*rvec.')*(u(n,:)*rvec.')/r^5; %coupling defined by
the TDC model
        B(m,n) = B(m,n)*5034;
%       B(n,m) = B(m,n); %fills in the other half of the coupling constant matrix
    end
end

% for m = 15
%     for n = 6:10,
%         rvec = coord(m,:)-coord(n,:);
%         r = sqrt(rvec*rvec.');
%         B(m,n) = (u(m,:)*u(n,:).'/r^3)-3*(u(m,:)*rvec.')*(u(n,:)*rvec.')/r^5; %coupling defined by
the TDC model
%         B(m,n) = B(m,n)*5034;
%         B(n,m) = B(m,n); %fills in the other half of the coupling constant matrix
%     end
% end
%
% for m = 9,
%     for n = 11:15,
%         rvec = coord(m,:)-coord(n,:);
%         r = sqrt(rvec*rvec.');
%         B(m,n) = (u(m,:)*u(n,:).'/r^3)-3*(u(m,:)*rvec.')*(u(n,:)*rvec.')/r^5; %coupling defined by
the TDC model
%         B(m,n) = B(m,n)*5034;
%         B(n,m) = B(m,n); %fills in the other half of the coupling constant matrix
%     end
% end
%
% for m = 10
%     for n = 11:15,
%         rvec = coord(m,:)-coord(n,:);
%         r = sqrt(rvec*rvec.');
%         B(m,n) = (u(m,:)*u(n,:).'/r^3)-3*(u(m,:)*rvec.')*(u(n,:)*rvec.')/r^5; %coupling defined by
the TDC model
```

```
%        B(m,n) = B(m,n)*5034;
%        B(n,m) = B(m,n); %fills in the other half of the coupling constant matrix
%    end
% end
```

A1.3. MATLAB Program to Translation and Rotation of Coordinates

Example code used to translate and rotate coordinates of molecules to make the violanthrone-79 configurations. The output from this code was used for the TDC code and to simulate the linear IR absorption and the 2D IR spectra.

```
clear all; close all

% Cartesian Coordinates

% oxygen=importdata('oxy_cent_trimer.txt');
% carbon=importdata('carb_cent_trimer.txt');
% carbon2=importdata('nitro_cent_trimer.txt');

localmode=importdata('localmodes.txt');
%
local2=localmode(:,3)+4.5;
local3=local2(:,1)+4.5;
%
modes=[localmode(:,1) localmode(:,2) localmode(:,3);...
   localmode(:,1) localmode(:,2) localmode(:,3);...
   localmode(:,1) localmode(:,2) localmode(:,3)];

% Oxygen = [ -0.690179   -6.360154   -3.474759;...
%     7.756225   -1.011115    1.827739];
% Carbon = [-0.905426   -5.303824   -2.878577;...
%     6.701686   -0.419467    1.591780];
%
% Carbon2 =[0.188374   -4.534075   -2.242996;...
%     5.543281   -1.111680    0.981777];

% ring1 = [3.218364   -1.133669    0.166171];
% ring2 = [1.016301   -2.581777   -0.990552];

%% Rotations and Translation Parameters
num_atoms=18; %number of atoms
alpha=0; %angle for rotation about x-axis
```

```
beta=0; %angle for rotation about y-axis
gamma=180; %angle for rotation about z-axis
T=[0 0 0]; %Translation
x0=[T(1),T(2),T(3),alpha,beta,gamma]';
% ahold=[0 0 1 1 1 1];


%% Correct list of Parameters

Rx=[1 0 0; 0 cosd(alpha) -sind(alpha);0 sind(alpha) cosd(alpha)];
Ry=[cosd(beta) 0 sind(beta); 0 1 0; -sind(beta) 0 cosd(beta)];
Rz=[cosd(gamma) -sind(gamma) 0; sind(gamma) cosd(gamma) 0; 0 0 1];

% mode_adj=zeros(size(modes));
for n=6:10
%     oxy_adj(n,:)=(Rx*Ry*Rz*(Oxygen(n,:)'+T'))';
%     carb_adj(n,:)=(Rx*Ry*Rz*(Carbon(n,:)'+T'))';
%     carb2_adj(n,:)=(Rx*Ry*Rz*(Carbon2(n,:)'+T'))';
%       ring1_adj(n,:)=(Rx*Ry*Rz*(ring1(n,:)'+T'))';
%       ring2_adj(n,:)=(Rx*Ry*Rz*(ring2(n,:)'+T'))';
lm_adj(n,:)=(Rx*Ry*Rz*(modes(n,:)'+T'))';

end


local_adj_180=[localmode(:,1) localmode(:,2) localmode(:,3);...
   lm_adj(:,1) lm_adj(:,2) lm_adj(:,3);...
   localmode(:,1) localmode(:,2) localmode(:,3)];
```

Appendix II

Gaussian Input File

A2.1. Gaussian Input File for Perylene Derivative (Lumogen Orange)

Here is an example input file used to complete a Gaussian calculation on the Rappé group's cluster. Different versions of Gaussian can be used. However, verison D must be used to complete anharmonic calculations.

```
%mem=2000MB
%nprocshared=8
%chk=JC272.chk
#p opt=tight freq=(noraman,hpmodes) b3lyp/6-31g(d) nosymm geom=connectivity

Perylene opt and freq calc

0 1
 C            -12.44534661  -10.50802072    3.30057665
 C            -11.12091950  -10.98228725    3.89360061
 C             -9.99223778   -9.95947216    4.02047681
 C            -10.26546220   -8.53555642    3.54192545
 C            -11.46112110   -8.19227920    2.99590341
 C            -12.60788323   -9.23007620    2.86840292
 C             -8.77685181  -10.29307512    4.53601466
 C             -9.15388979   -7.50761544    3.68235316
 C             -7.82808011   -7.94389962    4.28200955
 C             -7.64062018   -9.23943923    4.66410152
 C             -6.71182345   -6.90274743    4.43652755
 C             -8.18861788   -5.20508170    3.42665833
 C             -9.32408228   -6.24169796    3.26441940
 C            -10.66198802   -5.83682108    2.61188814
 C            -11.66554857   -6.74779761    2.49383700
 H            -12.59716508   -6.46243184    2.05205732
 H            -10.80221506   -4.83789923    2.25495946
 H             -8.60053855  -11.29814039    4.85797848
 H             -6.69342308   -9.53631560    5.06315570
 C            -14.96372807   -9.72715502    2.13624012
```

H	-15.89420305	-9.44434509	1.69009132
C	-13.34624897	-12.93465526	3.67372108
C	-12.12672408	-13.30215958	4.16197157
H	-11.96821497	-14.31499448	4.46893045
C	-13.95478516	-8.82021624	2.23764804
C	-13.58206756	-11.51163027	3.19541725
C	-10.96422060	-12.27725142	4.28713997
C	-14.76873046	-11.16144016	2.66896625
H	-14.09562766	-7.82173811	1.87938618
N	-6.99329907	-5.46108799	4.26834470
C	-14.50170185	-13.94044968	3.58699321
C	-15.92250922	-12.18785015	2.59178137
N	-15.88051015	-13.48145708	3.31750365
H	-10.02463375	-12.59457986	4.68917407
C	-16.57501231	-14.49924285	2.51484248
C	-7.24434805	-4.88601310	5.59796407
H	-6.18041869	-4.77361113	5.57410612
H	-7.99430419	-5.64206286	5.70296472
H	-16.47320015	-15.10173514	3.39327276
H	-17.13908839	-13.64667817	2.19911521
O	-8.28713496	-4.09959100	2.83334620
O	-5.54534199	-7.27985549	4.72028656
O	-14.27551190	-15.16590644	3.76025114
O	-16.93736309	-11.91106271	1.90131019
C	-17.96179592	-15.15659603	2.38209622
C	-19.81081526	-16.20986466	1.05207963
C	-20.05071485	-15.93583810	3.53377656
C	-20.57330926	-16.38761374	2.15801373
H	-20.17408881	-16.52428973	0.09628242
H	-20.65263078	-16.07603327	4.40746942
H	-21.53834740	-16.84195764	2.07525050
C	-6.92214925	-5.15707081	7.07906805
C	-5.66629620	-5.51055736	7.44461889
C	-8.02567999	-5.02520364	8.14465726
C	-5.34198008	-5.77821734	8.92625163
C	-7.74184016	-5.26538963	9.44793869
C	-6.31381711	-5.66437923	9.86392669
H	-4.34998396	-6.05437038	9.21525453
H	-8.50963822	-5.17757214	10.18776886
H	-6.08871865	-5.85140397	10.89308701
C	-17.56161376	-15.35565843	-0.09202404
H	-16.52583590	-15.40036484	0.17147569
C	-18.42183574	-15.55495415	1.16954755
C	-18.30487641	-14.90780778	5.01412791
H	-18.59974293	-13.89467386	5.19263698
C	-18.82868856	-15.35997690	3.63805216

C	-18.89356174	-15.81452002	6.11058550
C	-16.76796223	-15.00663167	5.03704771
H	-16.40455393	-14.69235777	5.99318170
H	-16.47304489	-16.01968384	4.85887520
H	-16.35848727	-14.37664462	4.27527111
H	-18.52992022	-15.50031326	7.06654956
H	-19.96122464	-15.74592519	6.09504955
H	-18.59854797	-16.82739944	5.93206280
C	-17.87452164	-13.98253140	-0.71545335
C	-17.88188464	-16.46604218	-1.11055010
H	-17.27751781	-13.84430603	-1.59280936
H	-18.91072133	-13.93849293	-0.97887797
H	-17.65301373	-13.21103212	-0.00810427
H	-17.66441700	-17.42023096	-0.67790343
H	-18.91856479	-16.42124167	-1.37280068
H	-17.28583026	-16.32823480	-1.98835173
C	-4.56390816	-5.64466732	6.37786846
C	-9.45075662	-4.61832103	7.72804959
H	-3.85243903	-6.38007303	6.69038244
H	-9.40342365	-3.99303334	6.86116847
C	-3.85567285	-4.28905661	6.19828424
C	-5.19395774	-6.07652919	5.04009057
C	-10.12274802	-3.84802060	8.87981661
C	-10.27153610	-5.88057357	7.40610429
H	-9.55138884	-2.97132247	9.10331965
H	-11.11266297	-3.56388730	8.58951128
H	-10.17093927	-4.47318007	9.74683474
H	-10.31852701	-6.50658152	8.27290706
H	-11.26174075	-5.59728727	7.11645487
H	-9.80445684	-6.41491117	6.60518934
H	-3.09069116	-4.38242980	5.45619123
H	-4.56729948	-3.55341258	5.88677097
H	-3.41703571	-3.98952945	7.12713896
H	-4.42773491	-6.16982822	4.29881965
H	-5.68592334	-7.01865831	5.16516144
H	-5.90583164	-5.34141075	4.72677266

A2.2. Obtaining the Dipole Derivative Vectors

After the geometry optimization and frequency calculation is completed, the following code can be used to get the dipole derivative vectors for an individual normal mode. The output will label the dipole derivative vectors by mode number, which can be found in the original

frequency calculation.

```
%chk=myfreq.chk
# Freq=(ReadFC) Geom=AllCheck IOp(7/33=1)
```

LIST OF ABBREVIATIONS

Abbreviations	Full Name
2D IR	Two-dimensional Infrared
$AgGaS_2$	Silver Gallium Sulfide
AOM	Acousto-optic Modulator
AWG	Arbitrary Waveform Generator
BBO	Beta Barium Borate
DDG	Digital Delay Generator
FWHM	Full Width Half Maximum
GVD	Group Velocity Delay
HeNe	Helium Neon
MCT	Mercury Cadmium Telluride
OPA	Optical Parametric Amplifier
PAH	Polycyclic Aromatic Hydrocarbon
TDC	Transition Dipole Coupling
TOD	Third-order Dispersion